PEOPLE'S DEMOCRATIC REPUBLIC OF ALGERIA

MINISTRY OF HIGHER EDUCATION AND SCIENTIFIC RESEARCH

University of Mohamed Boudiaf-M'sila

Faculty of Technology

Department of Electronic

THESIS

Presented for the graduation of

DOCTORAT OF SCIENCES

Field: Electronic
Option: Electronic

By: Abdelbaki CHEROUANA

THEME

Conception and modeling of photonic components Application: photonic waveguide sensors

Presented and publicly defended the: 16/03/2022

JURY MEMBERS:

HOCINI Abdesselam	Professor	University of M'sila	Chairman
BOUCHAMA Idris	Professor	University of M'sila	Supervisor
BENCHEIKH Abdelhalim	Professor	University of BBA	Co-Supervisor
FERRIA Kouider	Professor	University of Sétif 1	Examiner
BAKHOUCHE Belkacem	Senior Lecturer	University of Sétif 1	Examiner
BOURAS Mounir	Senior Lecturer	University of M'sila	Examiner

Academic year: 2021/2022

REPUBLIQUE ALGERIENNE DEMOCRATIQUE ET POPULAIRE
MINISTERE DE L'ENSEIGNEMENT SUPERIEUR ET DE LA RECHERCHE SCIENTIFIQUE

Université Mohamed Boudiaf - M'sila

Faculté de Technologie

Département d'Electronique

THÈSE

Présentée en vue de l'obtention du diplôme de

Doctorat en Sciences en Electronique

Spécialité : Électronique

Par : Abdelbaki CHEROUANA

THÈME

Conception et modélisation des composants photoniques. Application Capteurs optiques à base de guides d'ondes photoniques

---

Présenté et défendu publiquement le : 16/03/2022

MEMBRES DU JURY

HOCINI Abdesselam	Professeur	Université de M'sila	Président
BOUCHAMA Idris	Professeur	Université de M'sila	Encadreur
BENCHEIKH Abdelhalim	Professeur	Université de BBA	Co-Encadreur
FERRIA Kouider	Professeur	Université de Sétif 1	Examinateur
BAKHOUCHE Belkacem	Maître de conférences	Université de Sétif 1	Examinateur
BOURAS Mounir	Maître de conférences	Université de M'sila	Examinateur

Année universitaire: 2021/2022

الحمد لله حمدا كثيرا طيبا مباركا فيه

Acknowledgments

This work never happens in this way without the help of all those who have collaborated near or far and who deserve the sufficient thanks.

Big thanks go first to my dear family

I would like to thank Mr. BOUCHAMA Idris, Professor of Electronics, Faculty of Technology, University of Mohamed Boudiaf M'sila, my thesis director, who supervised me throughout this thesis and for his kindness.

A big thank you goes to Mr. BENCHEIKH Abdelhalim, Professor from BBA University, Co-director of this thesis, not only for his help and many advices, but also for the encouragement he lavished on me for register for this thesis and to accomplish it.

I would like to thank Mr. HOCINI Abdesselam, Professor at the University of M'sila, who did me a great honor to accept to chair the jury for this thesis.

I address my thanks to Mr. FERRIA Kouider, Professor at the University of Sétif 1as well as to Mr. BAKHOUCHE Belkacem, lecturer class A, from the University of Sétif 1, and to Mr. BOURAS Mounir, lecturer class A, from M'sila University, for the honor they did me by accepting to be examiners of this thesis.

I thank everyone with whom I have shared my studies and research, especially these years of thesis.

Chapter IV: Birefringent Planar Waveguide based Sensor

List of figures

Chapter I: Basic Component of Photonic Sensors

Chapter II: Optical Sensing Mechanisms and Architectures

Chapter IV: Birefringent Planar Waveguide based Sensor

GENERAL INTRODUCTION

Optical sensors are a class of devices that use various forms of light–matter interactions to detect, interrogate, and quantify molecules for multiple applications. Progress in materials, light sources, innovative solutions and detectors covering wider ranges of the electromagnetic spectrum, with higher sensitivity; allow the use of new techniques that some time ago would have been considered inappropriate [1]. Photonic sensors are recent class of optical sensors. Hence, research in photonic structures and components has a significant impact on sensor technology. Chemical and biochemical sensors based on optical LOC (Lab-On- a-Chip) systems, represent the contemporary photonic sensors, as the last are estimated to expose high selectivity, high sensitivity and high stability. Furthermore, they have immunity to electromagnetic interference, smaller integration sizes and lower cost [2]. In photonic sensor, the optical waveguide is the essential part, because this photonic device has to ensure different functions. The first one consists in guiding the photonic signal from the optical source to the sensible area and detector. Secondly, the photonic waveguide has the role of transducer, enhancing the interaction between the chemical/biochemical process and the optical signal [3]. The formation of modes in optical waveguides could be exploited for sensing. In fact, when the light propagates inside the waveguide by total internal reflection, it senses the medium surrounding the waveguide by the evanescent tails of its electric field. When a light wave interacts with the biomolecules that are binding to the waveguide surface, some of its properties (wavelength, amplitude or polarization) change and by monitoring these changes, the substance can be detected. A variety of optical-sensing mechanisms exist, including luminescence, fluorescence, phosphorescence, absorbance, elastic scattering, Raman scattering, surface-Plasmon resonance, guided-wave resonance, interference, and reflection/ transmission microscopy [4]. Optical variable has to be converted into a useful signal. To this aim, several photonic integrated configurations have been proposed, comprising, integrated optical interferometers, microring resonators, Bragg grating resonators, directional couplers and photonic crystals optical sensors [5]. Among integrated optical waveguides, slab optical waveguide based evanescent wave is widely used for chemical and biochemical sensing. Lithium niobate $LiNbO_3$ is considered a highly attractive material for production of active integrated optoelectronic and photonic components owing its exceptional optical, Ferro-electrical, piézo-electrical, and thermo-electrical properties [6]. Sensitivity is the most important parameter of a planar optical sensor. Thus, sensitivity enhancement of optical sensors based on evanescent wave interactions has attracted significant research interest. Nevertheless,

the majority of photonic sensors are fabricated by isotropic materials, hence, only one kind of modes can be propagating within, (TE mode or TM mode). Thing that permits the detection of one substance at a time by the same configuration. The use of a birefringent material, like $LiNbO_3$, as a core of the waveguide can permit us the detection of two different substances in the same time by the same configuration, by reason of, in such birefringent waveguide we have two orthogonal modes that propagated simultaneously without interference (TE mode and TM mode). TE mode can detect one substance, and TM mode can sense the other substance. On the other hand, knowing that sensitivity of photonic sensor depends on geometrical and physical parameters of the waveguide [3]. The application of variable electric field on the $LiNbO_3$ waveguide, can make the sensitivity of the sensor adjustable without varying physical and geometric parameters.

The main work of my dissertation is the modeling of birefringent planar waveguide based photonic sensor fabricated by $LiNbO_3$ as waveguiding film, and studying the influence of source, geometrical and physical parameters, as well as electric field induced birefringence on the sensitivity and evanescent field of the sensor.

The thesis is divided into four chapters. In the first chapter, we presented in detail the integrated optical waveguides transducers used in integrated photonic sensors.

In the second chapter, we described in detail principle sensing mechanisms and architectures employed in integrated optical photonic sensors.

The third chapter is divided in two parts. In the first part, an isotropic and anisotropic slab optical waveguides are modeled with two approaches, successively. The first is the optical ray approach, which allows us to determine the dispersion equation of the guided modes for an isotropic slab waveguide. The second is the electromagnetic approach used to determine the wave equations and their solutions, as well as, the solutions of electromagnetic field for an anisotropic slab waveguides. In addition, the influence of the physical and geometric parameters and the wavelength of the source on the propagating modes are studied. In the second part, the Effective Index Method (EIM) is used to computing the modal fields and the propagation constants in the Embedded-strip waveguide.

In the fourth chapter, after brief description of planar optical sensors principles, we have investigated sensitivity and evanescent field of a slab waveguide optical sensor constituted of Lithium Niobate as a guiding film. Hence, the influences of source, geometrical and physical parameters as well as the birefringence on the sensor sensitivity and on the evanescent field have been studied.

CHAPTER I:

BASIC COMPONENT OF PHOTONIC SENSORS

I.1. Introduction

The well-being of the individual is correlated by the process of monitoring the various aspects of the environment, involving chemical, physical or biomedical parameters. Optical sensor technology has a major part to play in this process, by promoting new solutions to difficult measurement subjects [1]. Optical sensors are devices that use various forms of light–matter interactions to detect and quantify atoms or molecules for several applications, in environmental, industry, medicine and chemical/biochemical analysis. Advances in optoelectronic technology have motivated their development. Waveguide-based sensors witch are recent classes of optical sensors, are becoming more and more attractive in the field of optical elaboration of signals for sensing applications in different areas, especially in chemical and bio-chemical detection. In this case, the operating principle consists of the variation of the effective index of the optical mode propagating into the structure, as a consequence of the presence of a chemical substance to be detected close to the sensor surface [5]. Generally, light is confined within the waveguide along the dimensions of 1D, 2D, or 3D. Based on the light confinement dimension, integrated waveguides can be classified as planar waveguides (1D), channel waveguides (2D), and photonic crystals (3D), respectively [7]. In photonic sensor, the optical waveguide is the essential part, because this photonic device has to assure different functions. The first one consists in guiding the photonic signal from the optical source to the sensible area and detector. Secondly, the photonic waveguide has the role of transducer, enhancing the interaction between the chemical/biochemical process and the optical signal [3].

In this chapter, we will present in detail the sensing principles of the main integrated optical waveguide transducers such as, strip waveguide, rib waveguide, slot waveguide, Sub-wavelength grating waveguide and photonic crystals waveguides.

I.2. Integrated waveguides for optical sensing

Optical waveguides are appropriate for photonic detections, since their precise detection, noise immunity, various geometries and high efficiency of light-matter interactions. Generally, there are three kinds of widely used waveguides, that is strip waveguide, rib waveguide and slot waveguide. Rib waveguides show low optical losses in comparison with the sensitivity. In contrast, slot waveguides exhibit a large sensitivity but high optical loss. Strip waveguides, in contrast, offer a good compromise between loss and sensitivity [8]. Most of integrated optical waveguides are fabricated with lithographic techniques on a single-chip in low cost and mass

production. Moreover, materials used for fabricating of integrated optical sensors can be high index contrast or low refractive index materials, in the objective of obtaining high sensitivities [9]. The rib and the wire (strip) integrated waveguides confines the light wave in the core which has the higher refractive index. Here a portion of evanescent wave interacts with the substances to be detected. However, the slot waveguide intensely confines light in the slot area of a low refractive index, makes the light matter interaction very powerful. The major sensing mechanism for integrated optical sensors is the detection of the refractive index RI change of analyte. Hence, integrated optical waveguides based RI sensors are usually employed by means of interferometers and microresonators [10]. In interferometers sensors such as directional couplers [11], Mach-Zehnder [12], Young (YI) interferometers [13], light matter interaction establishes an equivalent phase change, which is dependent on the difference between the effective indices of the sensor arm and the reference arm. In microresonator sensors, such as ring, disk and Bragg resonators, the wavelength of resonance shifts and thus, measures the refractive index changes that occur due to the biomolecular bindings [14].

I.2.1. Sensing principle in strip waveguide

As the electromagnetic wave travels through the silicon strip waveguide, most of the power is confined within the core. However, there is a part of light identified as evanescent field extending to the cladding and substrate as shown in Figure I.1. If an absorbing medium is located approximately to the waveguide, a part of the evanescent field is absorbed and the total modal power decreases as the mode propagates along the waveguide, which is detected as a reduced transmitted intensity. In waveguide based sensing, two basic approaches are normally used. For bulk or homogenous detecting, a waveguide core is exposed to an aqueous homogeneous objective medium, Figure I.2 (a). In the case of surface sensing, a waveguide core is functionalized by biomarkers in the aim of binding the molecules from an aqueous solution forming a surface layer, Figure I.2 (b). The amount of the evanescent field that propagates in the sensing region, expressed in terms of the evanescent field ratio, depends on the geometrical of the waveguide with respect to the wavelength of the propagating light, as well as on the optical properties of the used materials [15]. The sensors with high evanescent field ratio can interact more with the absorbing medium, which in turn improves the sensitivity of the sensor.

In strip waveguide, both quasi-TE and quasi-TM modes are studied, because of the probable molecules interaction with the evanescent field on the top and at the sidewalls of the

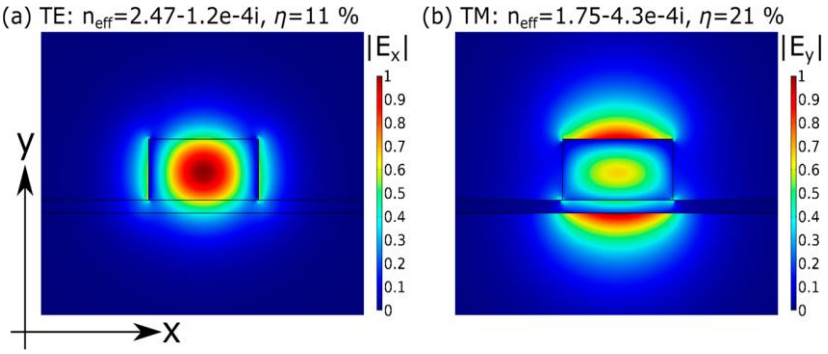

Figure I.1: (a) Field distribution of the fundamental quasi-TE mode; (b) Field distribution of the fundamental quasi-TM mode [15].

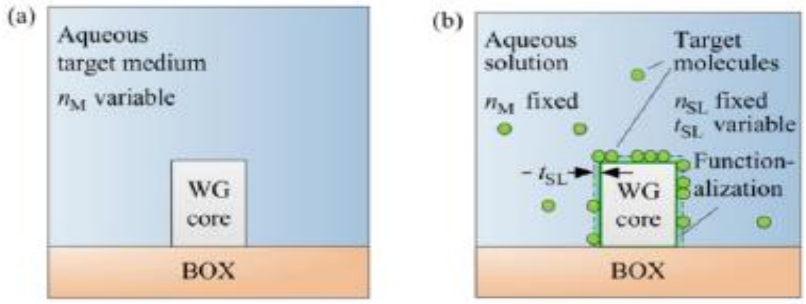

Figure I.2: (a) Homogeneous and (b) surface sensing in strip waveguide [16].

Waveguide **[**17, 15]. For quasi-TE mode, the dominant electrical field is in the horizontal direction. As the waveguide dimensions are reduced, a big part of the mode can exit from the core in the form of evanescent wave, leads to an increase in the evanescent field ratio. However, when the width of the core gets too small, the quasi-TE mode gets leaky and becomes a no propagating mode, in this case, all the energy is transferred to the cover medium. Furthermore, evanescent field ratio saturates for large width values because most of the energy is restricted in the core. It is worth to note that, in the vertical direction, evanescent field ratio does not depend so much on the waveguide height. For quasi-TM mode, the evanescent field ratio is sensitive to waveguide height. However, the waveguide becomes leaky when its dimensions become too small [10].

I.2.2. Sensing principle in rib waveguide

The rib waveguide of Figure I.3 consists of a silica substrate, a thin silicon layer on top of the substrate and a rectangular silicon rib part. The index of the rectangular region must be

larger than the surrounding medium in order to guide light. The optical sensors based on rib waveguides are used either in label-free detection or in bulk detection in the waveguide cover. The principle of sensing in a rib waveguide optical sensor relies on a propagating mode, which considerably expand into the cover medium surroundings the waveguide core. The interaction between the extended field and the surface layer or the refractive index of cladding medium, alters the effective refractive index of the propagating mode. Hence, an optical phase shift accumulated during propagation [16]. The sensitivity of a rib waveguide optical sensor depends on the power and the scattering of the evanescent field in the external medium. The optical sensor having high evanescent field ratio possibly interact more with the absorbing medium, which increases its sensitivity. In the rib waveguide, the evanescent field ratio can exceed that in the strip waveguide because analytes will interact with the evanescent field on the top and at the two sidewalls of the waveguide [17]. In addition to that, in a rib waveguide, both TE and TM modes are considered because they are important for the field improvement. TE mode in rib waveguide has an important part of field dispersed in the two shoulders of the waveguide, Figure I.3 (a). It has been shown that the evanescent field ratio is slightly dependent to the planar waveguide thickness. However, it is much higher at larger waveguide width. In the other hand, for TM polarization, Figure I.3 (b), it has been shown that the planar thickness of the rib waveguide has a big influence on the evanescent field ratio. Furthermore, it has been demonstrated that the geometry of the rib waveguide as well as the propagation loss are important parameters to be considered when designing a rib waveguide based photonic sensors [17].

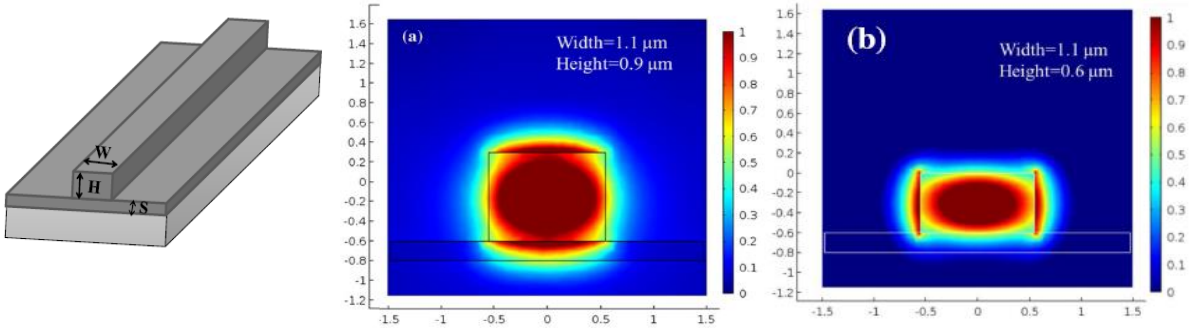

Figure I.3: Basic schematic of Rib waveguide (in the left). (a) TM, (b) TE mode distribution in a rib waveguide [17].

I.2.3. Slot waveguide sensor

The slot waveguide is a split of low refractive index medium between two strips of high refractive indices, Figure I.4. This structure is able to guide and strongly confine light in a nanoscale low-refractive index material by using total internal refraction and the discontinuity of the electric field at the normal boundary between two materials, which results into higher amplitude in the low-index slot region. The amplitude is proportional to the square of the ratio between the refractive indices of the high-index material and the low-index slot material [18]. When the width of the slot waveguides is similar to the decay length of the field, electric field remains across the slot and the section has high-field confinement, which results into propagation of light in the slot section. Furthermore, slot waveguides are generally fabricated by CMOS technology, permitting miniaturization, incorporation in a chip with other components. In addition to that, slot waveguide based sensors can make very small measurement and they have very low wavelength sensitivity. These make slot waveguide based photonic sensors promising for biochemical detections [19]. Refractive index sensors based on slot waveguide are mainly realized by way of interferometry systems such as, directional couplers [20], Mach-Zehnder interferometers [21] and microring resonators [22, 23, and 24].

Utilizing the remarkable field concentration in the slot region, a high light-matter interaction can be achieved in both surface and homogenous sensing, Figure I.5. Bulk sensing or homogeneous sensing refers to a sensitivity investigation when the cover and the slot area are filled directly with analyte. Thus, in the sensing region, changes of the refractive indices are occurred caused changes of the effective index of the guided mode. In the surface sensing, an ultrathin layer of receptor molecules is making on the slot waveguide structure to attach the targeted analyte. The binding between the target analyte and the ultrathin layer changes the detecting layer thickness that influences the effective index of the guided mode [10].

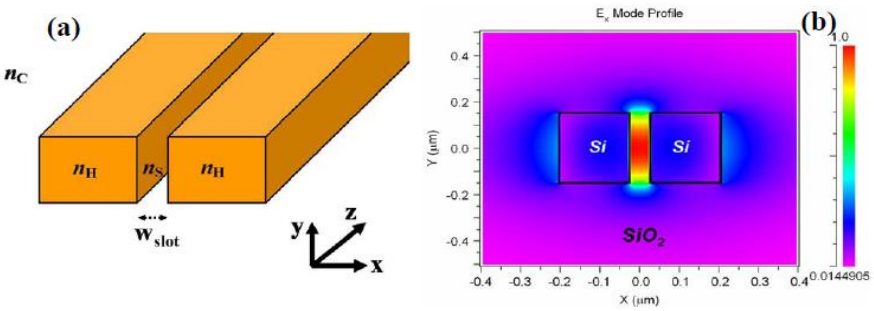

Figure I.4: (a) slot waveguide, (b) E_x profile of the quasi-TE mode in a slot waveguide [10].

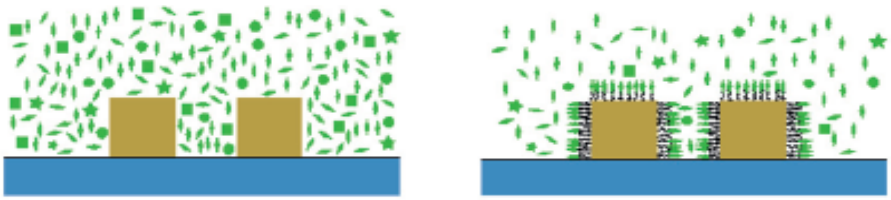

Figure I.5: Schematic of homogenous sensing and surface sensing principle in a slot waveguide surface [25].

For homogeneous sensing, the sensitivity of the slot waveguide is expressed as [9]:

$$S = \frac{\partial n_{eff}}{\partial n_c} = \frac{2n_c^0}{\eta_0 P} \iint_R |E(x,y)|^2 dxdy \quad \text{(I.1)}$$

Where: n_{eff} is the propagating mode effective index, $\eta_0$is the free space impedance, E is the electric field vector, n_c^0 is the unperturbed refractive index value of the cover medium. *P* is the Poynting vector and R is the integral domain.

In case of surface sensing, the sensitivity of slot waveguide can be written as [26]:

$$S = \frac{\partial n_{eff}}{\partial \rho} \quad \text{(I.2)}$$

Where: ρis the molecular adlayer thickness and $n_{eff}$is the propagating mode effective index. Using an optimized set of geometrical parameters, a sensitivity exceeding the unity can be achieved [26].

Two geometrical configurations of the slot waveguides can be realized, which are the vertical configuration and the horizontal one.

I.2.3.1. Vertical slot waveguide

In this waveguide, the slot area is vertically etched between the two Si strip waveguides, Figurer I.6. From Figure I.6 (a, b), it is evident that the TE mode has stronger confinement in the slot region than the TM mode due to the discontinuity of the normal component of the electric field at the high index contrast interface (x-component). The cladding and the slot region are filled directly with analyte (bulk sensing) or, the waveguide is coated by an ultra-thin receptor to immobilize the target (surface sensing).

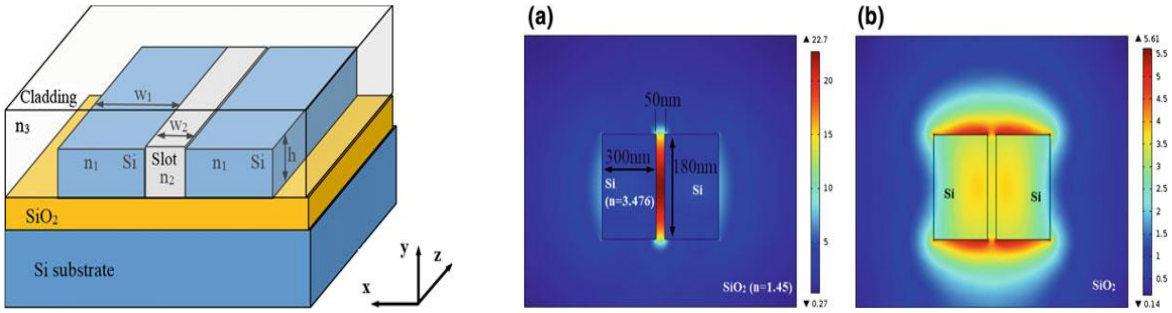

Figure I.6: Slot waveguide based on Silicon On Insulator SOI (in the left). (a), (b) electric field distribution for TE mode and TM mode successively [7].

I.2.3.2. Horizontal slot waveguide

In the horizontal slot waveguide a low refractive index medium is sandwiched between to high refractive indices mediums, Figure I.7 (a). This configuration is used to get a strong confinement in the slot region for TM mode [27]. The strong light confinement is for the TM mode because the normal component of the electric field is the y-component. FigureI.7 (b) represents the electric field distribution of the TM mode for the SOI horizontal slot waveguide.

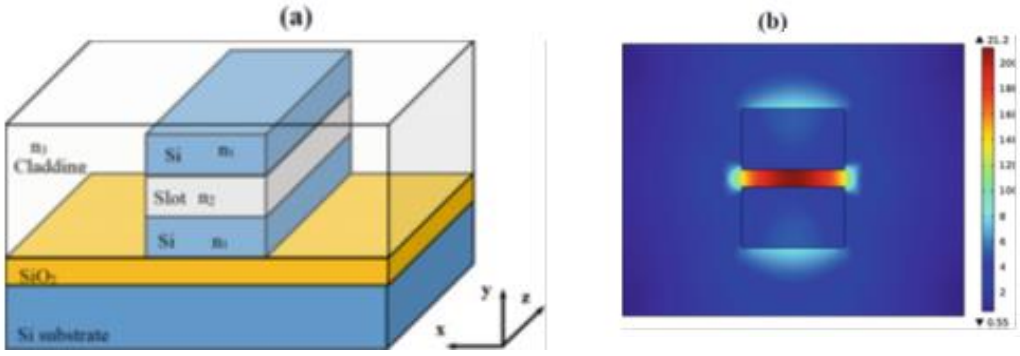

Figure I.7: (a) Schematic of horizontal slot waveguide, (b) electric-field distribution for TM mode [7].

I.2.4. Sub-wavelength grating waveguide based photonic sensors

Sub-wavelength grating waveguide is a periodic arrangement of silicon blocks, Figure I.8. The electromagnetic field solutions supported by this waveguide are described by the Floquet-Bloch modes formalism [28]. The operation of this grating waveguide in the sub-wavelength regime is very useful for photonic sensors. Figure I.8 illustrates the fundamental TE mode. The figure shows that, apart the field improvement that arises at the sidewalls, the

field is improved between the silicon blocks. This delocalization of the electric field increases the area of light-matter interaction, which is very useful for sensing applications. It has been showed that in homogenous and surface sensing, considerable enhancement of the sensitivity can be attained by the optimization of the waveguide geometry [29].

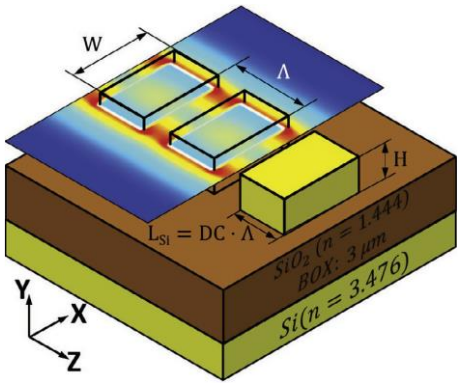

Figure I.8: Sub-wavelength grating waveguide for sensing applications [29].

I.2.5. Photonic Crystal for Chemical/Biochemical Sensors

Photonic sensors continue to be high on the agenda because of the ever-increasing demand for sensing applications in areas such as healthcare, defense, security, environment and food quality control, with a particular emphasis on miniaturised and personalised technologies A particular photonic structure that can be used for sensing is a Photonic Crystal (PhC) [30]. Photonic crystals are the periodic dielectric structures that can control and guide the photons. They can be categorized into three main groups as one-dimensional (1D), two-dimensional (2D), and three-dimensional (3D) structures [31]. An intrinsic property of PC structure is Photonic Band Gap (PBG) introduced by the periodicity of dielectric constant which prohibits a certain range of frequencies from propagating within the materials. The wavelength range of propagation in PC depends upon PBG structure which in turn is controlled by periodicity and refractive index of material. In fact, a little change in the periodic structure, which is called as defect, can create a new frequency range in the band gap, displaying particular resonant dips/peaks in the spectral signature. In the lattice of air holes in silicon, defects can be formed by reducing or increasing the radius of one or more air holes; even defects can be shaped by filling holes. Point defect creates microcavities and line defect creates waveguides in photonic crystals [32]. The main PC property exploited for sensing is the dependency of the width and position of the defect peak on the periodicity and on the refractive index of the surrounding

materials. In addition, light can be localized in a very small volume, leading to strong light–analyte interactions. Sensing mechanism in the most photonic crystal sensors is based on the refractive index (RI) change mechanism. By binding the chemical or biochemical molecules to active sensing surface, the refractive index will be changed. So, the resonant wavelength or the intensity of the transmission spectrum is changed. This process can be used as a way to measure the concentration of the molecules [33]. In photonic crystals, the sensor can be formed by simply illuminating the structure with an incandescent lamp, LED or Laser. Miniature, sturdy and low cost instrumentation for measuring properties of photonic crystals, with the addition of the ability to fabricate photonic crystal structures inexpensively has made them suitable for sensor applications in multidisciplinary field.

Several architecture of photonic crystals have been investigated and employed in photonic sensors to achieve high performance e.g., simple photonic crystal, microcavities, waveguides, ring resonators, photonic crystal fibers, slotted photonic crystals, slotted waveguides, slotted ring resonators, interferometry structures [34].

I.2.5.1. W1 photonic crystal waveguides

One of the most common defects is realized by removing a single row of holes along a symmetry direction of the crystal, thus creating a W1 waveguide, Figure I.9. This creates the defect modes in the photonic band structure. Forbidden frequencies can be guided by this defect Holes on either side of the line defect behave as very efficient mirrors for forbidden frequencies, and thus can be used to guide light. Photonic crystal waveguides can employ temporal light confinement mechanisms such as slow light [35, 36]. Physically, slow light behavior results from coherent backscattering at each unit cell of the photonic crystal forming slow moving interference patterns within the waveguide [35]. The main advantage of slow light is that it results in pulse length compression, which in turn leads to higher intensity and increased light-matter interactions. These linear defects are often employed to side-couple light into cavities by placing them in close proximity and allowing evanescent-wave coupling.

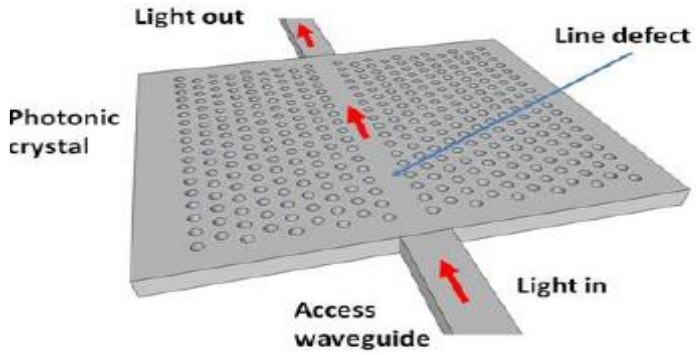

Figure I.9: Schematic of a 2-D slab photonic crystal, with a W1 defect. Light is delivered to and from a photonic crystal via access waveguides [37].

I.2.5.2. Slot photonic crystal waveguides

Slot photonic crystal waveguides (SPCWs), are constructed by introducing a slot cut along the length of a standard PhC planar waveguide, Figure I.10. These structures allow the confinement and guiding of light when it is polarized with the electrical field perpendicular to the slot. They are of interest for hybrid integration as they can enhance the light-matter interaction due to the combined slot and slow light effects [38, 39] with a low-index material filling the slot. Typical dimensions for a SPCW have been chosen to achieve proper fraction of electric-field energy density in the cladding region, especially the radius of holes in the first row (r_1) and the value of the slot width (W_{slot}).

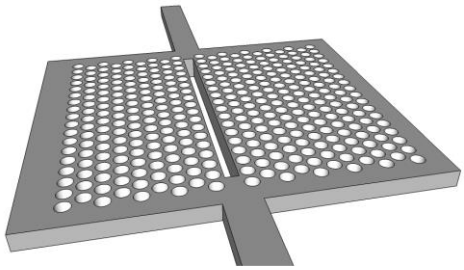

Figure I.10: Sketch of slotted photonic crystal geometry. Slot waveguide defect introduced to guiding region of W1 photonic crystal [37].

I.2.5.3. Planar photonic crystal cavities

Confinement of light in photonic crystals can be achieved by introducing defects in the ordered arrangement of refractive index, such as removing holes or changing their radii. The

result is the creation of available states for a narrow-band portion of radiation within the bandgap, which prevents radiation from propagating in neighboring regions. The performance of a cavity can be evaluated by a high quality factor *Q*, a concept determining how long the lifetime of photon confined in the cavity is, and a small cavity mode volume *V* defining the cavity ability of spatial mode confinement. Defects that form cavities in a two-dimensional slab can be classified in three main categories:

- They can be created by shifting several holes in the Γ-K direction to make "point-shift" of "zero-cell" cavity (H0), Figure I.11 (a), or removing one hole from a triangular lattice of air holes (H1), Figure I.11 (b)**.**

- L*n* cavities represent line defects, whereby *n* adjacent holes are removed from the periodic lattice in order to localise light along a line, Figure I.12 (a).

- Heterostructure cavities; the hole size and/or period is changed along a line defect similar to semiconductor heterostructures, Figure I.12 (b).

- PhCs can also feature periodicity in only a single spatial direction, to form "nanobeam" cavities. Nanobeam cavities utilise refractive index guiding in the transverse directions and photonic crystal confinement in the direction of propagation; interestingly, this approach tends to achieve smaller mode volumes than those of cavities in 2D slabs, while 2D cavities achieve higher Q-factors. To form a nanobeam cavity, a row of air holes is typically etched into a single mode waveguide. Defects can be introduced by removing holes, altering their radii or by tapering their sizes and positions. Figure I.12 (c).

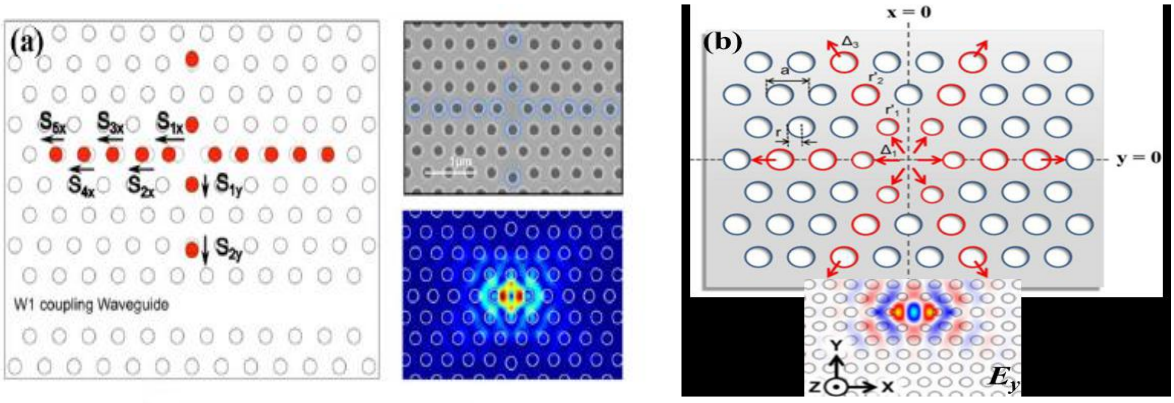

Figure I.11: Different kinds of PhC cavities and the E_y profile of the dipole mode (a) H0 PhC cavity [40]. (b) H1 PhC cavity [41].

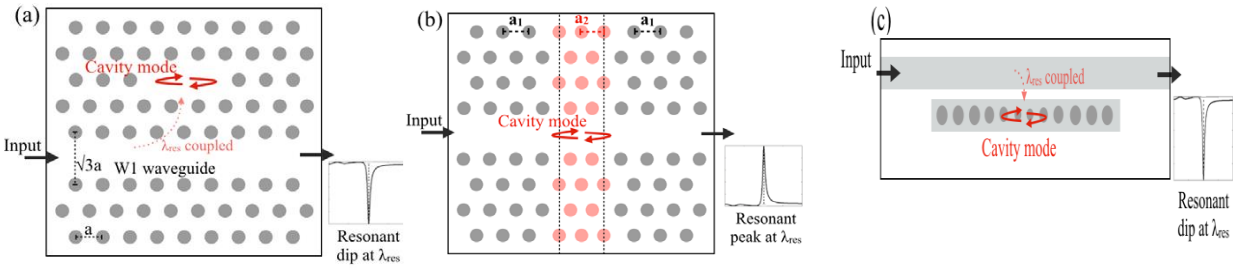

Figure I.12*:* (a) Top view of a PhC cavity, consisting of 3 missing holes. (b) Schematic of a Heterostructure cavity obtained by altering the period of the PhC in a specific section. (c) Schematic of a side-coupled nanobeam cavity [30].

I.2.5.4. Slot photonic crystal cavities

An interesting variant of the photonic crystal cavity configuration is the slotted cavity [37], Figure I.13 Slotted cavities combine the concept of photonic crystal confinement with the slot waveguide [18] by adding an air slot at the center of the cavity; their main advantage is a strong spatial confinement of the mode within the air slot and the resulting larger overlap of the mode with the sensing medium, which increases sensitivity. Indeed, slotted devices show the best performance in terms of sensitivity and LOD within the class of PhC biosensors [30].In this sensor, the technological approach employed for realizing the microcavity does not consist in modifying the lattice constant or the hole radii characterizing the PhC, but in introducing a straight line defect in which a modified waveguide width acts as resonant cavity [42]. The waveguide region is obtained by removing a row of air holes in the middle of the structure. An air – slot is embedded in this line defect region. The width of the air slot is kept constant, except in the middle. A slit is made by increasing the width of air slot in the center. This increasing in slot width results in the formation of reflective barriers for traveling mode. The cavity mode is strongly confined into the cavity region [3]. By this way, only resonant wavelengths can propagate inside the photonic cavity. The refractive index change (Δn) due to the sensor exposition to different analytes, causes a resonant wavelength shift ($\Delta\boldsymbol{\lambda}$). Consequently, it is possible to detect different analytes concentrations by monitoring the cavity transmission spectrum [3].

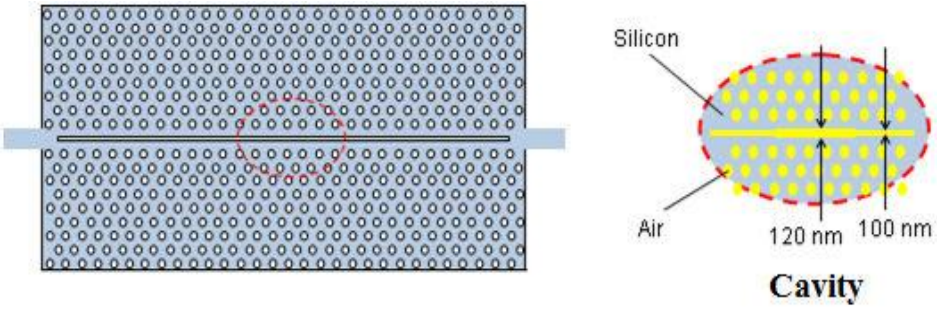

Figure I.13: Air-slot PhC cavity with zoom of slit in the slot [3].

I.3. Conclusion

In this chapter, we have presented different kinds of integrated optical waveguides widely used in photonic sensors as well as their sensing principles, including, strip waveguide, rib waveguide, slot waveguide, sub-wavelength grating waveguide and photonic crystals waveguides. The sensing principle is based on the interaction of the substances to be detected with the evanescent field extending to the cover. All these waveguides can be used either in homogenous or in surface sensing. The type of the waveguide and the optimization of its geometry, as well as the kind of polarization have a significant influence on the improvement of the sensor sensitivity.

CHAPTER II:

OPTICAL SENSING MECHANISMS AND ARCHITECTURES

II.1. Introduction

The evolution of science and technology of optical sensors has reached to a point that we can almost measure all physical parameters of interest and a broad range of biological and chemical quantities. The incorporation of optical waveguides in the sensing process adds an interesting twist to this field. For example, the formation of modes in optical waveguides could be exploited for sensing [43]. The optical waveguide sensors known as integrated photonic sensors are advantageous compared to the electronic and mechanical ones, since, they have high sensitivity, quick response and small tail. This kind of sensors facilities the label-free configurations, which make them, promising in chemical and bio-chemical detection [44, 45]. In fact, light propagates inside the waveguide by total internal reflection; it senses the medium adjoining the waveguide by the evanescent tails of its electric field. When a light wave interacts with the biomolecules that are binding on the waveguide, some of its properties (wavelength, amplitude or polarization) change, and by examining these transformations, the substance can be sensed. A diversity of optical sensing mechanisms exist, counting, fluorescence, absorbance, Raman scattering, surface plasmon resonance and effective index changes. In the purpose of detecting the optical properties changes, different configurations have been proposed, with characteristics appropriate for different applications. Such as, integrated optical interferometers, microring resonators, Bragg grating resonators, directional couplers and photonic crystals optical sensors.

In this chapter, we will describe in detail principle sensing mechanisms and architectures employed in integrated optical sensors.

II.2. Optical Sensing Principles

Different sensing mechanisms are exploited to detect the concerned analytes. Exactly, we can cite optical absorption, fluorescence, Raman scattering, Sagnac effect and detecting of refractive index changes. Many substances can be detected during their absorption change in the region of UV-Vis. Fluorescence spectroscopy uses a beam of monochromatic light that excites molecules of the composites and causes them to emit fluorescence. This mechanism is very selective if the molecules present fluorescence properties. Raman spectroscopy also employs a monochromatic light to monitor rotational, vibrational in a system. This sensing form can provide a fingerprint for each chemical species. Nevertheless, the sensitivity of this mechanism is usually low, in comparison with the other mechanisms. The mechanism of detecting the refractive index changes consist of determining the changes in refractive index

due to the presence of analytes that are in solution or adhered to the surface in the sensing region of the waveguide. Photonic sensors based on surface plasmon resonance are used to improve the detections of refractive index changes. Hence, when the condition of resonance is satisfied, an increase in the sensitivity is attained.

II.2.1. Optical absorption

Optical absorption is an important sensing mechanism employed in photonic biochemical detectors. This mechanism uses the Beer-Lambert law that joins the optical intensity to the substance concentration as follow:

$$\mathrm{I} = I_0 exp(-\alpha L) \tag{II.1}$$

Where $I_0$and $I_0$are the input and output light intensities at the input and the output of the waveguide respectively. L is the optical path, α is the absorption coefficient that is function of source wavelength and the photonic properties of the material.

For liquids, the absorption coefficient can be expressed as the product of molar absorptivity, $\varepsilon(\lambda)$, and the concentration, c , of the absorbers:

$$\alpha_{liquids}(\lambda) = \varepsilon(\lambda).c \tag{II.2}$$

The absorption coefficient of gases is usually expressed as the product of absorption cross section, $\sigma(\lambda)$, and the number density, N, of the absorbers:

$$\alpha_{gases}(\lambda) = \sigma(\lambda).N \tag{II.3}$$

In fact, different molecules and atoms absorb radiation of different wavelengths that is the absorption spectrum. Hence, the optical absorption sensing method consists in monitoring the output light intensity changes according to the spectral characteristic of the absorption coefficient of the substance to be sensed. Therefore, the transmission spectra in the output of the waveguide show peaks at specific wavelengths equivalent to the molecule or atom absorption lines in the absorption spectra. Figure II.1shows absorption spectra of several gases and liquid solutions [46].

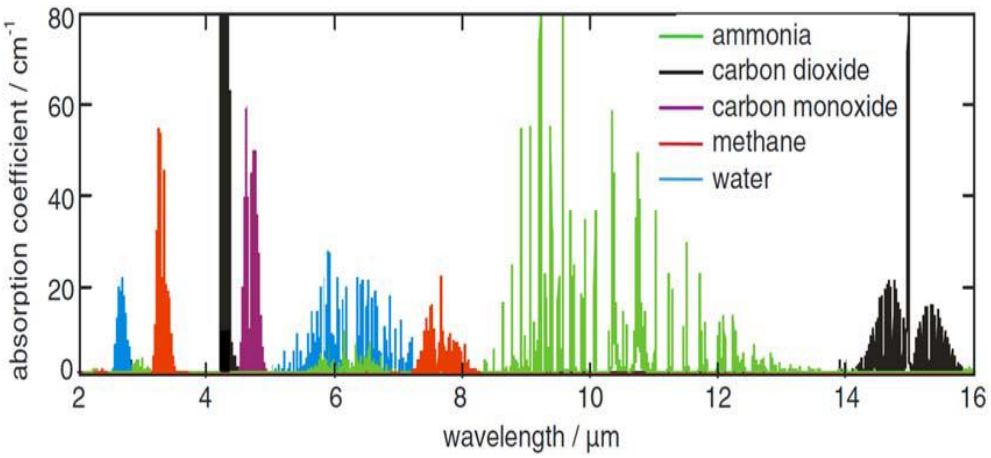

Figure II.1: Absorption spectra of five atmospheric gases [46].

II.2.2. Fluorescence

In fluorescence-based detection, the intensity of the fluorescence indicates the concentration of the target as well as their existence. We can just measure the intrinsic fluorescence of the target analyte or a change in fluorescence of an indicator dye by the analyte, with the determined concentration, referred to as the quench case [4]. In the latter case, the probe molecule can be immobilized onto the waveguide surface and placed in the evanescent field of the integrated optics sensor [45]. Fluorescence phenomena are related to an energetic transition from an excited state to a lower energy level producing photon emission. When a molecule absorbs electromagnetic energy, it travels to an excited energy level. Depending on the incident electromagnetic wavelength, the molecule reaches a well-defined energy level. The intensity of an absorption band can be explained by the term of oscillator strength f [47].

$$f = 4.315 \times 10^{-19} . \int \varepsilon_{\upsilon} . d\upsilon \qquad \text{(II.4)}$$

Where ε_{υ} is the molar extinction coefficient at the frequency υ.

The recombination of the molecule or atom from a high energy level to a low one can be happening in diverse way. In the majority cases, the emitted light has a longer wavelength, and therefore lower energy, than the absorbed radiation. However, when the absorbed electromagnetic radiation is intense, it can lead to emission of radiation having a shorter wavelength than the absorbed radiation. The emitted radiation can also be of the same wavelength as the absorbed radiation, named "resonance fluorescence".

The fluorescence quantum efficiency is defined as:

$$\emptyset_F = \frac{N^0_{L-P}}{N^0_{P-A}} \quad \text{(II.5)}$$

Where
$N^0_{L-P}$is the number of the photons emitted during the process of relaxation, $N^0_{P-A}$is the number of the photons absorbed by the molecule.An example of integrated optical fluorescence multichannel biosensor has been studied in [48].

II.2.3. Raman scattering

The Raman spectroscopy is one of the widely-used spectroscopic techniques and becoming increasingly important in a broad range of scientific disciplines categorized into distinct application areas such as materials science, biotechnology, pharmaceuticals, forensic science and photonic devices [49].Scattering of light by molecules can be devised in Rayleigh scattering, or Raman scattering. In Rayleigh scattering, the photon's energy and the state of the molecule after the scattering events are unchanged. Hence, it does not contain much information on the structure of molecular states [50]. In Raman scattering, molecule can transfer the energy to the photon and the photon can transfer the energy to the molecule. Thus, scattered photons and incident photons have no equal energies. The missing energy is transferred to the molecule, which conducts to the formation of phonons. Furthermore, when the scattered photon has less energy than the incident photon, the process is defined as Stokes scattering. In contrast, when the scattered photon has more energy than the incident photon, the process is known as anti-Stokes scattering. Hence, the photon acquires vibrational energy from the atoms/molecule and is scattered with a higher energy, Figure II.2. Red and blue shifts caused by Stokes and anti-Stokes scattering, successively, provide information about vibrational, rotational, and other low frequency transitions in molecules. Raman spectroscopy can be used to study liquid, gaseous and solid samples.

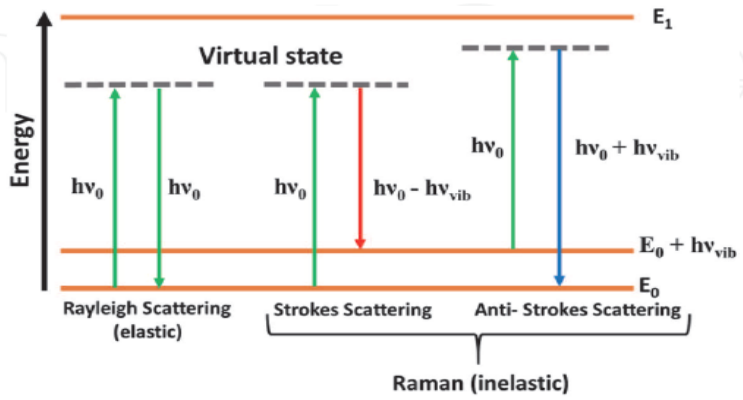

Figure II.2: Energy level diagram for Rayleigh and Raman scattering [51].

Light scattering can be measured whichever by the attenuation of the incident signal, after traveling the sample, or by measuring the intensity of the light scattered by the sample at a particular angle to the incident beam.

Raman signals are usually weak and require powerful sources and sensitive detectors. Surface enhanced Raman spectroscopy is a technique where molecules experience much higher scattering efficiencies when adsorbed on metal nanoparticles or irregular metal surfaces, this technique is non-destructive tool for biochemical sensing [52]. In addition to that, when the incident light becomes very intense, the optical properties of the medium change, leads to an increase in the amount of the emitted photons exited by other scattered photons, that is the Stimulated Raman scattering, this is very important for photonic sensors [53, 54].An example of optical waveguide Raman sensor is illustrated in figure II.4. The laser beam passes through waveguide and illuminated the sample containing a mixture of molecules. By investigating the scattered light from the Raman spectra, each type of molecule within the sample can be distinguished [55].

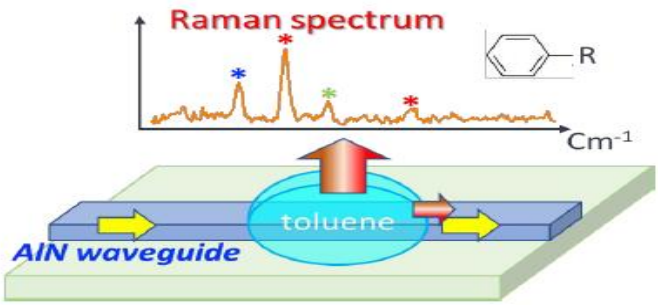

Figure II.3: Scattered light reveals the sample's Raman molecular fingerprint [55].

II.2.4. Effective index change in guiding structures

Photonic detection of biochemical substances is based on the change of the effective refractive index of the guided mode in the existence of biomolecules approximately of the detector area. Therefore, the amount of the refractive index modification is associated to the quantity of the light-matter interaction.

In an optical guiding configuration, the variation of the effective index of the propagating mode can be produced, either, by change of thickness of an adlayer on the waveguide, constituted by adsorbed or bound molecules, or by change of the refractive index of the homogeneous cover, Figure II.4.

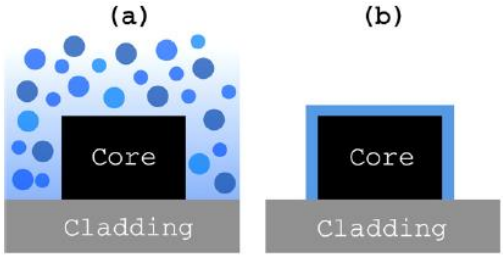

Figure II.4: (a) Homogeneous sensing, (b) surface sensing [44].

II.2.4.1. Homogeneous sensing

In homogeneous sensing, the effective refractive index of the guided mode changes suitable to the cover medium refractive index changes. This change of the effective index allows the measure of concentration of a varied continuum of biochemical species generally existing in a solution. In this case, a liquid or solid material serving as a cover medium of the optical waveguide. The sensitivity, S_h, can be evaluated as [27]:

$$S_h = \frac{\partial n_{eff}}{\partial n_c}\Big|_{n_c=n_c^0} = \frac{2n_c^0}{Z_0 P}\iint_C |E(x,y)|^2 dxdy = \frac{2n_c^0 \iint_\infty |E(x,y)|^2 dxdy}{Z_0 P}\Gamma_C' \quad \text{(II.6)}$$

Where

$$P = \iint_\infty \left[\left(\vec{E} \times \overrightarrow{H^*} + \vec{E}^* \times \vec{H}\right).z\right]dxdy \quad \text{(II.7)}$$

In the equation (II.6), Z_0 is the free space impedance, n_{eff} the effective refractive index of the guided mode, n_c is the refractive index of the solution, n_c^0 is the refractive index of the aqueous solution without the molecules, E and Hare the electric and magnetic field vectors, respectively, and Γ_C' is the optical field intensity confinement factor in the cladding region, defined as follows [27]:

$$\Gamma_C' = \frac{\iint_C |E(x,y)|^2 dxdy}{\iint_\infty |E(x,y)|^2 dxdy} \quad \text{(II.8)}$$

C and ∞ are the integration domains.

II.2.4.2. Surface sensing

Surface sensing is based on the fixation of selective biomolecules by an adlayer receptor surface deposited on the waveguide. Therefore, the selective molecules causes change in the thickness of the thin adlayer which causes changes of the effective refractive index of the guided mode as [27]:

$$\Delta n_{eff} = \frac{n_m^2 - (n_c^0)^2}{Z_0 P}\iint_\Sigma |E(x,y)|^2 dxdy \quad \text{(II.9)}$$

Where n_m is the refractive index of the immobilized thin film, Σ denotes the functionalized surface. The sensitivity of the waveguide for surface sensing is defined as follows [27]:

$$S_h = \frac{\partial n_{eff}}{\partial \rho}\Big|_{n_c=n_c^0} \quad \text{(II.10)}$$

Where ρ is the thickness of the immobilized receptor thin film.

II.3. Integrated optical sensors configurations

Among the various optical sensing devices, refractive index sensors have emerged as promising technology in the past few years. Refractive index sensors allow label-free, in real time and direct detection of the molecular interaction at a dielectric interface. In both bulk and surface sensing, the change of the refractive index of the cover or the thickness of the adlayer guides to the change of the effective refractive index of the guided mode. These optical changes have to be altered into a functional signal. To this purpose, numerous photonic sensor configurations have been proposed over the past decades, for biosensing applications, such as Mach–Zehnder interferometers (MZIs), microring resonators (MRRs), Bragg grating resonators and directional Couplers. Generally, it exist two different types of optical readout: the intensity and wavelength readout. For example, photonic chemical sensors based on optical absorption, are characterized by intrinsic intensity readout, because the change of the absorption coefficient is directly linked to the output optical intensity, according to the Beer-Lambert law [3]. However, Wavelength interrogation and intensity interrogation are two frequent configurations applied to evanescent field biosensors such as surface plasmon resonance or planar waveguide based sensors.

II.3.1. Integrated optical interferometers

In an interferometry biochemical sensor, the guided wave is divided into two single mode waveguides by a Y-junction, the first waveguide represents the sensing arm witch containing the sample, the second waveguide is considered as a reference, without sample. In the sensing arm, the evanescent field of the guided mode interacts with the analyte causes changes in its effective refractive index, resulting in a phase shift, depending on the substance concentration. After a certain distance, the two beams recombine again and cause a constructive or destructive interference at the output. Two typical configurations exist for integrated optical interferometers: the Mach–Zehnder interferometer (MZI) and the Young interferometer (YI).

II.3.1.1. Mach-Zehnder interferometers

Many types of Mach-Zehnder interferometers can exist according to the type of waveguides constituting the two arms, stripe waveguide, rib waveguide, buried waveguide, slot waveguide. In the case of a MZI sensor Figure II.5, if any optical phase shift is applied to the guided mode in the sensing arm, light will be combined at the output Y-branch exhibiting an output optical power equal to the input optical power. If an optical phase delay is applied in the sensing arm, the optical output power will be different from the input one. According to Eq. 12, the output intensity (I_{out}) is a periodically oscillating function of the phase change difference ($\Delta\varphi$) of the beams from the two arms:

$$I_{out} = I_{in} \cos\left(\frac{\Delta\varphi}{2}\right)^2 \tag{II.11}$$

The phase shift $\Delta\varphi$caused by the change of the effective refractive indexΔn_{eff}at the wavelength λ is defined as:

$$\Delta\varphi = \frac{2\pi}{\lambda}\Delta n_{eff} L \tag{II.12}$$

Where, L is the effective detection length of the sensing arm.

The sensitivity of the Mach-Zehnder interferometer for bulk and surface sensing are defined, respectively, as follows:

$$S_h = \frac{2\pi L}{\lambda}\left(\frac{\partial n_{eff}}{\partial n_c}\right) \tag{II.13}$$

$$S_s = \frac{2\pi L}{\lambda}\left(\frac{\partial n_{eff}}{\partial \rho}\right) \tag{II.14}$$

Where, n_{eff} is the effective index of the propagating mode, n_c is the cladding medium refractive index, and $\rho$is the thickness of adlayer deposited on the interface between de core and the cover medium of the waveguide.

In the configuration MZI using the slot waveguide, the sensing arm is constituted of a slot waveguide with strong light intensity confinement. This configuration significantly improves the light–matter interaction yielding to a higher sensitivity of the sensor [22].

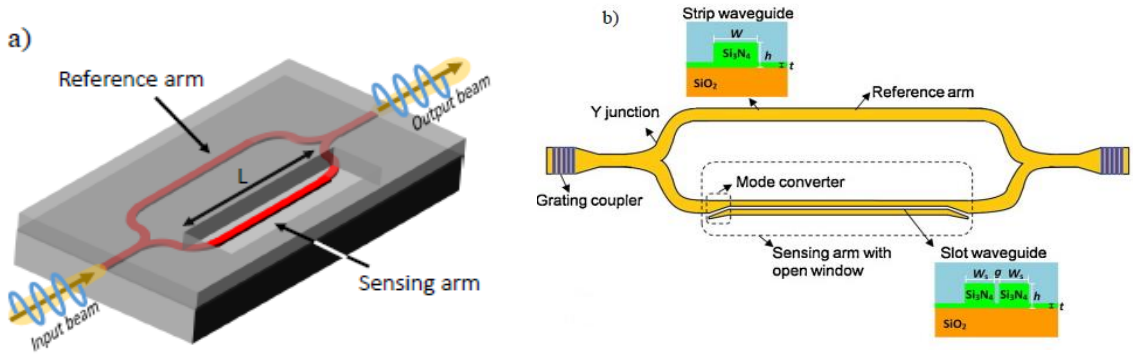

Figure II.5: a) A standard MZI configuration [56], b) Mach-Zehnder interferometer biosensor based on slot waveguide [22].

II.3.1.2. BiMW configuration

In Bimodal waveguides BiMW, Figure II.6, light from a coherent source in TE polarization is coupled into a ridge waveguide supporting a single transversal mode. After some distance, this mode is coupled into another waveguide which supports two transversal modes. Due to the vertical asymmetry of the junction, the fundamental mode of the first waveguide splits in two, the fundamental and the first order mode, which are propagating until the output of the structure. The fundamental mode would feebly influenced by the bio-interaction. Whereas the first order mode will be intensely influenced by the analyte refractive index variations [57].The modes propagate with different velocities and create an interference pattern at the exit, which intensity distribution depends on the physical parameters of the structure and, in particular, on the refractive index of the cladding layer through the interaction with the evanescent field. This intensity distribution is monitored using a photodetector array [58].

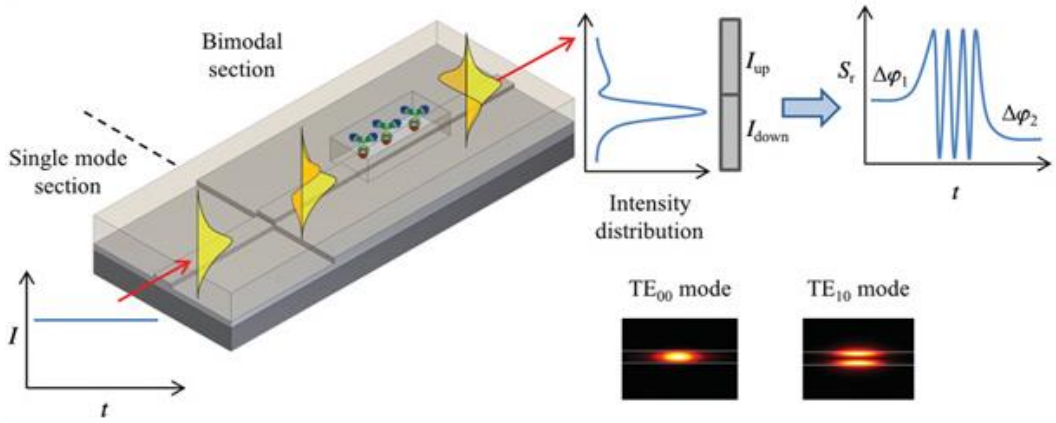

Figure II.6: BiMW interferometer, with the TE_{00} and TE_{10} mode profiles and the output detection scheme [58, 59].

II.3.1.3. Optical Young interferometer

In this configuration, because of the optical phase shift occurred in the sensing arm, resulting of the existing analyte, an interference pattern is formed in the CCD camera from both reference and sensing arms, Figure II.7. The following relation specifies the phase shift:

$$\Delta\varphi(t) = \frac{2\pi}{\lambda}\left[\frac{d.x}{f} - \left(n_{eff,s}(t) - n_{eff,R}\right).L\right] \quad \text{(II.15)}$$

Where, $d$is the space between the sensing and the reference arms, $f$is the distance between the output of the sensor structure and the CCD camera, and x is the position of the interference on the screen.

When the analyte interacts with the evanescent field in the sensing arm, we can deduce the phase shift at the interference pattern on the screen.

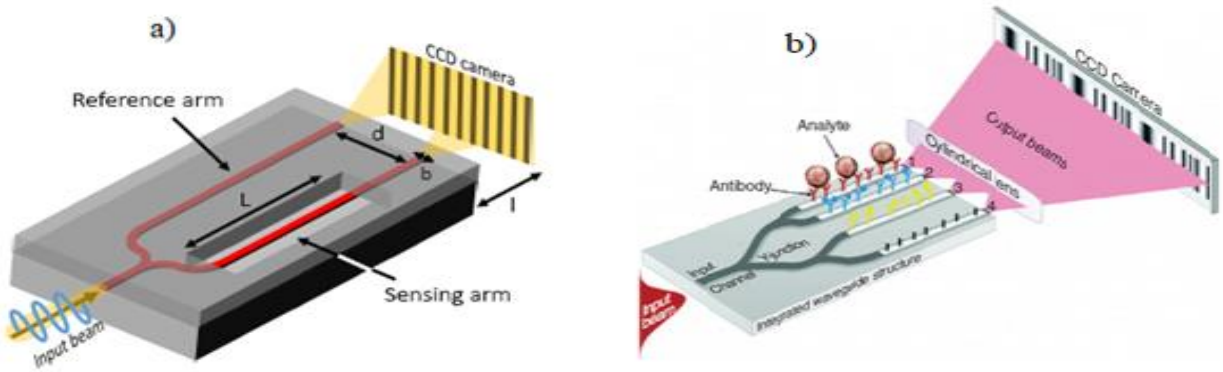

Figure II.7: a) The YI configuration [22], b) Four-channel Young interferometer [13].

In addition to that, a four-channel Young interferometer based waveguides was developed for bioanalytical applications, Figure II.7.b). This configuration is highly sensitive and has low Limit of Detection LOD [13].

II.3.1.4. Interferometry biosensor based on slab optical waveguide

This kind of photonic sensor is based on the planar optical waveguide. During the propagation of the transversal monomode in the slab waveguide, the evanescent field propagating above the core interacts with the substance to be sensed, inducing changes in the effective refractive index of the propagating mode. The effective refractive index depends on physical and geometrical parameters of the slab waveguide. Hence, a planar waveguide based optical sensor is susceptible both to homogeneous and surface refractive index changes [60].

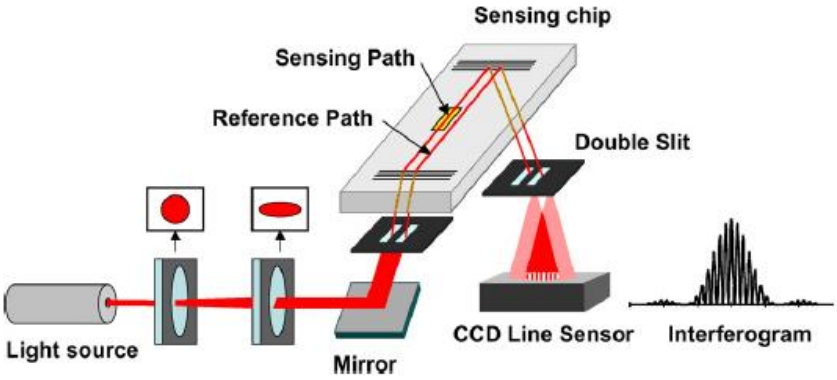

Figure II.8: Optical system of the interferometry biosensor system [60].

II.3.1.5. Birefringent waveguide based biosensor

The basic principle of the birefringent waveguide biosensor is the interference between the TE and TM orthogonally polarised beams. In fact, when the reaction between the antibody and antigen occurs, during the excitation of light, the difference in refractive index between the core and the sensing surface increases. This refractive index change in the waveguide in turn causes a change in birefringence between the two orthogonal polarizations TE and TM induced from the light source. A phase difference between the two polarizations is converted into a phase shift by the birefringence measurement system. Continuous real-time monitoring of the phase delay allows us to determine the amount of antibody–antigen reaction taking place, Figure II.9.

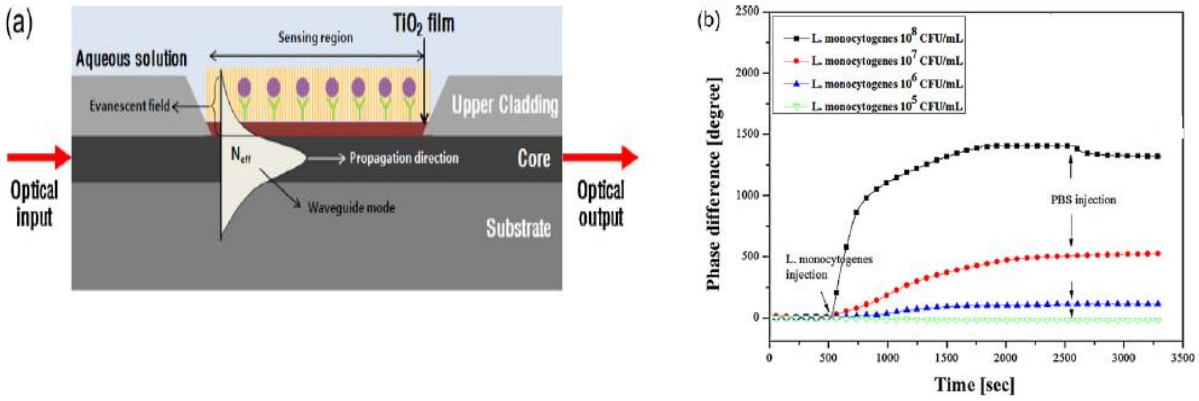

Figure II.9: (a) Waveguide sensor platform for antigen–antibody detection, (b) phase difference comparison between bimolecular concentrations [61].

II.3.2. Grating-coupler sensors

A Bragg grating is a periodic perturbation of the waveguide refractive index along the direction of propagation. More recent application of Bragg gratings is the realization of integrated optical sensors based on those structures; in this case, submicronic grating periods are demanded. A propagation of the light within such waveguide is observed, if the phase-matching condition (II.16) is satisfied.

$$n_{\text{eff}} = \sin\theta + m\frac{\lambda}{\Lambda} \tag{II.16}$$

WhereΛ is the grating period, $\theta$is the incident angle of the light and m is the diffraction order.

From this equation, it is clearly that a variation of the effective refractive index, with the presence of gases or biochemical molecules, will influence the resonance wavelength or the resonance angle. Therefore, Bragg grating based biosensors can be realized with two arrangements: the angular configuration and the wavelength configuration. It is worth to note that we can put the Bragg grating at the interfaces core/cover, core/substrate, or at both interfaces.

II.3.2.1. Grating-based biosensors with angular configuration

In the angular arrangement, the resonance angle is scanned using a laser source of fixed wavelength. The sample can be rotated to find the coupling angle and to determine the shift of the resonance angle induced by the bioreactions happening in the sensing area, where the grating can be an input coupler or an output coupler of light, Figure II.10. A position-sensitive photodetector or CCD line sensor detects the coupling or out coupling angle depending on the layer thickness or the effective refractive index, respectively [62].

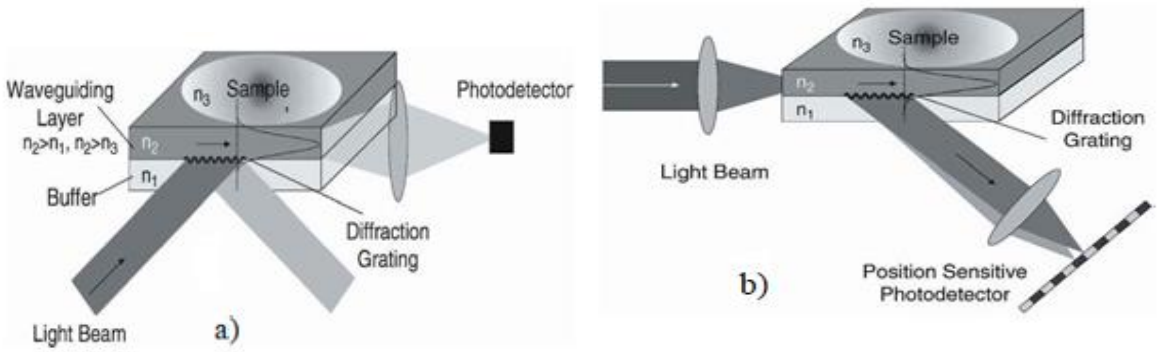

Figure II.10: Input grating coupler sensor and Output grating coupler sensor [4].

Using the grating as a reflector also, has been developed in grating-based biosensors, Figure II.11 (a). In such configuration, light of a tunable laser is coupled into the waveguide and a resonance wavelength is reflected back after interaction with the grating. A biochemical reaction on the grating surface makes resonance wavelength shift in the spectrum, Figure II.13 (b). Height sensitivity has been verified using $Si/SiO_2/Si_3N_4$ waveguide [63].

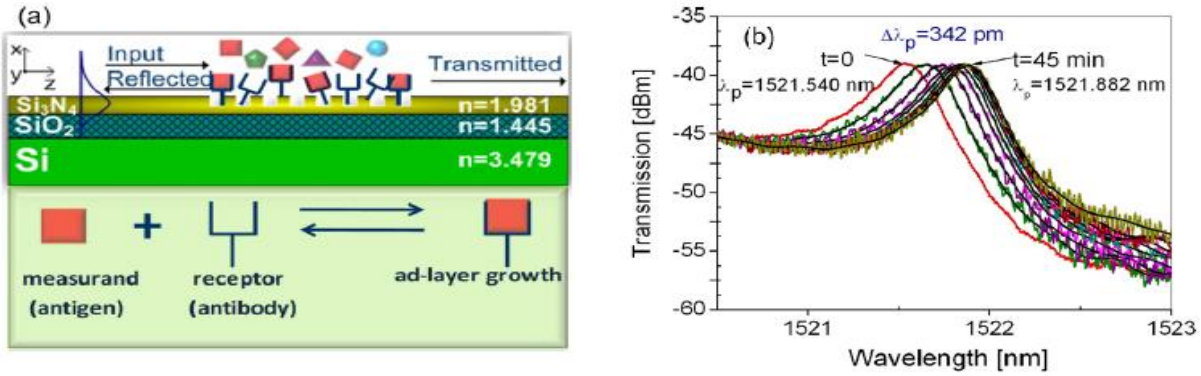

Figure II.11: (a) Schematic of the grating-based biosensor wavelength interrogation for label-free surface biosensing,(b) Transmission spectra of the label-free sensing of grating-based biosensor wavelength interrogation [63].

II.3.2.2. Grating-based biosensors with the wavelength interrogation

In the wavelength configuration, at fixed angle of incidence, a tunable laser is involved to scan the resonance wavelength. The operating principle of configuration is shown in Figure II.12 [64]. A collimated beam from tunable laser is incident at fixed angle θonto a waveguide deposited on a transparent substrate. When the coupling conditions are satisfied, the light beam is coupled into the waveguide, propagates, and a detector at the end of the waveguide monitors the intensity of light according to the source wavelength. When the grating is exposed to the analytes, adsorption causes changes in the refractive index at the grating surface and results in a shift in the laser beam coupling conditions, detected as wavelength λ shift. Several wavelength interrogation optical sensors have been investigated for the detection of different kinds of analytes [65].

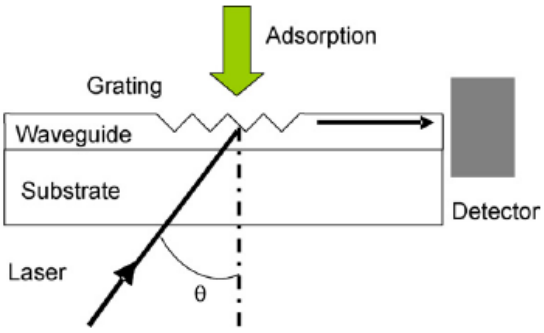

Figure II.12: Input grating coupler with the wavelength-interrogated approach [64].

II.3.3. Evanescent-Wave Sensors

Photonic-based biochemical sensors use light that is confined in its waveguide. As the light propagates into the waveguide by total internal reflection, part of the electromagnetic field called evanescent field, extends beyond the surface into the external medium, where it can interact with analytes. The evanescent field that is exponentially decays with distance, dependent on the physical properties of the materials and the geometrical design of the sensor. In fact, the analytes disturb the evanescent field and modify the cover refractive index and/or induce an optical absorption. The variation in the cover refractive index induces the shift of resonant peaks in photonic resonators, while the optical absorption reduces the light transmission intensity traveling the waveguide [66]. Hence, we can classify photonic biosensors into refractive index based sensors and absorption based sensors.

II.3.3.1. Refractive index-based sensors

For applications of homogenous sensing, the sensing signal can be employed to determine the refractive index of the sample as compared to a reference sample. For applications of surface sensing, the specific capture of biomolecules at the sensor surface results in a local change in refractive index which produces a sensing signal that enables quantification of the biomolecules in the sample, Figure II.13. Hence, two definitions of the sensitivity are used in biochemical sensing applications, the first one is the bulk sensitivity and the other is surface sensitivity:

$$S_{bulk} = \frac{\Delta\lambda(\Delta\phi)}{\Delta n_{sample}} \tag{II.17}$$

$$S_{surf} = \frac{\Delta\lambda(\Delta\phi)}{\Delta t_{adlayer}} \tag{II.18}$$

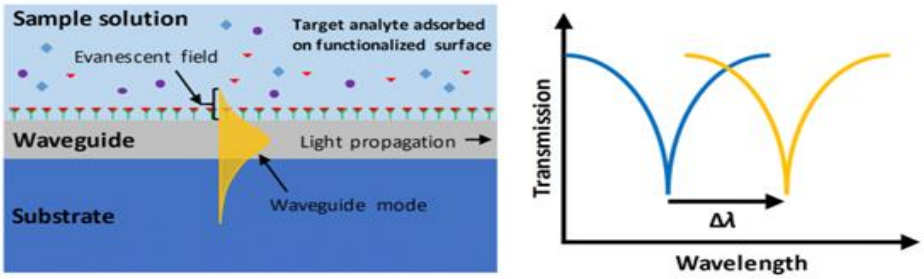

Figure II.13: Refractive index-based sensor with surface functionalized and the wavelength shift induced by the analyte [66].

II.3.3.2. Absorption-based sensors

In the absorption-based sensors, the evanescent field probes the vibrational transitions of the surrounding environment directly**.** Optical absorption of the vibrational transitions, in accordance with the Beer–Lambert law, provides an absorption spectrum that can be used for spectroscopic identification; Figure II.14. This kind of sensing is compatible for environmental monitoring, medical diagnostics, chemical, biological, radiological, nuclear, and explosive agents [67].

For absorption-based sensors, the sensitivity refers to bulk sensitivity in most cases as no surface functionalization is implemented, and is defined as the change in absorbance or transmittance divided by the change in sample concentration C:

$$S_{bulk} = \frac{\Delta R(\Delta T)}{\Delta C_{sample}} \qquad \text{(II.19)}$$

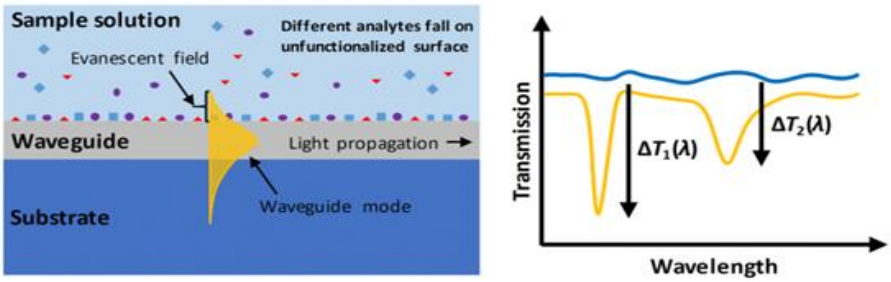

Figure II.14: Absorption-based sensor without surface functionalization and the sensor transmission spectrum [66].

II.3.4. Surface plasmon resonance based sensors

This technique is the current optical method using for chemical and biological sensing. The detecting principle is based on sensing the refractive index change of substances by the

surface plasmon wave. In fact, when the source wave and the surface plasmon wave are matched, a conversion of light energy to surface plasmons occurs (resonance).the excitation of SPW corresponds to an attenuation of the reflected light intensity, which results in a sharp dip in the reflected light intensity. The resonance occurs when de relationship (II.20) is satisfied. Furthermore, the resonance can be happening in a specific wavelength or in a specific angle of incidence. When the refractive index at the surface of the metal change by biomolecules, the propagation constant of the surface plasmon change, this results in change in the resonant angle or resonant wavelength, and a shift in the position of the SPR dip occurs, Figure II.15 (b).

$$\beta_{sp} = \sin\theta \frac{2\pi}{\lambda} n_{\mathrm{p}} \tag{II.20}$$

Where, λ is the source wavelength, $n_{\mathrm{p}}$is the refractive index of the prism, θ is the incidence angle and $\beta_{sp}$is the constant of propagation of surface plasmon wave.

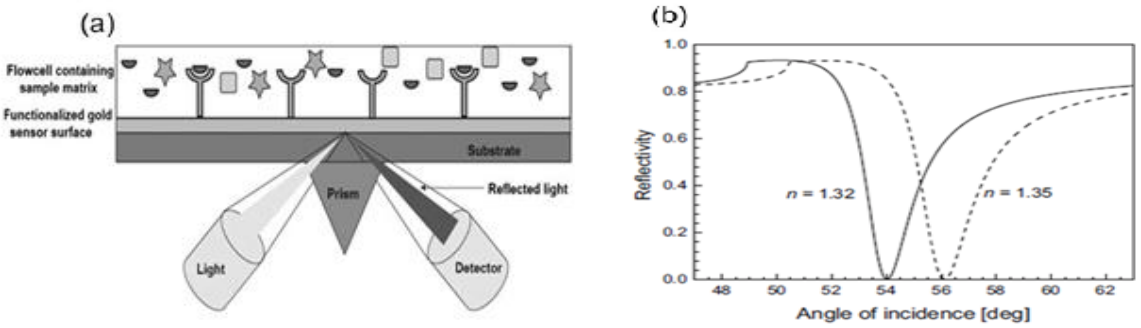

Figure II.15: (a) Kretschmann configuration in SPR sensor [68]. (b) Reflectivity for the system for two different biomolecules [4].

II.3.5. Ring resonator optical sensors

II.3.5.1. Ring resonator coupled to a bus waveguide

The basic principle of a ring resonator optical sensor involves in measuring the resonance wavelength shift caused by the change of the effective refractive index of the propagating mode in the existence of the analyte to be identified. The configuration of the ring resonator optical sensor comprises a bus waveguide coupled to a ring resonator, Figure II.16. Thus, if we choose the operational wavelength identical to one of the resonant wavelength symbolizing the ring resonator, then, the change of the refractive index of the cover medium will induce a shift$\Delta\lambda$ in the resonant wavelength. Hence, small refractive index changes can be calculated as [69]:

$$\Delta\lambda = \frac{\lambda_{res}}{n_g} . \Delta n_s . \Gamma_{cov} \tag{II.21}$$

Where:

$\Gamma_{cov}$is the field confinement factor in the cover. $\Delta n_s$is the change in the refractive index, n_g is the group index and λ_{res} is the resonant wavelength of ring resonator.

$$n_g = n_{eff} - \lambda_0 \frac{\delta n_{eff}}{\delta \lambda} \tag{II.22}$$

$$\lambda_0 = \frac{2\pi r n_{eff}}{m} \tag{II.23}$$

Wherer is the ring radius, $n_{eff}$is the modal effective index, m is an integer and $\lambda_0$is the modal wavelength.

The sensitivity $S_{SR}$of the sensor based on ring resonator coupled to a straight waveguide is defined as: S_w (homogeneous S_h or surface S_s sensitivities) as:

$$S_{SR} = FSR_S \frac{\lambda S_w}{n_g} \tag{II.24}$$

Where

$FSR_S$is the free spectral range of sensing cavity. $S_w$is the straight waveguide sensitivity, either, homogeneous sensitivity or surface sensitivity.

The effective length (L_{eff}) is related to the Q factor by:

$$L_{eff} = Q \frac{\lambda}{2\pi n} \tag{II.25}$$

Where

n is the refractive index of the ring resonator.

Noting that, high Q factor designate low optical losses and high peak resolution, which means high sensitivity [70].

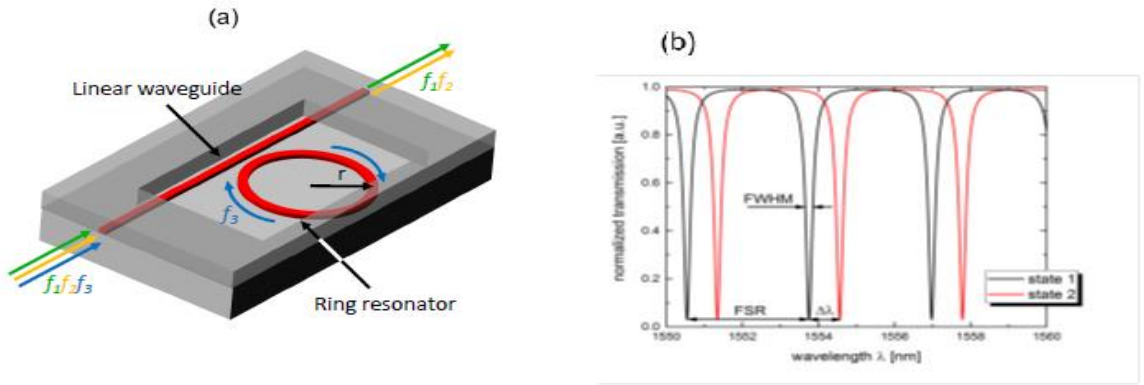

Figure II.16: (a) Straight waveguide coupled ring resonator optical sensor [21]. (b) The resonant peak shift due to the cover refractive index change [69].

II.3.5.2. Silicon slotted microring resonator sensor

Ring resonators based on slot waveguides exhibit ultra-high performance for photonic bio-chemical sensing. As we have seen in the previous chapter, slot waveguide is capable to strongly confine light in a nanoscale low refractive index material, allowing a high interaction with chemical and biochemical substances. By joining the improvement of light matter interaction of the slot waveguide with the sensitivity of the microring resonator, small changed of the refractive index of adjacent medium can be detected [71]. This is appeared as a resonance shift at the transmission spectrum, figure.17.

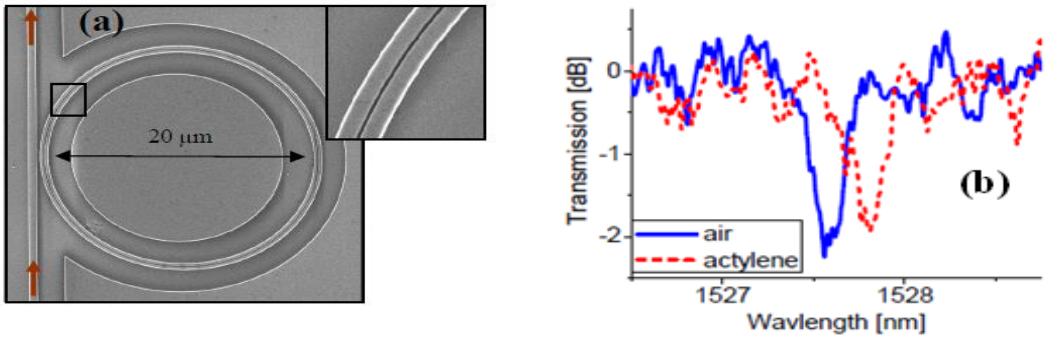

Figure II.17: Slotted microring resonator sensor (a). (b), Transmission spectra in the presence and absence of acetylene gas [71].

II.3.6. Directional couplers based photonic sensors

Directional couplers base photonic sensors, as shown in Figure II.18 (a), are constituted of two collinear waveguides in the waist, with divergent inputs and outputs. One waveguide is the sensing arm; the other waveguide is the reference arm. Noting that, the two waveguides are symmetric and have the same physical and geometrical characteristics. The sensing principle of photonic sensors based on directional couplers is founded on the power modulation at the waveguide's outputs, accomplished by a phase shift between the two propagating modes in both waveguides. In fact, when the propagation constants of the two modes are identical, a complete coupling energy between the two waveguide is occurred (P_1=0, P_2=P_0). The existence of any substances in the coupling area will change the refractive index the surrounding medium, producing change of the effective refractive index of the propagated mode in the sensing arm. In this case, the coupling efficiency is not complete. By measuring the change of power in the two outputs, it is possible to identify a particular substance and its concentration. The optical powers (P_1, P_2) at the output section (x = L) can be calculated by the following expressions:

$$P_2 = \frac{sin^2\left\{\left[(kL)^2+\left(\frac{\Delta\beta}{2}\right)^2\right]\right\}^{\frac{1}{2}}}{1+\left(\frac{\Delta\beta}{2}\right)^2} P_0 \quad \text{(II.26)}$$

$$P_1 = P_0 - P_2 \quad \text{(II.27)}$$

Where: k is the coupling coefficient and L is the device length.

The sensitivity of such configurations can be calculated as:

$$S = n_{clad(REF)} \frac{\partial T}{\partial n_{clad}}\Big|_{n_{clad}=n_{clad(REF)}} \quad \text{(II.28)}$$

Where: $T$is the transmittance recorded at the output of the reference arm. $n_{clad}$is the refractive index of the analyte and $n_{clad(REF)}$is the reference value of the analyte refractive index when the derivative is calculated.

Nothing that the use of slot waveguides in directional coupler base optical sensors, improve highly the sensitivity [10], Figure II.18 (b).

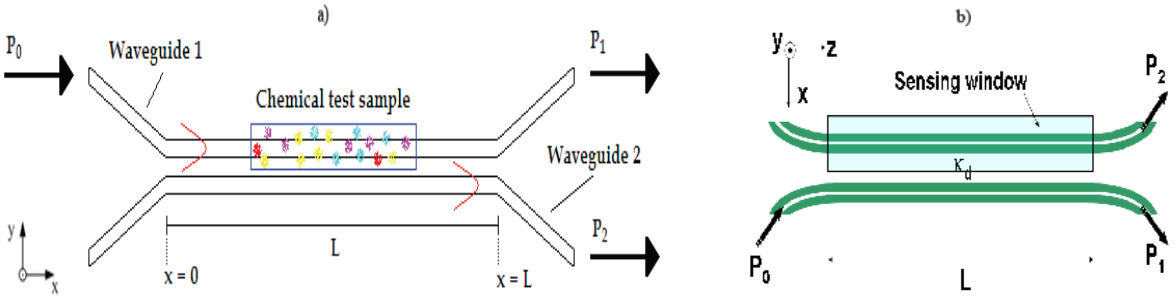

Figure II.18: Directional coupler base photonic sensors [3, 10].

II.4. Conclusion

In this chapter, a diversity of photonic sensing mechanisms were described, including optical absorption, fluorescence, Raman scattering and detecting of refractive index changes. In the purpose to transform optical variable induced by such optical-sensing mechanism into a useful signal, several integrated photonic sensors configurations have been described suitable for different applications, such as integrated optical interferometers, microring resonators, Bragg grating resonators and directional couplers.

CHAPTER III:

PHOTONIC WAVEGUIDES MODELING

III.1. Introduction

The term photonics reflects the growing bind between optics and electronics. If electronics can be considered as the discipline that describes the flow of electrons, photonics deals with the control of photons. The term photonics also reflects the importance of the photon nature of light in describing the operation of many optical devices. Furthermore, integrated photonics refers to the fabrication and integration of several photonic components on a common planar substrate. The integrated optical waveguides are the essentials elements for all integrated photonic devices, systems and instruments. Since, they play the role of guiding, splitting, switching, coupling, multiplexing and de-multiplexing of optical waves [72].

In this chapter, firstly, slab optical waveguides will be studied with two approaches. The optical ray approach, which permits us to define the dispersion equation of the guided modes, and the Maxwell's equations approach, used to determine wave equations and their solutions, as well as, the solutions of electromagnetic field. Furthermore, the influence of the physical and geometric parameters and the wavelength of the source on the propagation constants and the cutoff frequencies will be studied. Secondly, the effective index method (EIM) will be used for calculating the field distribution of quasi-TE and quasi-TM modes in the embedded-strip waveguide.

III.2. Optical waveguides classification

An optical waveguide is a light canal made of dielectric material embedded in another dielectric material of lower refractive index. The light is transported through the inner medium by multiple total internal reflections at the boundaries without radiating into the surrounding medium. We can categorize the integrated optical waveguide, essentially, according to their geometry and their dimensions where the light is restricted. For one dimension 1D waveguide, the confinement of optical wave occurs in a single direction. For two 2D dimensions waveguide, the confinement acts in two directions. Finally, for three dimensions 3D waveguide the confinement is in the three directions. According to their geometry, optical waveguide can be classified in three buildings: slab or planar waveguides, cylindrical or fiber waveguides and rectangular or channel waveguides, the latter kind of waveguides have different geometries (strip, rib, strip-loaded waveguide, Embedded-strip waveguide, Buried channel waveguide, Slot waveguide and arrow waveguide) [73, 74], as presented Figure III.1. We note that the most integrated photonic waveguides are fabricated by Ti: LiNbO3, GaAs and AlGaAs, InP, polymer and SOI materials.

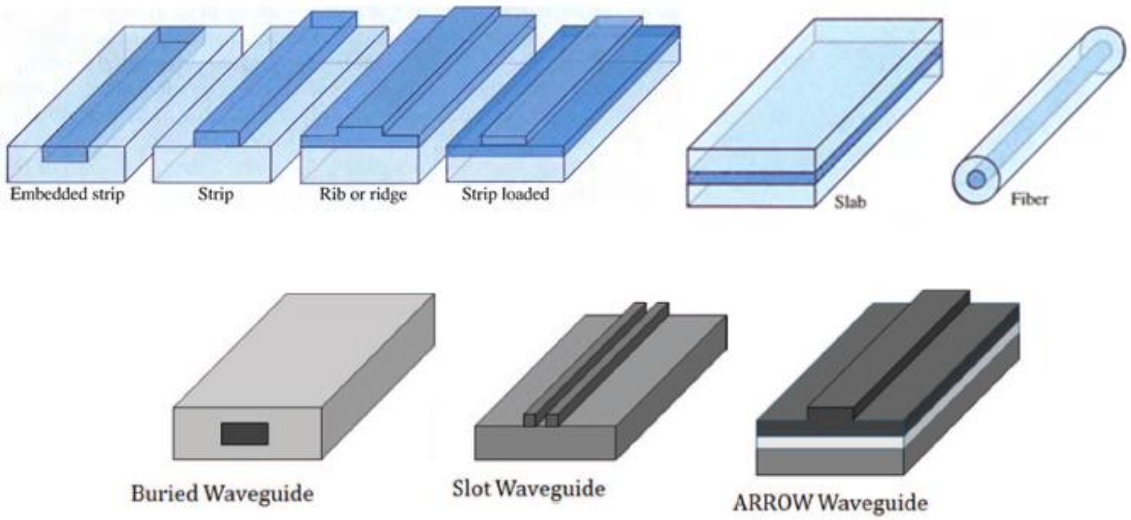

Figure III.1: Optical waveguide geometries [73, 74].

III.3. Modeling of integrated optical waveguides

Integrated optical waveguides are generally, examined by two famous methods. The Ray approach and the Electromagnetic approach. In the ray method, the light is considered as line that is perpendicular the light's wavefronts, this method used for planar waveguides; give us information about the propagation modes. However, in the electromagnetic method, the light is considered as electromagnetic waves and the Maxwell equations must be used. This approach gives us complete information about modes and electromagnetic distributions in different regions of the waveguide.

III.3.1. Guided modes in the step index slab waveguides

III.3.1.1. Ray method

The first condition for a mode to be propagating along the optical waveguide by total internal reflections at the two opposite interfaces, Figure III.2, is: $0 < \theta_z < \frac{\pi}{2} - \theta_s$.

Where:

$\theta_s = \sin(\frac{n_s}{n_f})^{-1}$ is the critical angle at the interface core/substrate. n_f , n_s are the core, substrate refractive indices, respectively, and θ_z is the refraction angle.

The second condition for a guided mode to be organized on constructive interference is that the total transversal phase shift of a two counterpropagating waves in a complete round trip

should be an integer number of 2π. Only a discrete number of angles fulfill that condition, and these will correspond to the propagation angles of guided modes.

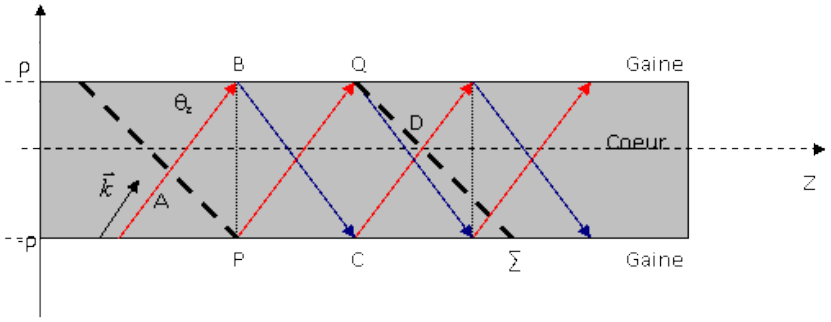

Figure III.2: Total reflection in the interfaces of an asymmetrical waveguide.

The difference in phase shifts for the two counter-propagating waves is described by [75]:

$$\varphi_{ABCD} - \varphi_{PQ} = 2\varphi_{AB} + \varphi_{R1} + \varphi_{R2} = 2m\pi \tag{III.1}$$

Where

$$\begin{aligned} \varphi_{AB} &= \varphi_{CD} = \left(\frac{2\pi}{\lambda} n_f\right)(2\rho \sin\theta_z) \\ \varphi_{BC} &= \varphi_{PQ} = \left(\frac{2\pi}{\lambda} n_f\right)\left(\frac{2\rho}{\sin\theta_z}\right) \end{aligned} \tag{III.2}$$

$$\begin{aligned} &(\varphi_R)_i = -2\arctan\left(g_i \frac{\sqrt{N^2 - n_i^2}}{\sqrt{n_f^2 - N^2}}\right) \quad ; \quad i = c(\text{cover}), s(substrate) \\ &g_i = 1 \quad : \quad for \quad TE \\ &g_i = \frac{n_f^2}{n_i^2} \quad : \quad for \quad TM \end{aligned} \tag{III.3}$$

Where: $N = n_f \cos\theta_z$, ρ is the thickness of the slab waveguide.

n_f, n_c and n_s are the core, cover and substrate indices, respectively.

We substitute (III.2) and (III.3) in (III.1), and taking in consideration g_i, we get:

$$\left(\frac{4\pi\rho}{c} f\sqrt{n_f^2 - N^2}\right) - \arctan\left(\frac{\sqrt{N^2 - n_c^2}}{\sqrt{n_f^2 - N^2}}\right) - \arctan\left(\frac{\sqrt{N^2 - n_s^2}}{\sqrt{n_f^2 - N^2}}\right) - m\pi = 0 \tag{III.4}$$

For TE modes.

$$\left(\frac{4\pi\rho}{c} f\sqrt{n_f^2 - N^2}\right) - \arctan\left(\frac{n_f^2}{n_c^2}\frac{\sqrt{N^2 - n_c^2}}{\sqrt{n_f^2 - N^2}}\right) - \arctan\left(\frac{n_f^2}{n_s^2}\frac{\sqrt{N^2 - n_s^2}}{\sqrt{n_f^2 - N^2}}\right) - m\pi = 0 \quad \text{(III.5)}$$

For TM modes.

The dispersion equations describe discrete values of the effective refractive index *N* for guided modes corresponding to the mode number *m*, where the guided mode with *m = 0* is called the fundamental mode while those with $m \neq 0$ are called higher-order modes. The number of modes that can be supported by a slab waveguide depends on the thickness of the core, refractive indices and the wavelength of the source. Each mode has its cutoff frequency f_c below which waveguiding cannot occur.

By putting $N = n_f \cos\theta_z$ in the equations (III.4) and (III.5), we can deduce the dispersion equations of TE and TM modes function of the refraction angles Θ_z, which are the propagation angles of guided modes.

Cut-off frequencies for TE modes

$$f_m = \frac{c\left(\arctan\left(\frac{\sqrt{n_s^2 - n_c^2}}{\sqrt{n_f^2 - n_s^2}}\right) + m\pi\right)}{\left(4\pi\rho\sqrt{n_f^2 - n_s^2}\right)} \quad \text{(III.6)}$$

Cut-off frequencies for TM modes

$$f_m = \frac{c\left(\arctan\left(\frac{n_f^2}{n_c^2}\frac{\sqrt{n_s^2 - n_c^2}}{\sqrt{n_f^2 - n_s^2}}\right) + m\pi\right)}{\left(4\pi\rho\sqrt{n_f^2 - n_s^2}\right)} \quad \text{(III.7)}$$

Where $n_s > n_c$

The Ray method cannot determine the electromagnetic field distribution in each region of the waveguide.

III.3.1.2. Electromagnetic method

The study of integrated photonic waveguides by the electromagnetic approach allows us to find the distribution of the E and M fields in each region of the waveguide, in addition to the

information concerning the number of propagated modes, the cutoff frequency and the propagation constant of each mode.

In this chapter, the studied planar waveguide is instituted in each region by a uniaxial anisotropic crystal. Theirs tensors of permittivity are $\bar{\bar{\varepsilon}}_f$,$\bar{\bar{\varepsilon}}_c$ and $\bar{\bar{\varepsilon}}_s$respectively. The cover, the core and the substrate of the waveguide have no losses and no magnetic permeability, Figure III.3.

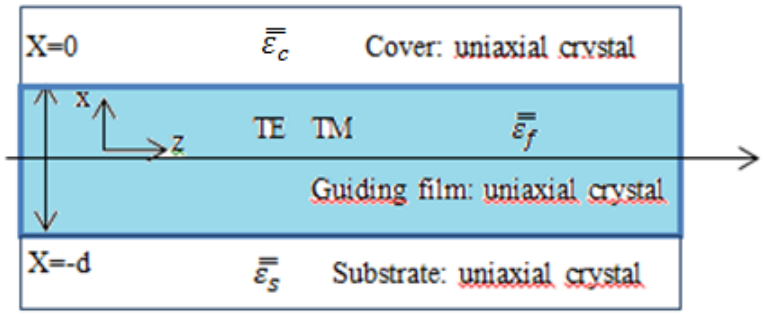

Figure III.3: Birefringent planar optical waveguide.

Among the four Maxwell's equations, we choose the two followings:

$$\vec{\nabla} X \vec{E} = -j\omega\mu_0\vec{H} \tag{III.8}$$

$$\vec{\nabla} X \vec{H} = j\omega\varepsilon_0\varepsilon_i\vec{E} \tag{III.9}$$

Where

$$\varepsilon_i = \begin{bmatrix} \varepsilon_i & 0 & 0 \\ 0 & \varepsilon_i & 0 \\ 0 & 0 & \varepsilon_{iz} \end{bmatrix} = \varepsilon_0 \begin{bmatrix} n_i^2 & 0 & 0 \\ 0 & n_i^2 & 0 \\ 0 & 0 & n_{iz}^2 \end{bmatrix}$$

It is worth noting that$\varepsilon_0$and $\mu_0$are; the dielectric constant and the magnetic permeability of vacuum, i=c, f, s (cover, film, substrate).

Seeing the following time harmonic wave:

$$\vec{E} = E(x).e^{j(\omega t-\beta z)} \tag{III.10}$$

$$\vec{\mathrm{H}} = H(x).e^{j(\omega t-\beta z)} \tag{III.11}$$

By using Cartesian coordinate system (x, y, z), equations (III.8) and (III.9) give six separate equations as follows:

$$\begin{cases} \frac{\partial E_z}{\partial y} - \frac{\partial E_y}{\partial z} = -j\omega\mu_0 H_x \\ \frac{\partial E_x}{\partial z} - \frac{\partial E_z}{\partial x} = -j\omega\mu_0 H_y \\ \frac{\partial E_y}{\partial x} - \frac{\partial E_x}{\partial y} = -j\omega\mu_0 H_z \\ \frac{\partial H_z}{\partial y} - \frac{\partial H_y}{\partial z} = j\omega\varepsilon_0\varepsilon_i E_x \\ \frac{\partial H_x}{\partial z} - \frac{\partial H_z}{\partial x} = j\omega\varepsilon_0\varepsilon_i E_y \\ \frac{\partial H_y}{\partial x} - \frac{\partial H_x}{\partial y} = j\omega\varepsilon_0\varepsilon_{iz} E_z \end{cases} \quad \text{(III.12)}$$

In a planar waveguide there is no variation of the field according the *y* direction, means that:

$$\frac{\partial E_z}{\partial y} = \frac{\partial E_x}{\partial y} = \frac{\partial H_z}{\partial y} = \frac{\partial H_x}{\partial y} = 0 \quad \text{(III.13)}$$

The set of the six equations becomes:

$$\begin{cases} -\frac{\partial E_y}{\partial z} = -j\omega\mu_0 H_x \\ \frac{\partial E_x}{\partial z} - \frac{\partial E_z}{\partial x} = -j\omega\mu_0 H_y \\ \frac{\partial E_y}{\partial x} = -j\omega\mu_0 H_z \\ -\frac{\partial H_y}{\partial z} = j\omega\varepsilon_0\varepsilon_i E_x \\ \frac{\partial H_x}{\partial z} - \frac{\partial H_z}{\partial x} = j\omega\varepsilon_0\varepsilon_i E_y \\ \frac{\partial H_y}{\partial x} = j\omega\varepsilon_0\varepsilon_{iz} E_z \end{cases} \quad \text{(III.14)}$$

III.3.1.2.1. TE modes

In this case, the electric field has only one component in the *y* axis, whereas, the magnetic field component is zero in this axis, so:

$$\begin{cases} E_x = E_z = 0 \rightarrow \frac{\partial E_x}{\partial z} = \frac{\partial E_z}{\partial x} = 0 \\ H_y = 0 \rightarrow \frac{\partial H_y}{\partial z} = \frac{\partial H_y}{\partial x} = 0 \end{cases} \quad \text{(III.15)}$$

A. Wave equation of TE modes

We replace the latter simplifications in the set of six equations (III.14), we get:

$$j\beta E_y = -j\omega\mu_0 H_x \quad \text{(III.16)}$$

$$\frac{\partial E_y}{\partial x} = -j\omega\mu_0 H_z \quad \text{(III.17)}$$

$$-j\beta H_x - \frac{\partial H_z}{\partial x} = j\omega\varepsilon_0\varepsilon_i E_y \quad \text{(III.18)}$$

Where: $\frac{\partial}{\partial z} = -j\beta$

From equations (III.16) and (III.17), we can obtain the magnetic field components in terms of the E_y component:

$$-\frac{\beta E_y}{\omega\mu_0} = H_x \tag{III.19}$$

$$\frac{j}{\omega\mu_0}\frac{\partial E_y}{\partial x} = H_z \tag{III.20}$$

Substituting H_x and $\frac{\partial H_z}{\partial x}$into the equation (III.18), we obtain the wave equations in each region:

$$\begin{cases} \frac{\partial^2 E_y}{\partial x^2} + \left(k_0^2\varepsilon_f - \beta^2\right)E_y = 0; \text{film} \\ \frac{\partial^2 E_y}{\partial x^2} - (\beta^2 - k_0^2\varepsilon_c)E_y = 0; \text{cover} \\ \frac{\partial^2 E_y}{\partial x^2} - (\beta^2 - k_0^2\varepsilon_s)E_y = 0; \text{substrate} \end{cases} \tag{III.21}$$

Where:

$$k_0^2 = \omega^2\varepsilon_0\mu_0$$

$$\gamma_f = \sqrt{k_0^2\varepsilon_f - \beta^2}$$

$$\gamma_c = \sqrt{\beta^2 - k_0^2\varepsilon_c}$$

$$\gamma_s = \sqrt{\beta^2 - k_0^2\varepsilon_s}$$

Equation (III.21) is the wave equation of TE modes in each region (cover, film and substrate).

B. Solutions of the wave equations in the three regions for TE modes

The guided TE modes have exponentially decaying behavior in the cladding and the substrate, and a sinusoidal behavior in the film region. The explicit solutions of the electric field in different layers are expressed as:

$$E_y = \begin{cases} Ae^{-\gamma_c x} & ; x \geq 0 \\ Be^{-j\gamma_f x} + Ce^{j\gamma_f x} & ; 0 > x > -d \\ De^{\gamma_s x} & ; x \leq -d \end{cases} \tag{III.22}$$

In addition, the solutions of the wave equations could fulfill the boundary conditions at the two interfaces, *x=0* and *x=-d*. This requires that the lateral electric and magnetic fields must be continuous at the dielectric discontinuities.

At *x=0*:

$$\begin{cases} E_{yc}(0) = E_{yf}(0) \\ H_{zc}(0) = H_{zf}(0) \end{cases} \quad \text{(III.23)}$$

At *x=-d*:

$$\begin{cases} E_{yf}(-d) = E_{ys}(-d) \\ H_{zf}(-d) = H_{zs}(-d) \end{cases} \quad \text{(III.24)}$$

The previous conditions give us four linear relations connecting all the waveguide parameters.

$$\begin{cases} A - B - C + 0.D = 0 \\ -\gamma_c A + j\gamma_f B - j\gamma_f C + 0.D = 0 \\ 0.A + Be^{+j\gamma_f d} + Ce^{-j\gamma_f d} - De^{-\gamma_s d} = 0 \\ 0.A - j\gamma_f e^{+j\gamma_f d} B + j\gamma_f e^{-j\gamma_f d} C - \gamma_s De^{-\gamma_s d} = 0 \end{cases} \quad \text{(III.25)}$$

To have no trivial solutions of this set of equations, the determinant should be zero. After cumbersome calculation, the characteristic equation for TE modes is obtained as:

$$k_0 d\sqrt{n_f^2 - N^2} = arctan\left(\sqrt{\frac{N^2 - n_s^2}{n_f^2 - N^2}}\right) + arctan\left(\sqrt{\frac{N^2 - n_c^2}{n_f^2 - N^2}}\right) + m\pi \quad \text{(III.26)}$$

The effective index of TE mode is given by: $N = \frac{\beta}{k_0}$

C. Field Distribution in each region for TE modes

By using the boundary conditions, we can determine the components of the electromagnetic field E_y , H_x and H_z in each region function of the constant A as follow:

$$E_y = \begin{cases} Ae^{-\gamma_c x} & ;\ x \geq 0 \\ A\left(cos\gamma_f x - \frac{\gamma_c}{\gamma_f} sin\gamma_f x\right) & ;\ 0 > x > -d \\ A\left(cos\gamma_f d + \frac{\gamma_c}{\gamma_f} sin\gamma_f d\right) e^{\gamma_s (x+d)} & ;\ x \leq -d \end{cases} \quad \text{(III.27)}$$

$$H_x = \frac{\beta A}{\omega\mu_0} \begin{cases} e^{-\gamma_c x} & ;\ x \geq 0 \\ \left(cos\gamma_f x - \frac{\gamma_c}{\gamma_f} sin\gamma_f x\right) & ;\ 0 > x > -d \\ \left(cos\gamma_f d + \frac{\gamma_c}{\gamma_f} sin\gamma_f d\right) e^{\gamma_s (x+d)} & ;\ x \leq -d \end{cases} \quad \text{(III.28)}$$

$$H_z = \frac{jA}{\omega\mu_0} \begin{cases} -\gamma_c e^{-\gamma_c x} & ;\ x \geq 0 \\ -\gamma_f \left(sin\gamma_f x + \frac{\gamma_c}{\gamma_f} cos\gamma_f x\right) & ;\ 0 > x > -d \\ \gamma_s \left(cos\gamma_f d + \frac{\gamma_c}{\gamma_f} sin\gamma_f d\right) e^{\gamma_s (x+d)} & ;\ x \leq -d \end{cases} \quad \text{(III.29)}$$

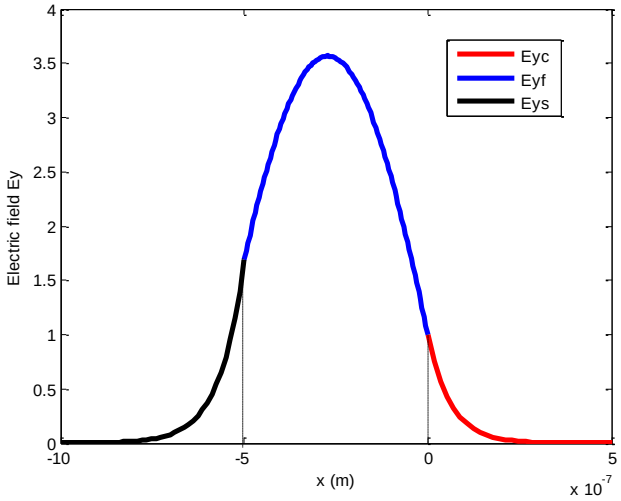

Figure III.4: TE electric field component (E_y) in three regions (cover, film and substrate) of slab waveguide (n_s= n_c =1.60, d=50 nm, $LiNbO_3$ as guiding film).

Figure III.4 represents the dominant component E_y in each region of the slab waveguide, where we are considered that the cover and the substrate are isotropic. Red and black curves represent evanescent fields in the cover and substrate region, respectively. However, blue curve represent electric field component in the core.

III.3.1.2.2. TM modes

In this case, magnetic field has only one component according the *y* axis, whereas, the electric field component is zero along this axis.

$$\begin{cases} H_x = H_z = 0 \rightarrow \frac{\partial H_x}{\partial z} = \frac{\partial H_z}{\partial x} = 0 \\ E_y = 0 \rightarrow \frac{\partial E_y}{\partial z} = \frac{\partial E_y}{\partial x} = 0 \end{cases} \quad \text{(III.30)}$$

A. Wave equation for TM modes

The same steps from TE modes are followed, we get:

$$j\beta H_y = j\omega\varepsilon_0\varepsilon_i E_x \quad \text{(III.31)}$$

$$\frac{\partial H_y}{\partial x} = j\omega\varepsilon_0\varepsilon_{iz} E_z \quad \text{(III.32)}$$

$$-j\beta E_x - \frac{\partial E_z}{\partial x} = -j\omega\mu_0 H_y \quad \text{(III.33)}$$

From equations (III.31) and (III.32) we can obtain the electric field components in terms of the H_y component:

$$\frac{\beta}{\omega\varepsilon_0\varepsilon_i}H_y = E_x \tag{III.34}$$

$$\frac{-j}{\omega\varepsilon_0\varepsilon_{iz}}\frac{\partial H_y}{\partial x} = E_z \tag{III.35}$$

Substituting E_x and $\frac{\partial E_z}{\partial x}$into equation (III.33) we obtain the wave equations of TM modes in each region:

$$\begin{cases} \frac{\partial^2 H_y}{\partial x^2} + \left(k_0^2\varepsilon_{fz} - \beta^2\frac{\varepsilon_{fz}}{\varepsilon_f}\right)H_y = 0\,; film \\ \frac{\partial^2 H_y}{\partial x^2} - \left(\beta^2\frac{\varepsilon_{cz}}{\varepsilon_c} - k_0^2\varepsilon_{cz}\right)H_y = 0; cover \\ \frac{\partial^2 H_y}{\partial x^2} - \left(\beta^2\frac{\varepsilon_{sz}}{\varepsilon_s} - k_0^2\varepsilon_{sz}\right)H_y = 0;\ substrate \end{cases} \tag{III.36}$$

Equation (III.36) is the wave equation of TM modes in each region (cover, film and substrate).

B. Solutions of the wave equations in the three regions for TM modes

The solutions of the magnetic field in each layer are expressed as:

$$H_y = \begin{cases} Ae^{-\gamma_c' x} & ;\ x \geq 0 \\ Be^{j\gamma_f' x} + Ce^{-j\gamma_f' x} & ;0 > x > -d \\ De^{\gamma_s' x} & ;x \leq -d \end{cases} \tag{III.37}$$

Where

$$\gamma_f' = \sqrt{k_0^2\varepsilon_{fz} - \beta^2\frac{\varepsilon_{fz}}{\varepsilon_f}}$$

$$\gamma_c' = \sqrt{\beta^2\frac{\varepsilon_{cz}}{\varepsilon_c} - k_0^2\varepsilon_{cz}}$$

$$\gamma_s' = \sqrt{\beta^2\frac{\varepsilon_{sz}}{\varepsilon_s} - k_0^2\varepsilon_{sz}}$$

The dielectric discontinuities in this case are:

At *x=0*:

$$\begin{cases} H_{yc}(0) = H_{yf}(0) \\ E_{zc}(0) = E_{zf}(0) \end{cases} \tag{III.38}$$

At *x=-d*:

$$\begin{cases} H_{yf}(-d) = H_{ys}(-d) \\ E_{zf}(-d) = E_{zs}(-d) \end{cases} \tag{III.39}$$

This conditions, giving place to four linear and homogenous equations that relate the constant parameters *A, B, C* and *D* and the propagation constant β.

After calculations, the characteristic equation for TM modes is obtained as follows:

$$k_0 d \frac{n_{fz}}{n_f}\sqrt{n_f^2 - N^2} = arctan\frac{n_{fz}n_f}{n_{cz}n_c}\sqrt{\frac{N^2-n_p^2}{n_f^2-N^2}} + arctan\frac{n_{fz}n_f}{n_{sz}n_s}\sqrt{\frac{N^2-n_s^2}{n_f^2-N^2}} + m\pi \quad \text{(III.40)}$$

C. Field Distribution of TM modes in each region

By using the boundary conditions, we can determine the constants and different components of the electromagnetic field as follow:

$$H_y = A\begin{cases} e^{-\gamma_c' x} & ; x \geq 0 \\ cos\gamma_f' x - \frac{n_f^2}{n_c^2}\frac{\gamma_c'}{\gamma_f'} sin\gamma_f' x & ; -d < x < 0 \\ \left(cos\gamma_f' d + \frac{n_f^2}{n_c^2}\frac{\gamma_c'}{\gamma_f'} sin\gamma_f' d\right) e^{\gamma_s'(x+d)} & ; x \leq -d \end{cases} \quad \text{(III.41)}$$

$E_x$and E_z can be determined from equations (III.34) and (III.35) respectively.

$$E_x = \frac{\beta A}{\omega\varepsilon_0\varepsilon_i}\begin{cases} e^{-\gamma_c' x} & ; x \geq 0 \\ cos\gamma_f' x - \frac{n_f^2}{n_c^2}\frac{\gamma_c'}{\gamma_f'} sin\gamma_f' x & ; -d < x < 0 \\ \left(cos\gamma_f' d + \frac{n_f^2}{n_c^2}\frac{\gamma_c'}{\gamma_f'} sin\gamma_f' d\right) e^{\gamma_s'(x+d)} & ; x \leq -d \end{cases} \quad \text{(III.42)}$$

$$E_z = \frac{-jA}{\omega\varepsilon_0\varepsilon_{iz}}\begin{cases} -\gamma_c e^{-\gamma_c' x} & ; x \geq 0 \\ -\gamma_f'\left(sin\gamma_f' x + \frac{n_f^2}{n_c^2}\frac{\gamma_c'}{\gamma_f'} cos\gamma_f' x\right) & ; -d < x < 0 \\ \gamma_s'\left(cos\gamma_f' d + \frac{n_f^2}{n_c^2}\frac{\gamma_c'}{\gamma_f'} sin\gamma_f' d\right) e^{\gamma_s'(x+d)} & ; x \leq -d \end{cases} \quad \text{(III.43)}$$

Where, the dielectric constant ε_i differs from region to region, as defined previously.

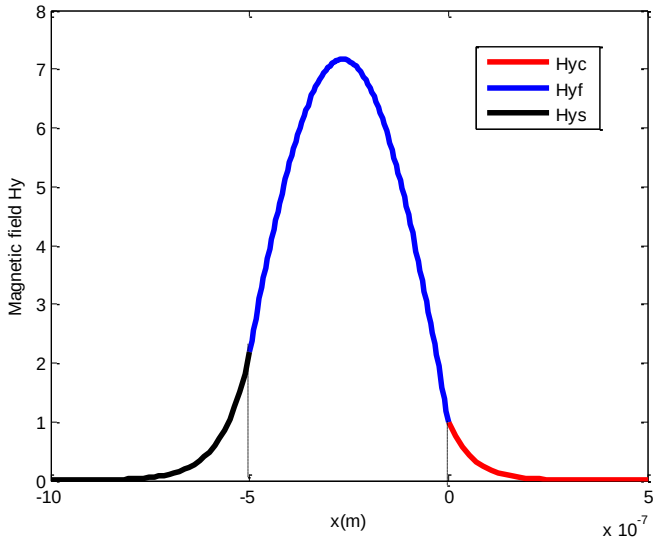

Figure III.5: TM_0 magnetic field components (H_y) in three regions (cover, film and substrate) of slab waveguide ($n_s = n_c = 1.60$, d=50 nm, $LiNbO_3$ as guiding film).

Figure III.5 represents the magnetic field component H_y in each region of the slab waveguide, where we are considered that the cover and the substrate are isotropic. Red and black curves represent evanescent fields in the cover and substrate region, successively. However, blue curve represent magnetic field component in the core.

III.3.1.2.3. Solutions of the characteristic equations for both TE and TM modes

The characteristic equations link the propagation constants of modes with the different parameters of the waveguide. We developed a program in Matlab, based on the bisection method, which allowed us to calculate the propagation constants of the fundamental and higher order modes of both TE and TM polarizations, as a function of the frequency, of the wavelength and the thickness of the waveguiding film. The developed program also allowed us to see the influence of the physical and geometrical parameters as well as the source's wavelength on the propagation constants and the cutoff frequencies of the guided modes. In fact, different values of these parameters will be introduced in the previous dispersion equations of both TE and TM modes via the program, which permits the calculation and the tracing of the effective refractive indices according to the frequency or the thickness of the waveguide core.

The slab waveguide consists essentially of a core of $LiNbO_3$ upper a glass substrate; the source's wavelength is 650 nm.

The physical parameters are chosen according to following table:

Table III.1: List of refractive indices used in the program with their correspondent materials [76].

Refractive index	Name of material
1.80	Lanthane flint dense LaSF30
1.628	Carbon disulfide, Quinoline, Vinylidene chloride.
1.48	Parafin, liquid, Crown glass (impure), Acrylic, Glycerine.
1.70	Flint glass
1.60	Polycarbonate, Epoxy, Polystyrene, Verre de germanium.
1.68	Barr &Stroud BS-39B
1.72	Glass: SF10, LaK10.

Figure III.6 represents the effective indices (propagation constants) versus frequency of TE_0, TE_1, TM_0 and TM_1 modes. The figure shows that, the effective indices of TE modes are greater than those of TM modes. Whereas, the cut off frequencies of the latter, are greater than those of TE modes. Furthermore, the effective indices of fundamental modes are greater than those of higher order modes. Whereas, cut off frequencies of the latter, are greater than those of fundamental ones. If the slab waveguide is symmetric, we note that TE and TM have the same cut off frequencies, Figure III.7.

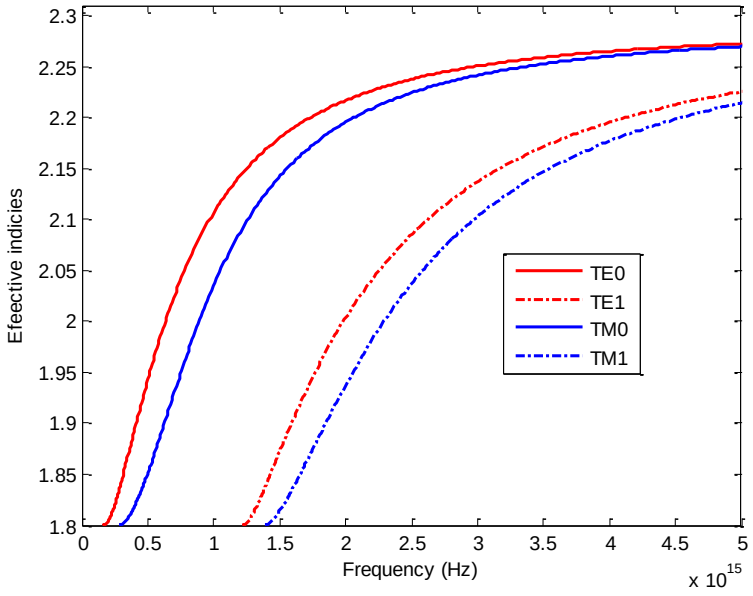

Figure III.6: Effective index according to the frequency of TE, TM modes in asymmetric planar waveguide, for (n_s=1.80, n_c =1.628, d=100 nm, $LiNbO_3$ as the core).

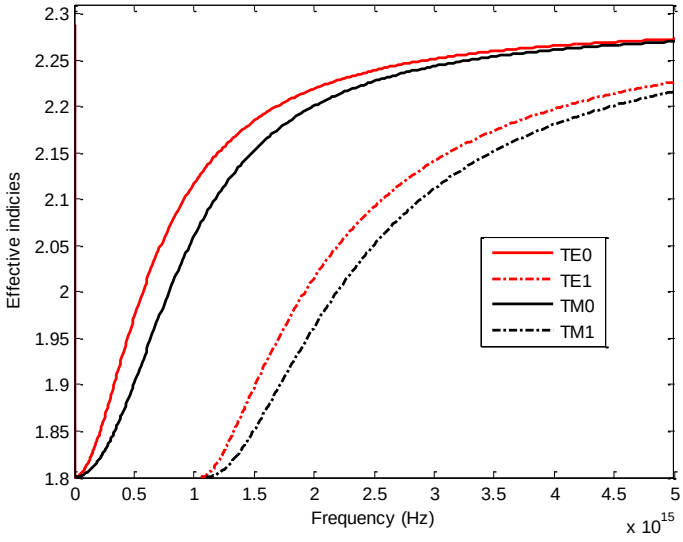

Figure III.7: Effective index versus frequency of TE, TM modes in symmetric planar waveguide, for (n_s=1.80, n_c =1.628, d=100 nm, $LiNbO_3$ as the core).

A. Influence of the geometrical parameter

Figures III.8 and III.9 show the propagation constants of the fundamental modes (TE_0, TM_0) as well as modes of order one (TE_1, TM_1), function of the frequency for different core's thicknesses values. The figures show that, the increase in the thickness of the core makes an increasing in the propagation constants of the modes as well as a reduction in their cut-off frequencies, especially for higher order modes. As a conclusion, the thickness of the core has significant impact in the choice of the frequency ranges of the propagated modes.

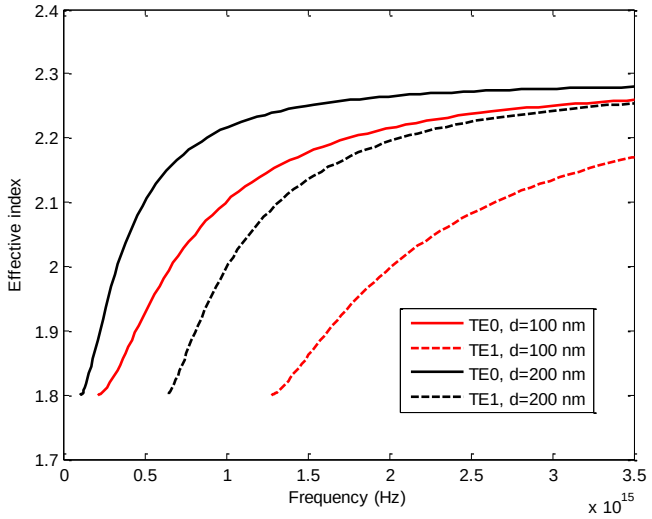

Figure III.8: Effective index versus frequency of TE_0 modes in slab waveguide for different core's thicknesses, (n_s=1.80, n_c =1.628, $LiNbO_3$ as the core).

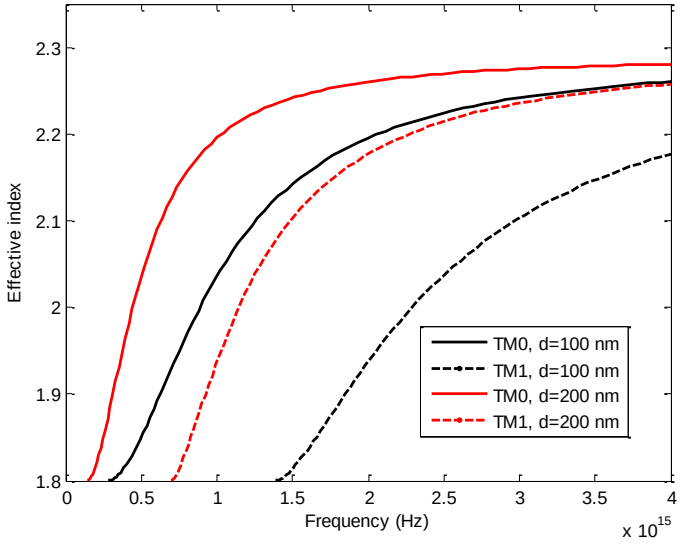

Figure III.9: Effective index versus frequency of TM modes in slab waveguide for different core's thicknesses, (n_s=1.80, n_c =1.48, $LiNbO_3$ as the core).

B. Influence of the source's wavelength

For different source's wavelengths, we illustrate de propagation constants of (TE_0, TE_1, TM_0 and TM_1) modes function of the core's thicknesses. As shown in Figures III. (10, 11), the increase in the source's wavelength induces a decrease in the propagation constants of the modes as well as an increase in theirs cut-off thicknesses, especially for higher orders modes.

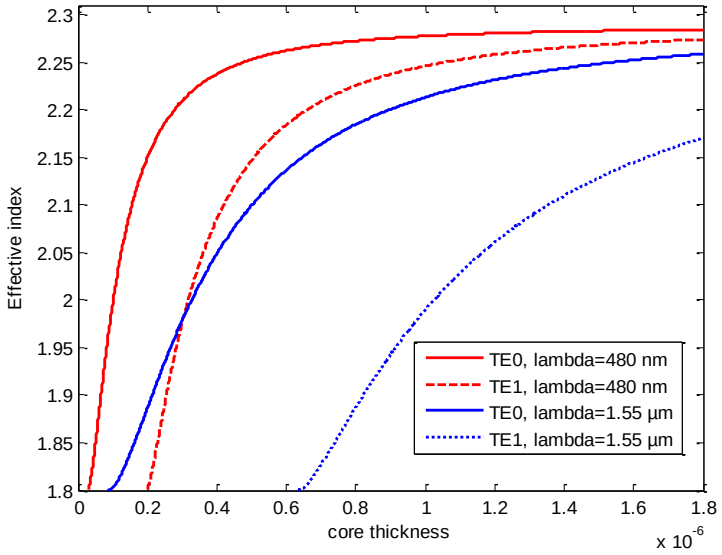

Figure III.10: Effective index versus core thickness of TE modes in slab waveguide for different source's wavelength, (n_s=1.80, n_p =1.628, d=100 nm, $LiNbO_3$ as the core).

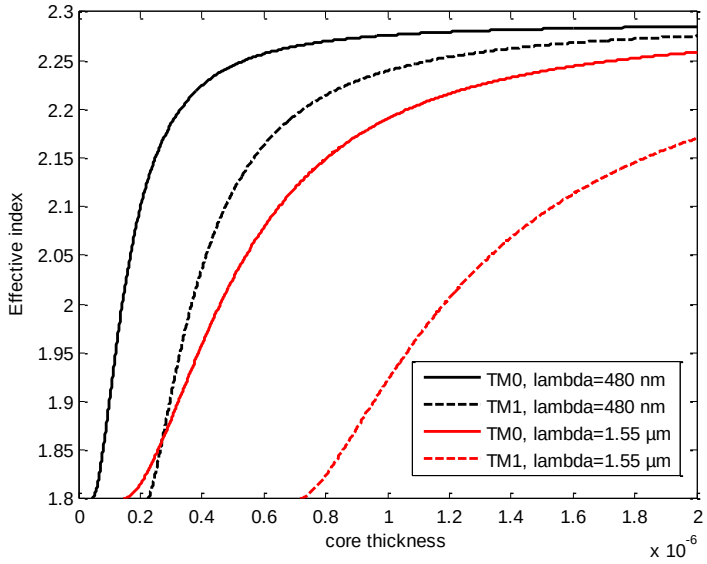

Figure III.11: Effective index versus core thickness of TM modes in slab waveguide for different source's wavelength, (n_s=1.80, n_p =1.628, d=100 nm, $LiNbO_3$ as the core).

C. Influence of the physical parameters

i. Influence of the cover refractive index

Changes in the cover refractive index do not have great influence on the propagated modes, and especially for TM modes, Figure III.13. Thus, the increase of the cover refractive index induces small decrease in cut-off frequencies of modes and neglected increase in theirs propagation constants, Figure III.12.

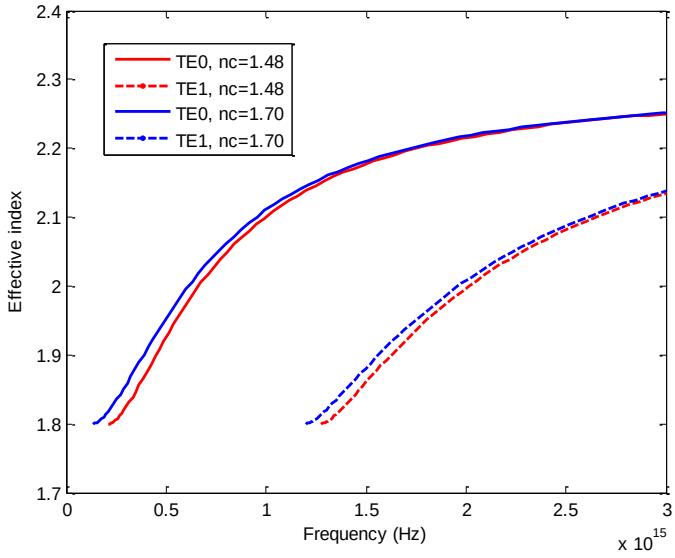

Figure III.12: Effective index versus frequency of TE_0 modes in slab waveguide for different cover refractive indices, (n_s=1.80, d =100 nm, $LiNbO_3$ as the core).

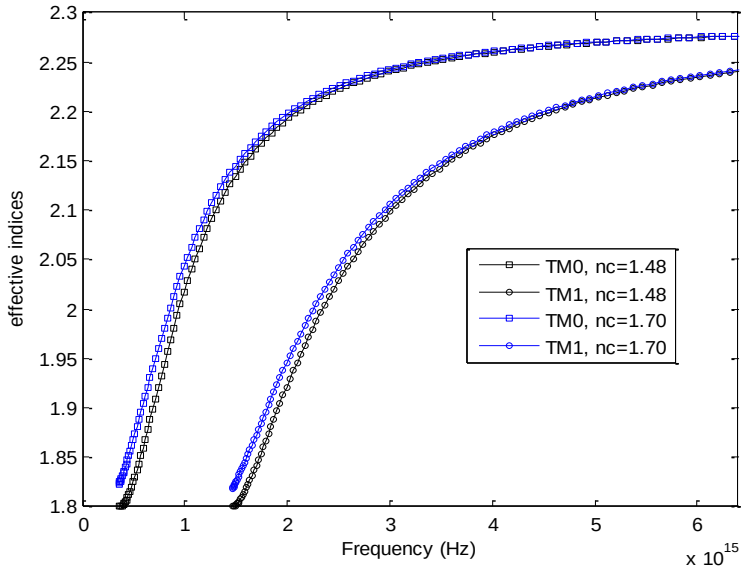

Figure III.13: Effective index versus frequency of TM modes in slab waveguide for different cover refractive indices, (n_s=1.80, d=100 nm, $LiNbO_3$ as guiding film).

ii. Influence of the substrate refractive index

Substrate refractive index changes do not have great influence on the propagation constants in higher frequencies (far from cut-off frequencies). However, its increase makes increasing of the cut-off frequencies of the guided modes and theirs propagation constants near to the cut-off frequencies, in both TE and TM cases, Figure III. (14, 15).

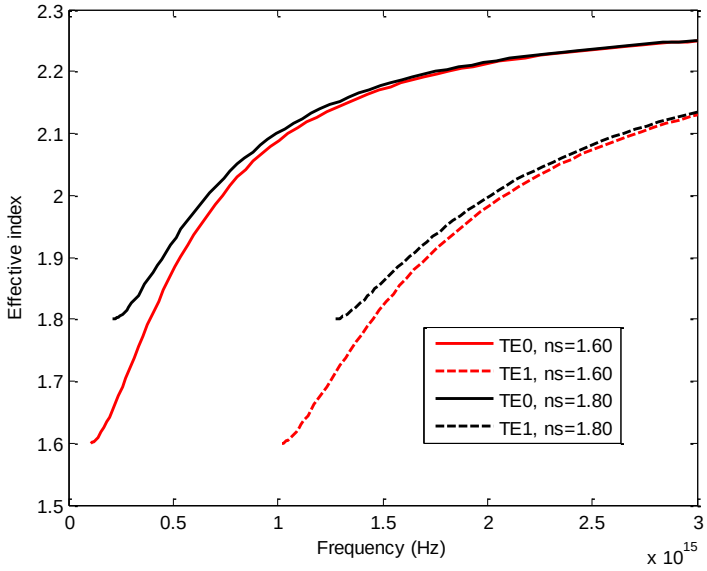

Figure III.14: Effective index versus frequency of TE_0 modes in slab waveguide for different substrate refractive indices, (n_p=1.48, d =100 nm, $LiNbO_3$ as guiding film).

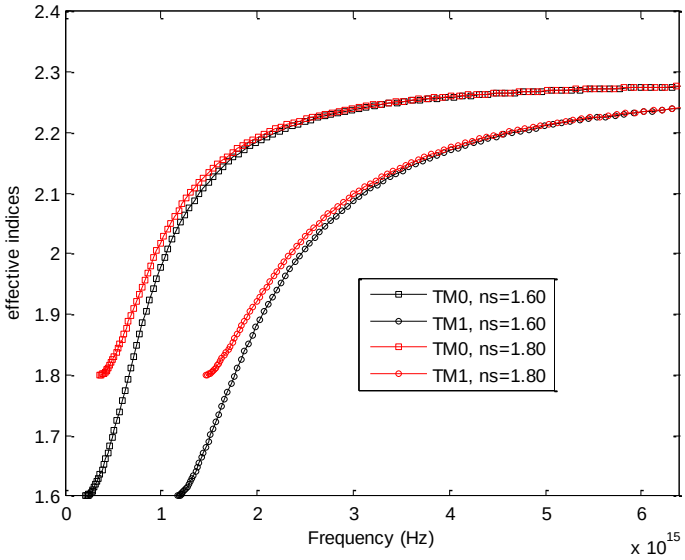

Figure III.15: Effective index versus frequency of TM modes in slab waveguide for different substrate refractive indices, (n_c=1.48, d=100 nm, $LiNbO_3$ as guiding film).

iii. Influence of the core refractive index

Figures III.16, III.17 show very clearly that small variations in the core refractive index induce great variations in the propagation constants of modes TE and TM and their cut-off frequencies. In fact, the increase of the core's refractive index induces an increase of the propagation constants and a decrease in the cut off frequencies. Notice that, higher order modes are more sensitive to the core's refractive index changes.

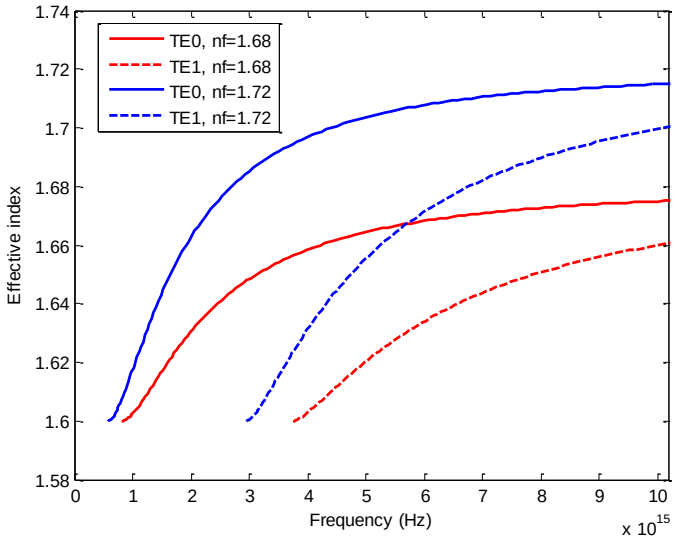

Figure III.16: Effective index versus frequency of TE modes in slab waveguide for different core refractive indices, (n_c=1.48, n_s=1.60, d=100 nm).

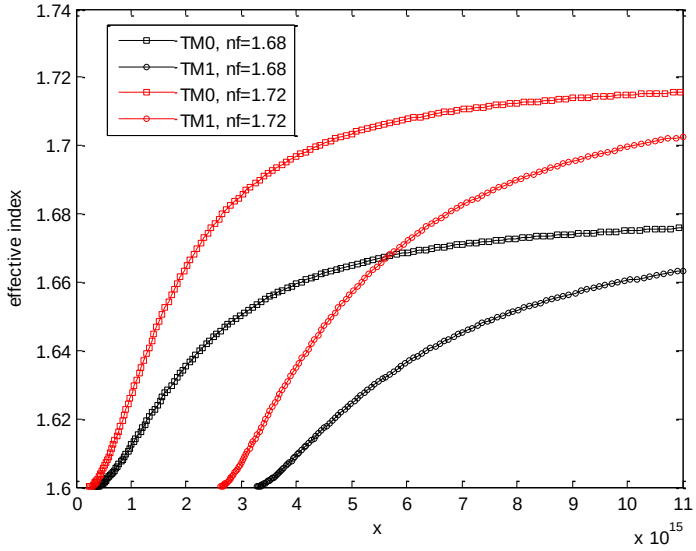

Figure III.17: Effective index versus frequency of TM modes in slab waveguide for different core refractive indices, (n_c=1.48, n_s=1.60, d=100 nm).

III.3.2. Modeling of channel waveguides by the Effective Index Method

In the rectangular integrated waveguides, there are two kinds of hybrid transversal electromagnetic modes. The quasi-TM mode mainly polarised along the x direction, named E_{mn}^{x} mode, and the quasi-TE modes mainly polarised along the y direction, termedE_{mn}^{y} mode [72].

The Effective Index Method (EIM) is one of among other methods used for modeling rectangular or channel waveguides. The EIM treats the rectangular waveguide as the superposition of two 1D waveguides: slab waveguide I confines the light in the *x* direction, while the slab waveguide II traps the light in the *y* direction.

In this method, the propagation constant of the TM_{m-1} or $TE_{n-1,}$ (according to E_{mn}^{x} or E_{mn}^{y}), mode in the planar waveguide I of thickness 2*a* is firstly calculated and used to define an effective index n_{eff}, which forms the refractive index of the second slab waveguide of thickness 2*b*. The propagation constant of the TE_{n-1} (TM_{m-1}) mode in the second planar waveguide II then represents the propagation constant of the E_{mn}^{x} (E_{mn}^{y}) mode in the channel waveguide [77], Figure III.18.

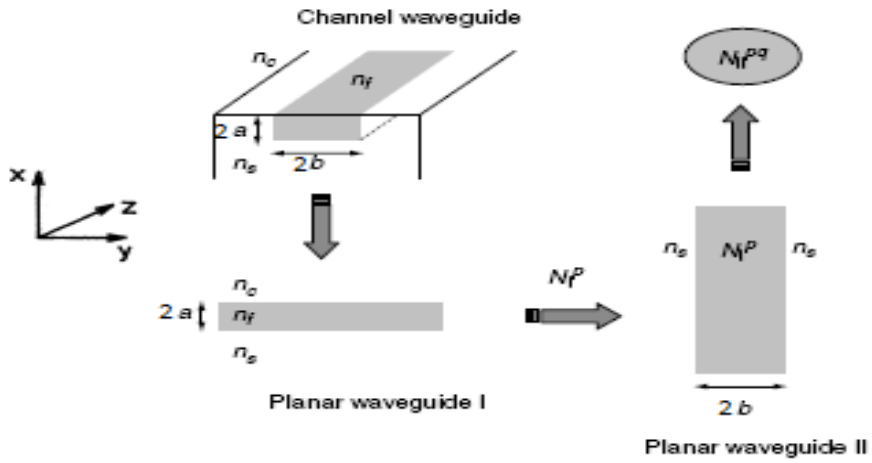

Figure III.18: Principle of the effective index method [72], with small modification.

III.3.2.1. E_{mn}^{x}Modes

For E_{mn}^{x}modes, (m and n are integers), the field components are E_x, E_y, H_y, H_z and E_z, where the major field components are E_x, H_y (H_x=0). According to the Maxwell equations, the electromagnetic field representation and the wave equation are obtained as:

$$\begin{cases} E_x = \frac{\omega\mu_0}{\beta} H_y + \frac{1}{\beta\omega n_j^2 \varepsilon_0} \frac{\partial^2 H_y}{\partial x^2} \\ E_y = \frac{1}{\beta\omega n_j^2 \varepsilon_0} \frac{\partial^2 H_y}{\partial x \partial y} \\ E_z = -\frac{i}{\omega n_j^2 \varepsilon_0} \frac{\partial H_y}{\partial x} \\ H_z = -\frac{i}{\beta} \frac{\partial H_y}{\partial y} \\ H_x = 0 \end{cases} \quad \text{(III.44)}$$

The electromagnetic field distribution is identified if the solution for H_y is known.

$$\frac{\partial^2 H_y}{\partial x^2} + \frac{\partial^2 H_y}{\partial y^2} + \left(k^2 n_j^2 - \beta^2\right) H_y = 0 \quad \text{(III.45)}$$

In the EIM, we first express the solution of the wave Eq. (III.45) for the E_{mn}^{x} mode, by using the separation of variables, as:

$$H_y(x, y) = X(x)Y(y) \quad \text{(III.46)}$$

Substituting Eq. (III.46) into Eq. (III.45) and after taking in account the estimation given by[78],which consists of assuming that the function *Y(x, y)* has a slowly variation respect to the *y* coordinate, we get the following relations:

$$\frac{\partial^2 X}{\partial x^2} + (k_0^2 n^2 - k_0^2 N_1(y)^2)X = 0 \quad \text{(III.47)}$$

$$\frac{\partial^2 Y}{\partial y^2} + (k_0^2 N_1(y)^2 - \beta^2)Y = 0 \quad \text{(III.48)}$$

A. Solution of the wave equation of E_{mn}^{x}Modes

The first step in the EIM procedure consists of solving the differential equation (III.47), using the *y* coordinate as a parameter. The Eigenvalue solution of equation (III.47) gives an effective index profile $N_1(y)$, which depends explicitly on the *y* coordinate. Once the index distribution $N_1(y)$ has been obtained, we introduce this function in the second differential equation (III.48), thus performing the second step in the problem resolution.

The solution of the equation (III.47) is similar to the solution of TM mode in an asymmetric step-index planar waveguide I, Figure III.18, given previously. The wave equations in the three regions are:

$$\begin{cases} \frac{\partial^2 X}{\partial x^2} - (k_0^2 N_1(y)^2 - k_0^2 n_s^2)X = 0; & substrate \\ \frac{\partial^2 X}{\partial x^2} - (k_0^2 N_1(y)^2 - k_0^2 n_c^2)X = 0; & cover \\ \frac{\partial^2 X}{\partial x^2} + \left(k_0^2 n_f^2 - k_0^2 N_1(y)^2\right)X = 0; & film \end{cases} \quad \text{(III.49)}$$

The solution of (III.49) is given by [79] as:

$$\mathrm{X(x)} = \begin{cases} A_1 cos(\gamma_{f1} a - \varphi) e^{-\gamma_{c1}(x-a)} & ; x > a \\ A_1 cos\left(\gamma_{f1} x - \varphi\right) & ; -a \le x \le a \\ A_1 cos(\gamma_{f1} a + \varphi) e^{\gamma_{s1}(x+a)} & ; x < -a \end{cases} \quad \text{(III.50)}$$

Where

$$\begin{cases} \gamma_{f1}^2 = k_0^2 n_f^2 - k_0^2 N_1(y)^2 \\ \gamma_{c1}^2 = k_0^2 N_1(y)^2 - k_0^2 n_c^2 \\ \gamma_{s1}^2 = k_0^2 N_1(y)^2 - k_0^2 n_s^2 \end{cases} \quad \text{(III.51)}$$

X(x) and $-\frac{i}{\omega n_j^2 \varepsilon_0}\frac{\partial \mathrm{X(x)}}{\partial x}$ are continuous at the boundaries of core–cladding interfaces x=±a. after some calculation, we get:

$$\tan\left(\gamma_{f1} a - \varphi\right) = \frac{n_f^2}{n_c^2}\frac{\gamma_{c1}}{\gamma_{f1}} \quad \text{(III.52)}$$

$$\tan\left(\gamma_{f1} a + \varphi\right) = \frac{n_f^2}{n_s^2}\frac{\gamma_{s1}}{\gamma_{f1}} \quad \text{(III.53)}$$

From these two equations we deduce the characteristic equation of the asymmetric step-index planar waveguide for TM mode is given by:

$$2k_0 a\sqrt{n_f^2 - N_1^2} = arctan\frac{n_f^2}{n_c^2}\sqrt{\frac{N_1^2-n_c^2}{n_f^2-N_1^2}} + arctan\frac{n_f^2}{n_s^2}\sqrt{\frac{N_1^2-n_s^2}{n_f^2-N_1^2}} + m\pi \quad \text{(III.54)}$$

$$2\varphi = m\pi + arctan\frac{n_f^2}{n_s^2}\sqrt{\frac{N_1^2-n_s^2}{n_f^2-N_1^2}} - arctan\frac{n_f^2}{n_c^2}\sqrt{\frac{N_1^2-n_c^2}{n_f^2-N_1^2}} \quad \text{(III.55)}$$

Where

$\beta_1 = k_0 N_1$

In the other hand, the solution of the equation (III.48) is similar to the solution of TE mode in a symmetric step-index planar waveguide II, Figure III.18.

The wave equation (III.48) in the core and the substrate regions are given by:

$$\begin{cases} \frac{\partial^2 Y}{\partial y^2} + (k_0^2 N_1(y)^2 - k_0^2 N^2)Y = 0; & \text{film} \\ \frac{\partial^2 Y}{\partial y^2} - (k_0^2 N^2 - k_0^2 n_s^2)Y = 0; & \text{substrate} \end{cases} \quad \text{(III.56)}$$

The solution of (III.59) is the solution of a symmetric step-index planar waveguide for TE mode and this is given by:

$$\mathrm{Y(y)} = \begin{cases} A_2 \cos(\gamma_f b - \eta)\, e^{-\gamma_s(y-b)} & ;\ y > b \\ A_2 \cos(\gamma_f y - \eta) & ;\ -b \le y \le b \\ A_2 \cos(\gamma_f b + \eta)\, e^{\gamma_s(y+b)} & ;\ y < -b \end{cases} \quad \text{(III.57)}$$

Where

$$\begin{cases} \gamma_f^2 = k_0^2 N_1^2 - \beta^2 \\ \gamma_s^2 = \beta^2 - k_0^2 n_s^2 \end{cases} \quad \text{(III.58)}$$

Where

$\beta = k_0 N$

Y(x) and $\frac{\partial \mathrm{Y(x)}}{\partial x}$are continuous at the boundaries of core–cladding interfaces x=±b. after some calculation, we get:

$$tan(\gamma_f b - \eta) = \frac{\gamma_s}{\gamma_f} \quad \text{(III.59)}$$

$$tan(\gamma_f b + \eta) = \frac{\gamma_s}{\gamma_f} \quad \text{(III.60)}$$

From these two the equations, we deduce the characteristic equation of the symmetric step-index planar waveguide for TE mode as:

$$2k_0 b\sqrt{N_1^2 - N^2} = 2arctan\left(\sqrt{\frac{N^2-n_s^2}{N_1^2-N^2}}\right) + m\pi \quad \text{(III.61)}$$

$$\eta = \frac{m\pi}{2} \quad \text{(III.62)}$$

B. Field distribution of E_{mn}^{x} modes in each region

The H_y components are obtained by multiplying equations (III.50) and (III.57) in each region, Figure III.19 as in [79]. The other components are obtained by replacing the derivatives$\frac{\partial H_y}{\partial x}$, $\frac{\partial H_y}{\partial y}$, $\frac{\partial^2 H_y}{\partial x^2}$ and $\frac{\partial^2 H_y}{\partial x \partial y}$ in the formula (III.44) in each region. After calculation, we get the complete field distribution of E_{mn}^{x} modes as fallow:

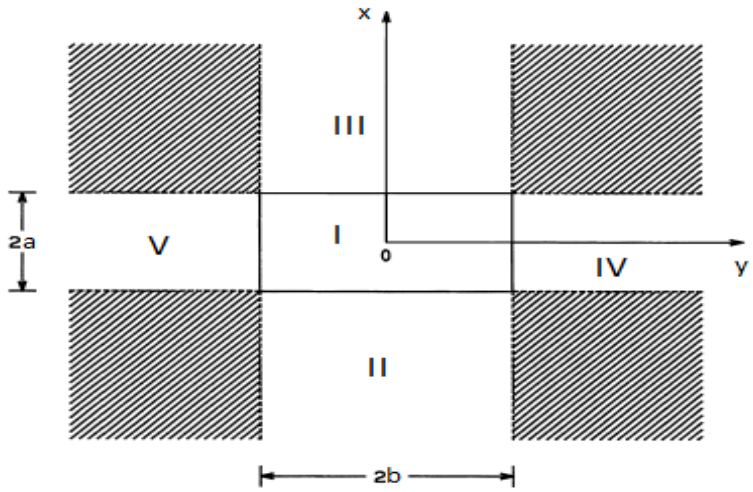

Figure III.19: Three-dimensional rectangular waveguide [79], with small modification.

Region I

$$\begin{cases} H_y = Acos(\gamma_{f1}x - \varphi)cos(\gamma_f y - \eta) \\ E_x = A\left(\frac{\omega\mu_0}{\beta} - \frac{\gamma_{f1}^2}{\beta\omega n_f^2\varepsilon_0}\right)\left(cos(\gamma_{f1}x - \varphi)cos(\gamma_f y - \eta)\right) \\ E_y = \frac{A\gamma_f\gamma_{f1}}{\beta\omega n_f^2\varepsilon_0} sin(\gamma_{f1}x - \varphi)sin(\gamma_f y - \eta) \\ E_z = \frac{Ai\gamma_{f1}}{\omega n_f^2\varepsilon_0} sin(\gamma_{f1}x - \varphi)cos(\gamma_f y - \eta) \\ H_z = \frac{Ai\gamma_f}{\beta} cos(\gamma_{f1}x - \varphi)sin(\gamma_f y - \eta) \\ H_x = 0 \end{cases} \quad \text{(III.63)}$$

Region II

$$\begin{cases} H_y = Acos(\gamma_f y - \eta)cos(\gamma_{f1} a + \varphi)e^{\gamma_{s1}(x+a)} \\ E_x = A\left(\frac{\omega\mu_0}{\beta} + \frac{\gamma_{s1}^2}{\beta\omega n_s^2 \varepsilon_0}\right) cos(\gamma_f y - \eta)cos(\gamma_{f1} a + \varphi)e^{\gamma_{s1}(x+a)} \\ E_y = \frac{-A\gamma_{s1}}{\beta\omega n_s^2 \varepsilon_0} sin(\gamma_f y - \eta)cos(\gamma_{f1} a + \varphi)e^{\gamma_{s1}(x+a)} \\ E_z = -\frac{iA\gamma_{s1}}{\omega n_s^2 \varepsilon_0} \cos(\gamma_f y - \eta) \cos(\gamma_{f1} a + \varphi)\, e^{\gamma_{s1}(x+a)} \\ H_z = \frac{iA}{\beta} sin(\gamma_f y - \eta)cos(\gamma_{f1} a + \varphi)e^{\gamma_{s1}(x+a)} \\ H_x = 0 \end{cases} \quad \text{(III.64)}$$

Region III

$$\begin{cases} H_y = Acos(\gamma_{f1} a - \varphi)cos(\gamma_f y - \eta)e^{-\gamma_{c1}(x-a)} \\ E_x = A\left(\frac{\omega\mu_0}{\beta} + \frac{\gamma_{c1}^2}{\beta\omega n_c^2 \varepsilon_0}\right) cos(\gamma_{f1} a - \varphi)cos(\gamma_f y - \eta)e^{-\gamma_{c1}(x-a)} \\ E_y = \frac{A\gamma_f\gamma_{c1}}{\beta\omega n_c^2 \varepsilon_0} cos(\gamma_{f1} a - \varphi)sin(\gamma_f y - \eta)e^{-\gamma_{c1}(x-a)} \\ E_z = \frac{Ai\gamma_{c1}}{\omega n_c^2 \varepsilon_0} cos(\gamma_{f1} a - \varphi)cos(\gamma_f y - \eta)e^{-\gamma_{c1}(x-a)} \\ H_z = \frac{iA\gamma_f}{\beta} cos(\gamma_{f1} a - \varphi)sin(\gamma_f y - \eta)e^{-\gamma_{c1}(x-a)} \\ H_x = 0 \end{cases} \quad \text{(III.65)}$$

Region IV

$$\begin{cases} H_y = Acos(\gamma_f b - \eta)cos(\gamma_{f1} x - \varphi)e^{-\gamma_s(y-b)} \\ E_x = A\left(\frac{\omega\mu_0}{\beta} - \frac{\gamma_{f1}^2}{\beta\omega n_s^2 \varepsilon_0}\right) cos(\gamma_f b - \eta)cos(\gamma_{f1} x - \varphi)e^{-\gamma_s(y-b)} \\ E_y = \frac{A\gamma_{f1}\gamma_s}{\beta\omega n_s^2 \varepsilon_0} cos(\gamma_f b - \eta)sin(\gamma_{f1} x - \varphi)e^{-\gamma_s(y-b)} \\ E_z = \frac{Ai\gamma_{f1}}{\omega n_s^2 \varepsilon_0} cos(\gamma_f b - \eta)sin(\gamma_{f1} x - \varphi)e^{-\gamma_s(y-b)} \\ H_z = \frac{i\gamma_s A}{\beta} cos(\gamma_f b - \eta)cos(\gamma_{f1} x - \varphi)e^{-\gamma_s(y-b)} \\ H_x = 0 \end{cases} \quad \text{(III.66)}$$

Region V

$$\begin{cases} H_y = Acos(\gamma_{f1} x - \varphi)cos(\gamma_f b + \eta)e^{\gamma_s(y+b)} \\ E_x = A\left(\frac{\omega\mu_0}{\beta} - \frac{\gamma_{f1}^2}{\beta\omega n_s^2 \varepsilon_0}\right) cos(\gamma_{f1} x - \varphi)cos(\gamma_f b + \eta)e^{\gamma_s(y+b)} \\ E_y = \frac{-A\gamma_s\gamma_{f1}}{\beta\omega n_s^2 \varepsilon_0} sin(\gamma_{f1} x - \varphi)cos(\gamma_f b + \eta)e^{\gamma_s(y+b)} \\ E_z = \frac{iA\gamma_{f1}}{\omega n_s^2 \varepsilon_0} sin(\gamma_{f1} x - \varphi)cos(\gamma_f b + \eta)e^{\gamma_s(y+b)} \\ H_z = -\frac{iA\gamma_s}{\beta} \cos(\gamma_{f1} x - \varphi) \cos(\gamma_f b + \eta)\, e^{\gamma_s(y+b)} \\ H_x = 0 \end{cases} \quad \text{(III.67)}$$

III.3.2.2. E_{mn}^{y}Modes

The solutions of the E_{mn}^{y}polarised modes are attained in analogous way as for E_{mn}^{x}modes carried out for quasi-TM modes. The field components are E_x, E_y, H_x, H_z and E_z, where the major field components are E_y, H_x (H_y=0). According to the Maxwell equations, the electromagnetic field representation and the wave equation are obtained as:

$$\begin{cases} E_x = -\frac{1}{\beta\omega n_j^2\varepsilon_0}\frac{\partial^2 H_x}{\partial x\partial y} \\ E_y = -\frac{\omega\mu_0}{\beta}H_x - \frac{1}{\beta\omega n_j^2\varepsilon_0}\frac{\partial^2 H_x}{\partial y^2} \\ E_z = \frac{i}{\omega n_j^2\varepsilon_0}\frac{\partial H_x}{\partial y} \\ H_z = -\frac{i}{\beta}\frac{\partial H_x}{\partial x} \\ H_y = 0 \end{cases} \quad \text{(III.68)}$$

The field's distributions can be recognized if H_x will be determined.

$$\frac{\partial^2 H_x}{\partial x^2} + \frac{\partial^2 H_x}{\partial y^2} + \left(k^2 n_j^2 - \bar{\beta}^2\right)H_x = 0 \quad \text{(III.69)}$$

The solution of this wave equation by using the separation of variables is:

$$H_x(x,y) = \bar{X}(x)\bar{Y}(y) \quad \text{(III.70)}$$

Where:

$$\frac{\partial^2 \bar{X}}{\partial x^2} + (k_0^2 n^2 - k_0^2 N_2(y)^2)\bar{X} = 0 \quad \text{(III.71)}$$

$$\frac{\partial^2 \bar{Y}}{\partial y^2} + \left(k_0^2 N_2(y)^2 - \bar{\beta}^2\right)\bar{Y} = 0 \quad \text{(III.72)}$$

A. Solution of the wave equation of E_{mn}^{y}Modes

For E_{mn}^{y} modes, if one considers the propagation in the planar waveguide I, one notices that the component of the EM field almost perpendicular to the plane of incidence is the most dominant component of the E field which is E_y. So this propagation is similar to TE mode, solution of equation (III.71). If one considers the propagation in the planar guide of the thickness 2b, one notes that the component of the EM field almost perpendicular to the plane of incidence is the most dominant component of the H field which is H_x. So this propagation is similar to the TM mode, solution of equation (III.72).

The solutions of (III.71) are done as [79]:

$$\overline{\mathrm{X}}(\mathrm{x}) = \begin{cases} B_1 cos(\gamma_{f2} a - \bar{\varphi}) e^{-\gamma_{c2}(x-a)} & ; x > a \\ B_1 cos(\gamma_{f2} x - \bar{\varphi}) & ; -a \le x \le a \\ B_1 cos(\gamma_{f2} a + \bar{\varphi}) e^{\gamma_{s2}(x+a)} & ; x < -a \end{cases} \quad \text{(III.73)}$$

Where

$$\begin{cases} \gamma_{f2}^2 = k_0^2 n_f^2 - k_0^2 N_2(y)^2 \\ \gamma_{c2}^2 = k_0^2 N_2(y)^2 - k_0^2 n_c^2 \\ \gamma_{s2}^2 = k_0^2 N_2(y)^2 - k_0^2 n_s^2 \end{cases} \quad \text{(III.74)}$$

$\overline{\mathrm{X}}(\mathrm{x})$ and $\frac{\partial \overline{\mathrm{X}}(\mathrm{x})}{\partial x}$are continuous at the boundaries of core–cladding interfaces x=±a. we get:

$$\gamma_{f2} a - \bar{\varphi} = atan\left(\frac{\gamma_{c2}}{\gamma_{f2}}\right) \quad \text{(III.75)}$$

$$\gamma_{f2} a + \bar{\varphi} = atan\left(\frac{\gamma_{s2}}{\gamma_{f2}}\right) \quad \text{(III.76)}$$

From these two the equations we deduce the characteristic equation of the asymmetric step-index planar waveguide for TE mode, as fallow:

$$2k_0 a\sqrt{n_f^2 - N_2^2} = arctan\sqrt{\frac{N_2^2 - n_c^2}{n_f^2 - N_2^2}} + arctan\sqrt{\frac{N_2^2 - n_s^2}{n_f^2 - N_2^2}} + m\pi \quad \text{(III.77)}$$

$$2\bar{\varphi} = m\pi + arctan\sqrt{\frac{N_2^2 - n_s^2}{n_f^2 - N_2^2}} - arctan\sqrt{\frac{N_2^2 - n_c^2}{n_f^2 - N_2^2}} \quad \text{(III.78)}$$

With: $\beta_2 = k_0 N_2$

The solution of (III.75) is the solution of a symmetric step-index planar waveguide for TM mode and this is given by:

$$\overline{\mathrm{Y}}(\mathrm{y}) = \begin{cases} B_2 cos(\bar{\gamma}_f b - \bar{\eta}) e^{-\bar{\gamma}_s(y-b)} & ; y > b \\ B_2 cos(\bar{\gamma}_f y - \bar{\eta}) & ; -b \le y \le b \\ B_2 cos(\bar{\gamma}_f b + \bar{\eta}) e^{\bar{\gamma}_s(y+b)} & ; y < -b \end{cases} \quad \text{(III.79)}$$

Where

$$\begin{cases} \bar{\gamma}_f^2 = k_0^2 N_2^2 - \bar{\beta}^2 \\ \bar{\gamma}_s^2 = \bar{\beta}^2 - k_0^2 n_s^2 \end{cases} \quad \text{(III.80)}$$

Where

$\bar{\beta} = k_0 \overline{N}$

$\overline{Y}(x)$; $\frac{i}{\omega n_f^2 \varepsilon_0}\frac{\partial \overline{Y}(x)}{\partial x}$ are continuous at the boundaries of core–cladding interfaces x=±b. We get the following equations:

$$\bar{\gamma}_f b - \bar{\eta} = atan\left(\frac{N_2^2}{n_s^2}\frac{\bar{\gamma}_s}{\bar{\gamma}_f}\right) \tag{III.81}$$

$$\bar{\gamma}_f b + \bar{\eta} = atan\left(\frac{N_2^2}{n_s^2}\frac{\bar{\gamma}_s}{\bar{\gamma}_f}\right) \tag{III.82}$$

From these two equations, we deduce the characteristic equation of the symmetric step-index planar waveguide for TM mode as fallow:

$$2k_0 b\sqrt{N_2^2 - \bar{N}^2} = 2arctan\left(\frac{N_2^2}{n_s^2}\sqrt{\frac{\bar{N}^2 - n_s^2}{N_2^2 - \bar{N}^2}}\right) + m\pi \tag{III.83}$$

$$\bar{\eta} = \frac{m\pi}{2} \tag{III.84}$$

B. Field distribution of E_{mn}^{y} modes in each region

We deduce H_x components by multiplying (III.73) and (III.79) equations in each region. The other components are obtained by calculating the derivatives $\frac{\partial H_x}{\partial x}$, $\frac{\partial H_x}{\partial y}$, $\frac{\partial^2 H_x}{\partial y^2}$ and $\frac{\partial^2 H_x}{\partial x \partial y}$ in the formula (III.68) in each region. After manipulation, we get the complete field distribution of E_{mn}^{y} modes as fallow:

Region I

$$\begin{cases} H_x = B cos(\gamma_{f2} x - \bar{\varphi}) \cos(\bar{\gamma}_f y - \bar{\eta}) \\ E_x = -\frac{1}{\beta \omega n_f^2 \varepsilon_0}\bar{\gamma}_f \gamma_{f2} B sin(\gamma_{f2} x - \bar{\varphi}) \sin(\bar{\gamma}_f y - \bar{\eta}) \\ E_y = B\left(\frac{\bar{\gamma}_f^2}{\beta \omega n_f^2 \varepsilon_0} - \frac{\omega \mu_0}{\beta}\right) cos(\gamma_{f2} x - \bar{\varphi}) cos(\bar{\gamma}_f y - \bar{\eta}) \\ E_z = \frac{-i\bar{\gamma}_f B}{\omega n_f^2 \varepsilon_0} \cos(\gamma_{f2} x - \bar{\varphi}) \sin(\bar{\gamma}_f y - \bar{\eta}) \\ H_z = \frac{i\gamma_{f2} B}{\beta} \sin(\gamma_{f2} x - \bar{\varphi}) \cos(\bar{\gamma}_f y - \bar{\eta}) \\ H_y = 0 \end{cases} \tag{III.85}$$

Region II

$$\begin{cases} H_x = B cos\left(\bar{\gamma}_f y - \bar{\eta}\right) \cos\left(\gamma_{f2} a + \bar{\varphi}\right) e^{\gamma_{s2}(x+a)} \\ E_x = \frac{\bar{\gamma}_f \gamma_{s2} B}{\beta \omega n_s^2 \varepsilon_0} \sin\left(\bar{\gamma}_f y - \bar{\eta}\right) \cos\left(\gamma_{f2} a + \bar{\varphi}\right) e^{\gamma_{s2}(x+a)} \\ E_y = B \left(\frac{\bar{\gamma}_f^2}{\beta \omega n_s^2 \varepsilon_0} - \frac{\omega \mu_0}{\beta}\right) \cos\left(\bar{\gamma}_f y - \bar{\eta}\right) \cos\left(\gamma_{f2} a + \bar{\varphi}\right) e^{\gamma_{s2}(x+a)} \\ E_z = \frac{-i\bar{\gamma}_f B}{\omega n_s^2 \varepsilon_0} \sin\left(\bar{\gamma}_f y - \bar{\eta}\right) \cos\left(\gamma_{f2} a + \bar{\varphi}\right) e^{\gamma_{s2}(x+a)} \\ H_z = -\frac{i\gamma_{s2} B}{\beta} \cos\left(\bar{\gamma}_f y - \bar{\eta}\right) \cos\left(\gamma_{f2} a + \bar{\varphi}\right) e^{\gamma_{s2}(x+a)} \\ H_y = 0 \end{cases} \quad \text{(III.86)}$$

Region III

$$\begin{cases} H_x = B cos\left(\gamma_{f2} a - \bar{\varphi}\right) \cos\left(\bar{\gamma}_f y - \bar{\eta}\right) e^{-\gamma_{c2}(x-a)} \\ E_x = -\frac{\gamma_{c2} \bar{\gamma}_f B}{\beta \omega n_c^2 \varepsilon_0} \cos\left(\gamma_{f2} a - \bar{\varphi}\right) \sin\left(\bar{\gamma}_f y - \bar{\eta}\right) e^{-\gamma_{c2}(x-a)} \\ E_y = B \left(\frac{\bar{\gamma}_f^2}{\beta \omega n_c^2 \varepsilon_0} - \frac{\omega \mu_0}{\beta}\right) \cos\left(\gamma_{f2} a - \bar{\varphi}\right) \cos\left(\bar{\gamma}_f y - \bar{\eta}\right) e^{-\gamma_{c2}(x-a)} \\ E_z = \frac{-i\bar{\gamma}_f B}{\omega n_c^2 \varepsilon_0} \cos\left(\gamma_{f2} a - \bar{\varphi}\right) \sin\left(\bar{\gamma}_f y - \bar{\eta}\right) e^{-\gamma_{c2}(x-a)} \\ H_z = \frac{i\gamma_{c2} B}{\beta} \cos\left(\gamma_{f2} a - \bar{\varphi}\right) \cos\left(\bar{\gamma}_f y - \bar{\eta}\right) e^{-\gamma_{c2}(x-a)} \\ H_y = 0 \end{cases} \quad \text{(III.87)}$$

Region IV

$$\begin{cases} H_x = B cos\left(\gamma_{f2} x - \bar{\varphi}\right) \cos\left(\bar{\gamma}_f b - \bar{\eta}\right) e^{-\bar{\gamma}_s(y-b)} \\ E_x = -\frac{\bar{\gamma}_s \gamma_{f2} B}{\beta \omega n_s^2 \varepsilon_0} \sin\left(\gamma_{f2} x - \bar{\varphi}\right) \cos\left(\bar{\gamma}_f b - \bar{\eta}\right) e^{-\bar{\gamma}_s(y-b)} \\ E_y = -B \left(\frac{\bar{\gamma}_s^2}{\beta \omega n_s^2 \varepsilon_0} + \frac{\omega \mu_0}{\beta}\right) \cos\left(\gamma_{f2} x - \bar{\varphi}\right) \cos\left(\bar{\gamma}_f b - \bar{\eta}\right) e^{-\bar{\gamma}_s(y-b)} \\ E_z = \frac{-i\bar{\gamma}_s B}{\omega n_s^2 \varepsilon_0} \cos\left(\gamma_{f2} x - \bar{\varphi}\right) \cos\left(\bar{\gamma}_f b - \bar{\eta}\right) e^{-\bar{\gamma}_s(y-b)} \\ H_z = \frac{i\gamma_{f2} B}{\beta} \sin\left(\gamma_{f2} x - \bar{\varphi}\right) \cos\left(\bar{\gamma}_f b - \bar{\eta}\right) e^{-\bar{\gamma}_s(y-b)} \\ H_y = 0 \end{cases} \quad \text{(III.88)}$$

Region V

$$\begin{cases} H_x = B cos\left(\gamma_{f2} x - \bar{\varphi}\right) \cos\left(\bar{\gamma}_f b + \bar{\eta}\right) e^{\bar{\gamma}_s(y+b)} \\ E_x = \frac{\bar{\gamma}_s \gamma_{f2} B}{\beta \omega n_s^2 \varepsilon_0} \sin\left(\gamma_{f2} x - \bar{\varphi}\right) \cos\left(\bar{\gamma}_f b + \bar{\eta}\right) e^{\bar{\gamma}_s(y+b)} \\ E_y = -B \left(\frac{\omega \mu_0}{\beta} + \frac{\bar{\gamma}_s^2}{\beta \omega n_s^2 \varepsilon_0}\right) \cos\left(\gamma_{f2} x - \bar{\varphi}\right) \cos\left(\bar{\gamma}_f b + \bar{\eta}\right) e^{\bar{\gamma}_s(y+b)} \\ E_z = \frac{i\bar{\gamma}_s B}{\omega n_s^2 \varepsilon_0} \cos\left(\gamma_{f2} x - \bar{\varphi}\right) \cos\left(\bar{\gamma}_f b + \bar{\eta}\right) e^{\bar{\gamma}_s(y+b)} \\ H_z = \frac{i\gamma_{f2} B}{\beta} \sin\left(\gamma_{f2} x - \bar{\varphi}\right) \cos\left(\bar{\gamma}_f b + \bar{\eta}\right) e^{\bar{\gamma}_s(y+b)} \\ H_y = 0 \end{cases} \quad \text{(III.89)}$$

III.4. Conclusion

In this chapter, we have modeled slab and channel photonic waveguides. Firstly, isotropic and anisotropic slab waveguides were studied with the optical ray method and the electromagnetic method, respectively. The former approach allowed us to calculate the dispersion equations of the TE and TM guided modes function of the propagation angles and the effective indices of the guided modes. Whereas, the electromagnetic approach, permitted us to calculate the wave equations, their solutions and the characteristic equations, as well as, the solutions of electromagnetic field in the three regions of the waveguide, where each region was fabricated by a uniaxial anisotropic crystal. We have developed a program in Matlab, based on the bisection method, which allowed us to calculate the propagation constants of both TE and TM polarizations, as a function of the frequency, of the wavelength and the thickness of the waveguiding film. The developed program also allowed us to see the influence of the physical and geometrical parameters as well as the source's wavelength on the guided modes. The results showed that, the increase in the thickness of the core makes increasing the propagation constants of the modes as well as reducing their cut-off frequencies, especially for of higher order modes. Further, the increase in the source's wavelength motivates the decrease of the propagation constants of modes and an increase of their cut-off thicknesses, especially for higher orders modes. Furthermore, changes of cover and substrate refractive indices have slight influence on the propagating modes. However, small changes in the core refractive index engender considerable changes in the propagation constants and cut-off frequencies of the guided modes.

Finally, the effective index method (EIM) is explained in detail and used to calculate dispersion equations of $E_{mn}^{y}$and E_{mn}^{x} modes as well as their field distribution in each region of the Embedded-strip waveguide.

CHAPTER IV:

BIREFRINGENT PLANAR WAVEGUIDE BASED SENSOR

IV.1. Introduction

Due to the exponential decay of the evanescent field in photonic waveguides based sensors, only changes occurring in close proximity to the surface will be sensed. This feature makes photonic waveguides based sensors attractive for chemical and biochemical sensing, with reduced sample volumes and consequently reduced auxiliary reagent volumes as well. Evanescent-wave biosensors enable monitoring of biomolecular interactions in real-time and can contribute to a more concrete disease diagnosis. With these types of sensors, it would be possible to, selectively, sense an almost limitless range of analytes just by selecting the appropriate biological receptor. Currently, plasmonic and silicon photonics based biosensors are among the most employed evanescent-wave biosensors for the analyses of nucleic acids with potential applicability in clinical diagnosis [80]. In addition to that, many integrated optical sensors are fabricated by $LiNbO_3$ thin film crystals because of its many useful properties [81]. Especially its birefringence that permits coupled both TE and TM modes in its optical slab waveguide [82], the latter property can be used to detect two different chemical substances in the same time by using the same configuration, where TE mode can sense an analyte, while the TM mode can identify the other analyte. Sensitivity is the most important parameter of an optical sensor. Therefore, sensitivity enhancement of integrated sensors has involved significant attention [83].

In this chapter, we have investigated sensitivity and evanescent field of a slab waveguide optical sensor constituted of Lithium Niobate as a guiding film, where the influence of the source, geometrical and physical parameters, as well as the electric-field induced birefringence, on the sensitivity and on the evanescent field are studied. In this case, we can predict that the sensitivity of the sensor can be adjusted by varying the applied electric field.

IV.2.Modeling of the birefringent slab waveguide based sensor

IV.2.1. Characteristic equations calculation

The permittivity tensors of the three regions of the slab waveguide illustrated in Figure IV.1, are the following$\bar{\bar{\varepsilon}}_f$,$\bar{\bar{\varepsilon}}_c$ and$\bar{\bar{\varepsilon}}_s$, respectively for the core, the cover and the substrate, where

$$\bar{\bar{\varepsilon}}_i = \begin{bmatrix} \varepsilon_i & 0 & 0 \\ 0 & \varepsilon_i & 0 \\ 0 & 0 & \varepsilon_{iz} \end{bmatrix} = \varepsilon_0 \begin{bmatrix} n_i^2 & 0 & 0 \\ 0 & n_i^2 & 0 \\ 0 & 0 & n_{iz}^2 \end{bmatrix}$$

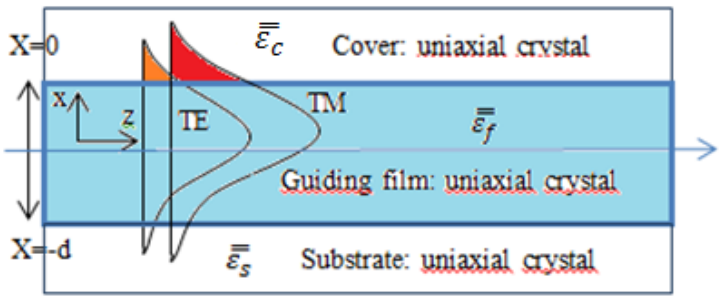

Figure IV.1: Birefringent slab waveguide based sensor.

In such birefringent planar waveguide, both TE and TM modes propagated simultaneously in the waveguide [84]. The dispersion relations are calculated in the previous chapter as follows:

$$k_0 d\sqrt{n_f^2 - N^2} = arctan\left(\sqrt{\frac{N^2-n_s^2}{n_f^2-N^2}}\right) + arctan\left(\sqrt{\frac{N^2-n_c^2}{n_f^2-N^2}}\right) + m\pi \qquad \text{(IV.1)}$$

For TE modes

$$k_0 d\frac{n_{fz}}{n_f}\sqrt{n_f^2 - N^2} = arctan\frac{n_{fz}n_f}{n_{cz}n_c}\sqrt{\frac{N^2-n_c^2}{n_f^2-N^2}} + arctan\frac{n_{fz}n_f}{n_{sz}n_s}\sqrt{\frac{N^2-n_s^2}{n_f^2-N^2}} + m\pi \qquad \text{(IV.2)}$$

For TM modes

All the parameters are defined in the chapter three.

IV.2.2. Sensitivity of birefringent slab waveguide based sensor

Sensitivity is the change of the sensor output signal in response to unit change in a property of the sensor (the concentration of an analyte deposited on the sensor surface). It is a parameter that defines the ability of a sensor to transduce an input signal to an output one. The sensitivity is function of the substance to be detected and the kind of the waveguide transducer. The sensitivity is deduced from the expression: $S = \left(\frac{\partial n_p}{\partial N}\right)^{-1}$ .By differentiating the characteristics equations (IV.5) and (IV.6) with the last consideration and the standardization as in [85], we get:

$$S_{TE} = \sqrt{\frac{1-a_c}{1-X}}\frac{X}{a_c}\frac{1}{\sqrt{a_c-X}}\frac{1}{\left[T+\frac{1}{\sqrt{a_s-X}}+\frac{1}{\sqrt{a_c-X}}\right]} \qquad \text{(IV.3)}$$

For TE modes

$$S_{TM} = \frac{\frac{X(1-2X+a_C)\sqrt{1-a_C}}{\sqrt{1-X}\sqrt{a_C-X}[a_C(1-X(1-Xa_{CZ}))-Xa_{CZ}]}}{\left[T'K+\frac{a_C(1-a_C)}{\sqrt{(a_C-X)[a_C(1-X(1-Xa_{CZ}))-Xa_{CZ}]}}+K\sqrt{\frac{1-a_{SZ}}{1-a_S}}\frac{a_S(1-a_S)}{\sqrt{(a_S-X)[a_S(1-X(1-Xa_{SZ}))-Xa_{SZ}]}}\right]} \quad \text{(IV.4)}$$

For TM modes

$$T = k_0 d = \frac{arctan\sqrt{\frac{a_S-X}{X}}+arctan\sqrt{\frac{a_C-X}{X}}+m\pi}{\sqrt{X}} \quad \text{(IV.5)}$$

$$T' = k_0 d n_{fz} = \frac{arctan\frac{1}{\sqrt{1-a_C}\sqrt{1-a_{CZ}}}\sqrt{\frac{a_C-X}{X}}+arctan\frac{1}{\sqrt{1-a_S}\sqrt{1-a_{SZ}}}\sqrt{\frac{a_S-X}{X}}+m\pi}{\sqrt{X}} \quad \text{(IV.6)}$$

$$a_s = 1-\frac{n_s^2}{n_f^2} \quad \text{(IV.7)}$$

$$a_c = 1-\frac{n_c^2}{n_f^2} \quad \text{(IV.8)}$$

$$X = 1-\frac{N^2}{n_f^2} \quad \text{(IV.9)}$$

$$a_{sz} = 1-\frac{n_{sz}^2}{n_{fz}^2} \quad \text{(IV.10)}$$

$$a_{cz} = 1-\frac{n_c^2}{n_{fz}^2} \quad \text{(IV.11)}$$

$$K = \frac{n_{fz}}{n_f} \quad \text{(IV.12)}$$

IV.2.3. Influence of waveguide and source parameters on the sensor's sensitivity and evanescent fields

As we have seen previously, sensitivities expressions and evanescent field components are functions of the waveguide and the light source parameters. We developed a program in Matlab that allowed us to calculate the sensitivities of both TE and TM modes as a function of the frequency, of the wavelength and the thickness of the waveguiding film. The program simulates also, the electric and magnetic fields components in each region of the waveguide. The developed program allowed us to see the influence of physical, geometrical and the source parameters on the sensitivities of both TE and TM modes as well as their influence on the evanescent fields in the cover of waveguide. The slab waveguide consists essentially of a core of $LiNbO_3$ on a glass substrate; the wavelength of the source is 650 nm.

Figure IV.2 shows the sensitivity variation of both TE and TM modes, for an asymmetrical slab waveguide based sensor as a function of frequency. The core of the

waveguide sensor is $LiNbO_3$ (n_{fx}=2.2880, n_{fz}=2.2030), the refractive index of the substrate is n_s=1.80, whereas, the cover refractive index is n_c=1.628. We note that the sensitivities of the TM modes are more important than those of the TE modes. Further, sensitivities of fundamental modes (TM_0 and TE_0) are greater than those of higher order modes. Furthermore, maximum sensitivities of all modes are situated near the cut off frequencies, where those of higher order modes are situated in higher frequencies, in comparison with those of fundamental modes. We note also that, maximum sensitivities of TE modes are located in lower frequencies, in comparison with maximum sensitivities of TM modes. In the other hand**,** for a symmetrical slab waveguide sensor, we note that maximum sensitivities of TE and TM modes are equals and they are situated in the cut off frequencies, however, sensitivities decrease quickly in higher frequencies, especially for TE modes, Figure IV.3. A comparison of sensitivities of fundamental modes, for both symmetrical and asymmetrical slab waveguide sensors is represented in Figure IV.4. It is clear that sensitivities of symmetrical slab waveguide sensor are more important than those of asymmetrical slab waveguide sensor. Furthermore, for TM_0 mode, the sensitivity is maximal for a wide band of frequency, in comparison with maximum sensitivities of TE_0 mode.

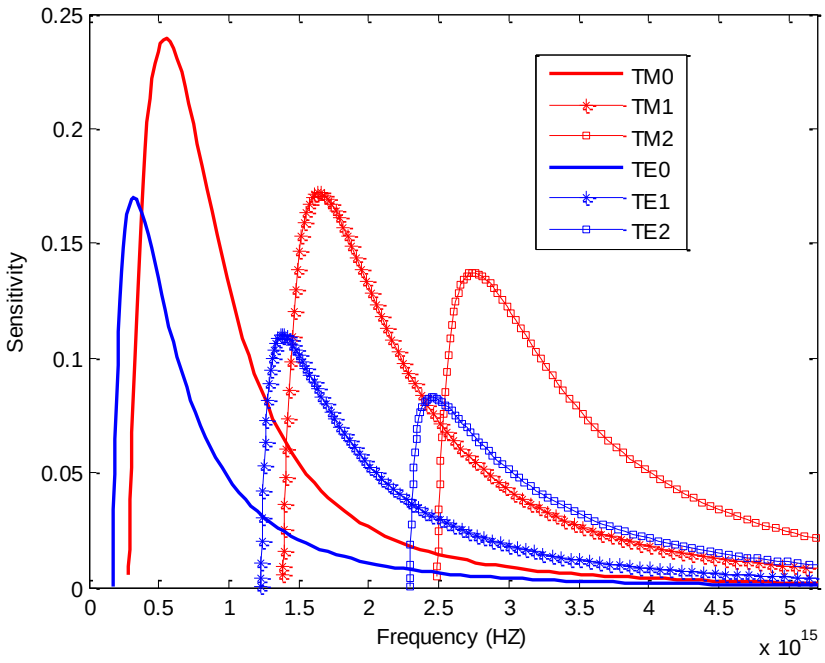

Figure IV.2: Sensitivities according to the frequency for the first three modes of an asymmetric slab waveguide (n_c=1.628, n_s=1.80, d=100 nm and $LiNbO_3$as guiding film).

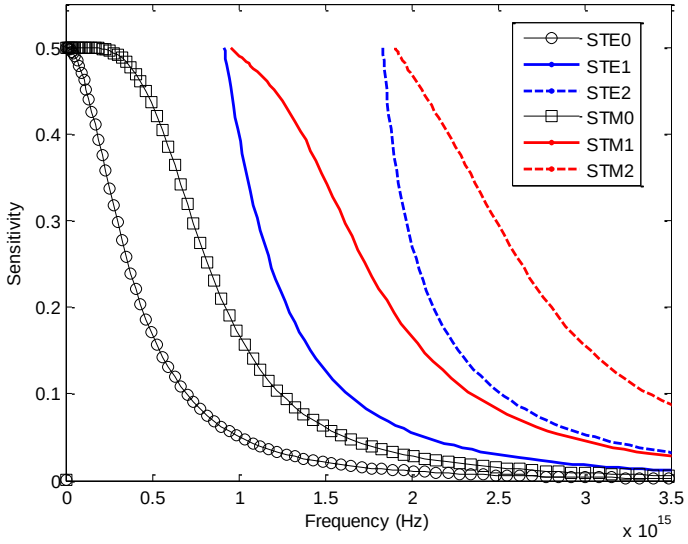

Figure IV.3: Sensitivities according to the frequency of TE_0 and TM_0 modes of a symmetric slab waveguide (n_c=n_s=1.60, d=100 nm and $LiNbO_3$as guiding film.

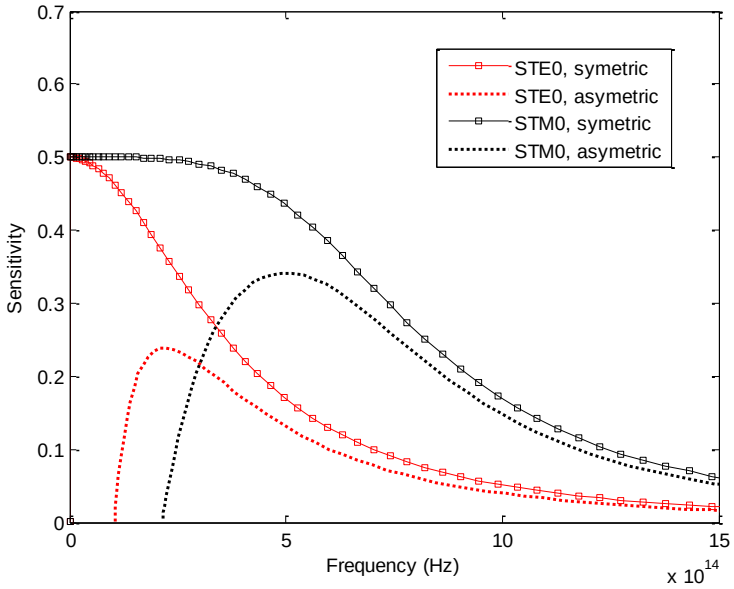

Figure IV.4: Sensitivities comparison as a function of the frequency for TE_0 and TM_0 modes of a symmetric and asymmetric slab waveguide (n_c=n_s=1.60, d=100 nm and $LiNbO_3$as guiding film).

In Figure IV.5 and IV.6 we represent electric and magnetic fields components in the cover region for both transversal polarizations. For TE mode, H_z and H_x components are very small in comparison with E_y. However, for TM mode, the dominant components are E_x and E_z, the component H_y is unimportant. For this reason, small components are not represented in the next figures. We note that the amplitudes of evanescent field components of TM modes are more

important than those of TE modes, for this reason, sensitivities of TM modes are always greater than those of TE modes. The expressions of electric and magnetic fields components are presented in the previous chapter. The intensities of these evanescent fields are responsible of sensing biochemical substances in optical slab waveguide sensors. We report that all previous remarks are valid for the all rest of figures.

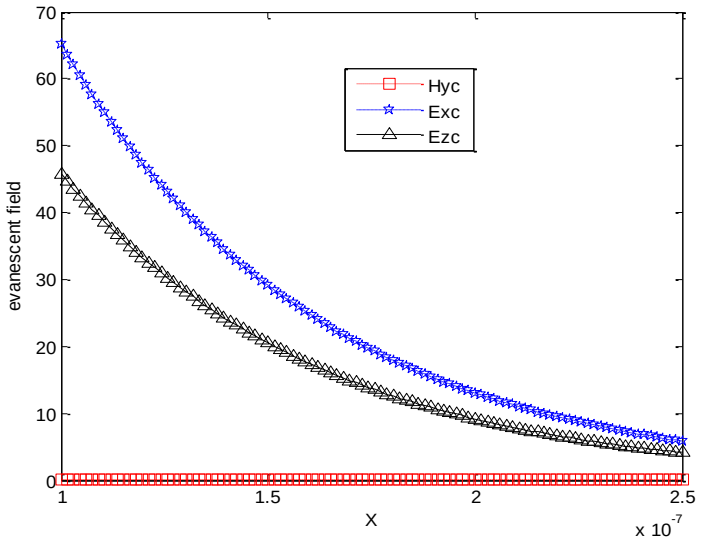

Figure IV.5: Evanescent field components in the cover versus x for TM_0 mode, (n_s=1.80, n_p=1.628, $LiNbO_3$as guiding film, d=100 nm). H_y is very small in comparison with E_z and E_x.

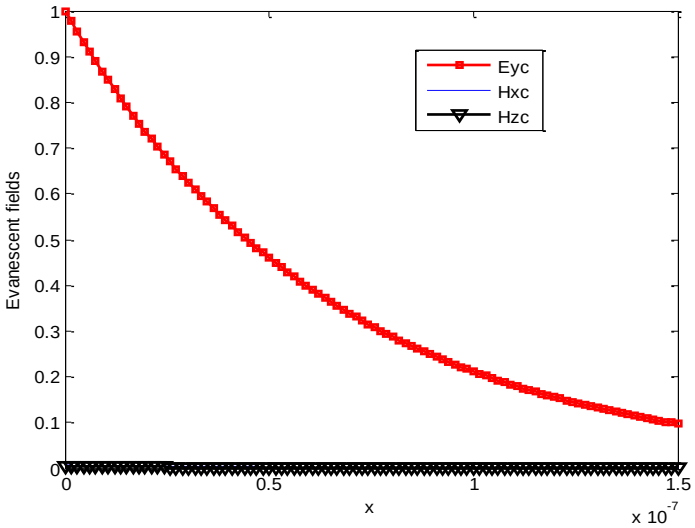

Figure IV.6: Evanescent field components in the cover versus x for TE_0 mode, (n_s=1.80, n_p=1.628, $LiNbO_3$as guiding film, d=100 nm). H_z and H_x are very small in comparison with E_y.

IV.2.3.1. Influence of the source's parameters

A. Influence of field amplitude

The expression of the sensitivity as a function of evanescent field intensity can be defined as in [85]:

$$S = \Gamma_c \left[\sqrt{\frac{1-a_c}{1-X}} + 2\mathrm{P} \left(\sqrt{\frac{1-X}{1-a_c}} - \sqrt{\frac{1-a_c}{1-X}} \right) \right] \quad \text{(IV.13)}$$

Where P=0 for TE polarization. However, P=1 for TM polarization and the confinement factor in the cover Γ_c is given by [18], as follow:

$$\Gamma_c = \frac{\iint_c |E(x,y)|^2 dxdy}{\iint_\infty |E(x,y)|^2 dxdy} \quad \text{(IV.14)}$$

Knowing that, the intensities of the electric and magnetic evanescent fields are function of their amplitudes.

Figures IV.7 and IV.8 illustrate, respectively, the sensitivity according to the frequency of fundamental modes for different fraction of modal power located in the cover. The two graphs show that, the sensitivity increase when the fraction of modal power confined in the cover increase. However, for TE_0, the sensitivity is maximal for the lower frequencies and it decreases for the higher frequencies. Whereas, for TM_0, the sensitivity is minimal for the lower frequencies and it is maximal for the higher frequencies. The increase of the sensitivities by increasing the modal power located in the cover can be explained by the increasing of evanescent field amplitudes in such region, as it is illustrated in Figures IV.9 and IV.10. Where the values of x, (at z = 0), extend from [0 to 3* d /2], for TE_0 mode, and from [0 to 5* d /2], for TM_0 mode.

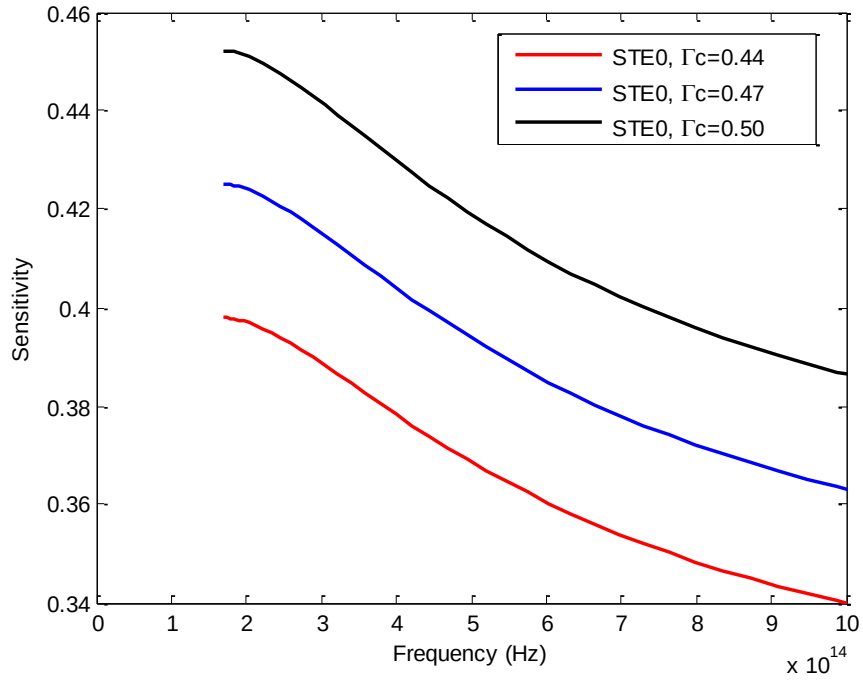

Figure IV.7: Sensitivity according to the frequency of TE_0 modes for different fraction of modal power located in the cover layer, (n_s=1.80, n_p=1.628, d=100 nm, $LiNbO_3$ as guiding film).

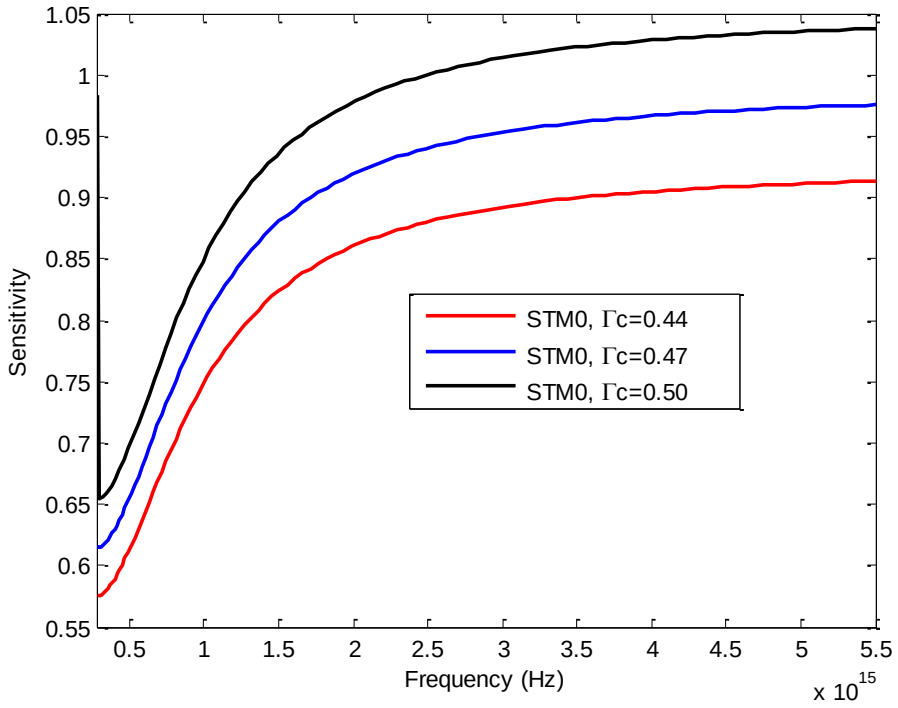

Figure IV.8: Sensitivity according to the frequency of TM_0 modes for different fraction of modal power located in the cover layer, (n_s=1.80, n_p=1.628, d=100 nm, $LiNbO_3$ as guiding film).

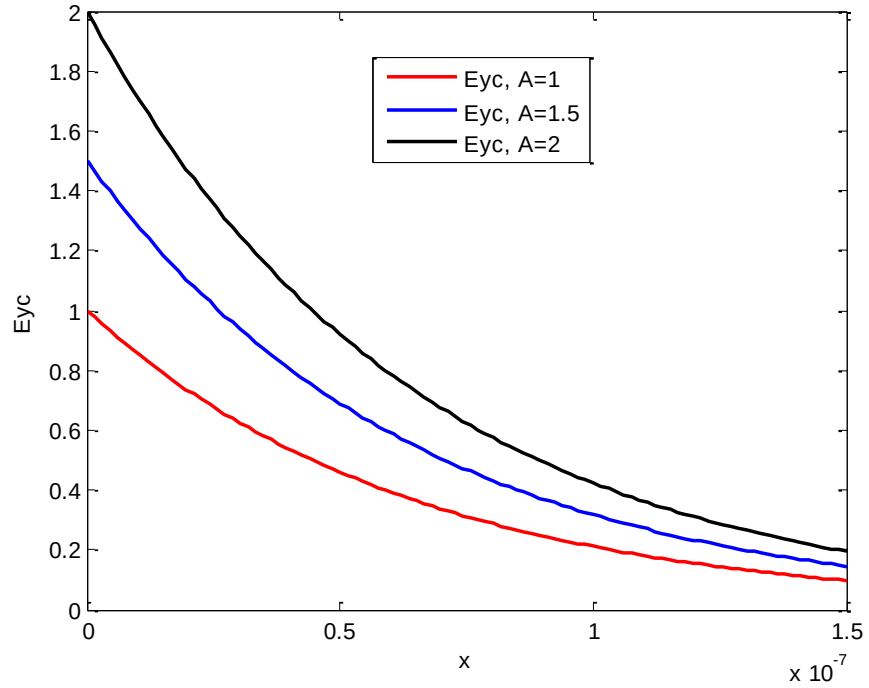

Figure IV.9: Evanescent field component E_{yc} in the cover versus x of TE_0 mode for different amplitude of field, (n_s=1.80, n_p=1.628, d=100 nm, $LiNbO_3$ as guiding film).

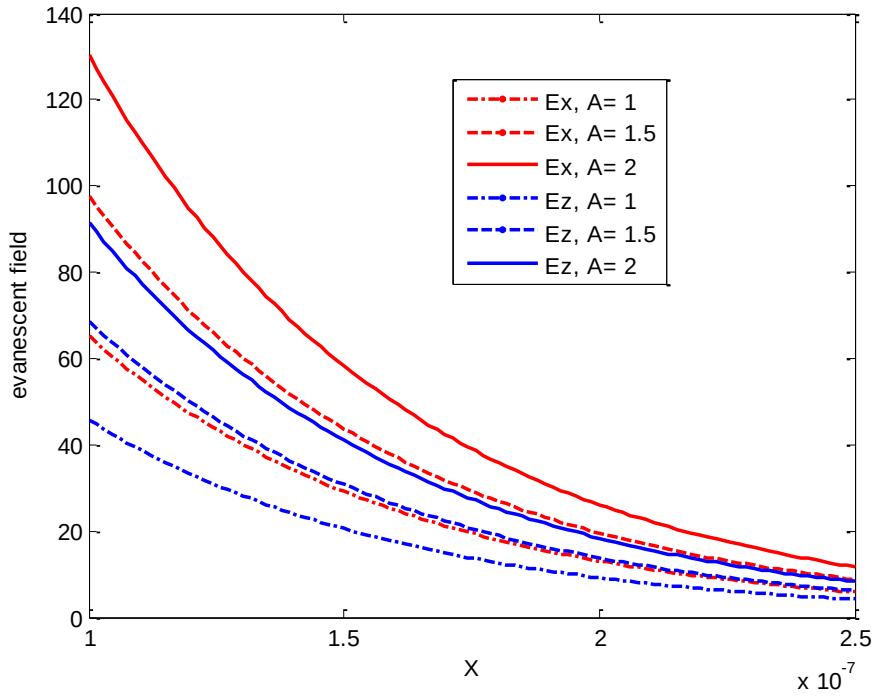

Figure IV.10: Evanescent field components (E_x, E_z) in the cover versus x of TM_0 mode for different amplitude of field, (n_s=1.80, n_p=1.628, d=100 nm, $LiNbO_3$ as guiding film).

B. Influence of the source's wavelength

Sensitivity as a function of the core thicknesses, for TE_0 and TM_0 modes, are represented in Figure IV.11 and IV.12, respectively, for different source's wavelengths. For TE_0 mode, maximal sensitivities are 0.175, 0.185 and 0.195, corresponding to 0.05, 0.07 and 0.19 µm core thicknesses, successively. However, for TM_0 mode, maximal sensitivities are 0.23, 0.25 and 0.28, corresponding to 0.1, 0.14 and 0.32 µm, core thicknesses, successively. The curves show that, the sensitivity of the planar waveguide sensor increases by increasing the source's wavelength, however, the curves shift towards higher core thicknesses. This implies that, for longer source's wavelength, maximal sensitivity is obtainable for longer core thicknesses, and vice versa. The increase of the sensitivity for longer source's wavelength can be explicated, also, by the increase of the evanescent fields intensities produced by increasing of their source's wavelength, thing that improving the light-matter interaction, as illustrated in Figures IV.13 and IV.14. Where the values of x, (at z = 0), range from [0 to 7* d /2].

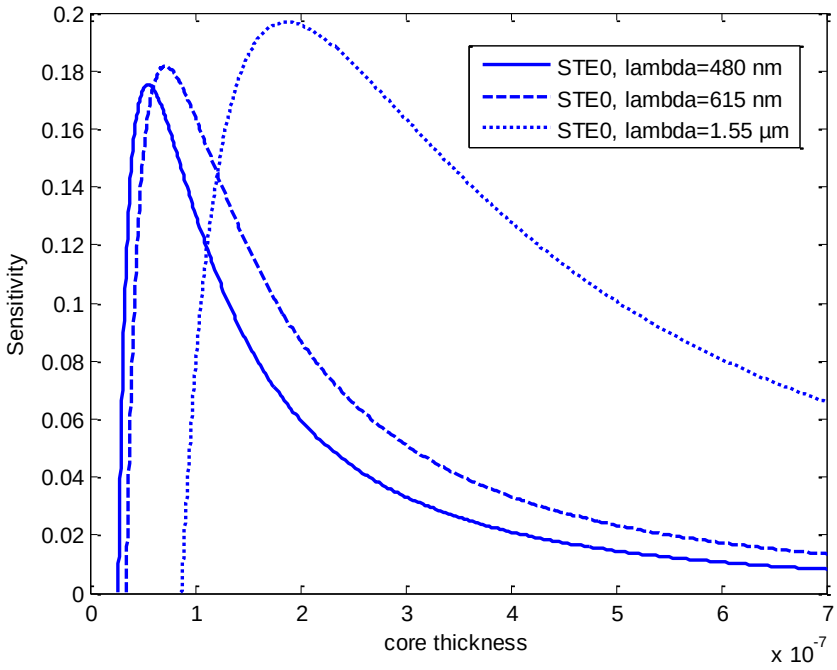

Figure IV.11: Sensitivity according to the core thicknesses of TE_0 modes for different source's wavelength, (n_s=1.80, n_p=1.628, d=100 nm, $LiNbO_3$as guiding film).

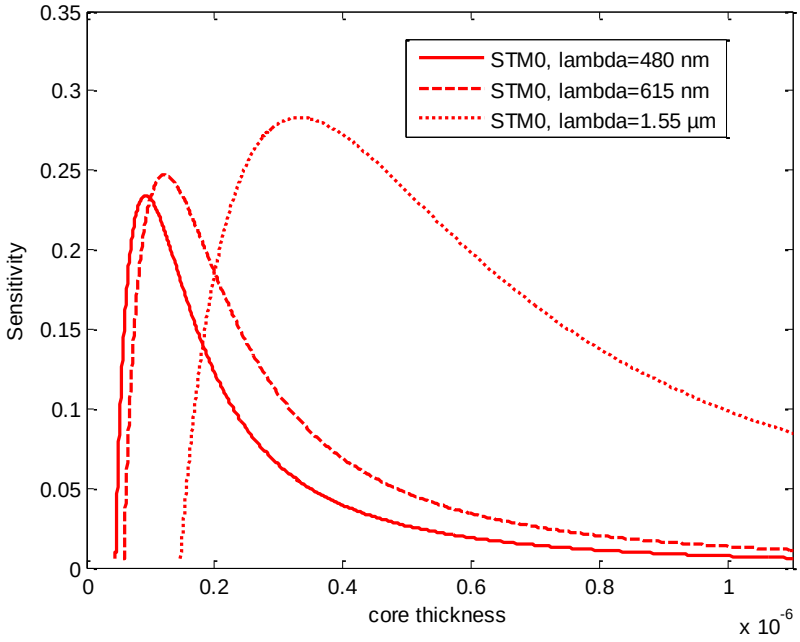

Figure IV.12: Sensitivity according to the core thicknesses ofTM_0modesfor different source's wavelength, (n_s=1.80, n_p=1.628, d=100 nm, $LiNbO_3$as guiding film).

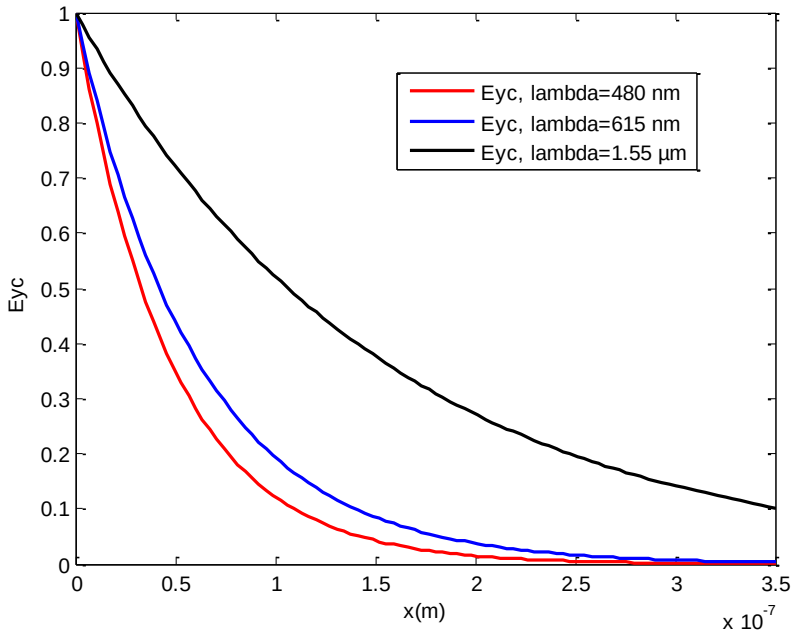

Figure IV.13: Evanescent field components E_{yc} in the cover versus x of TE_0 mode for different source's wavelengths, (n_s=1.80, n_p=1.628, d=100 nm, $LiNbO_3$as guiding film).

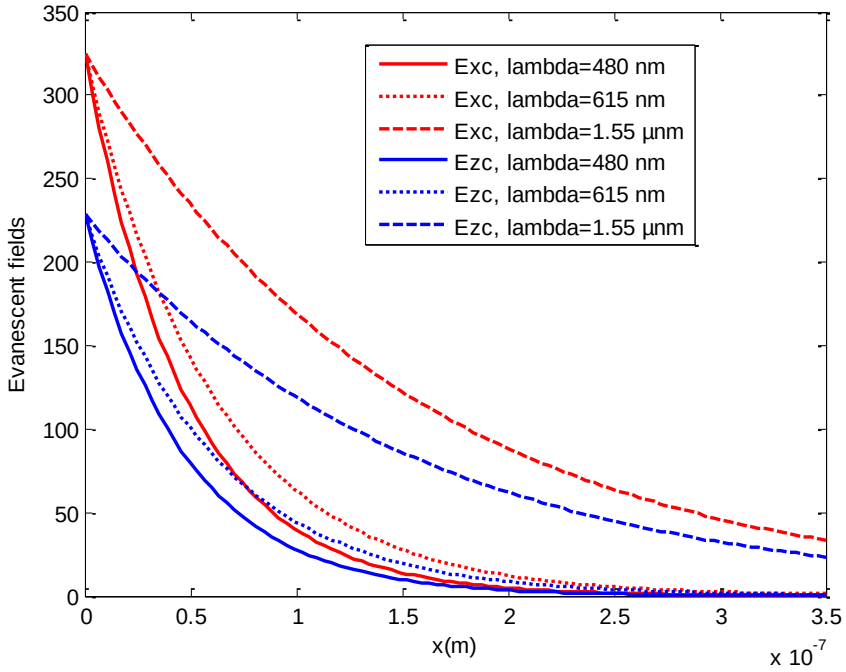

Figure IV.14: Evanescent field components (E_x, E_z) in the cover versus x of TM_0 mode for different source's wavelengths, (n_s=1.80, n_p=1.628, d=100 nm, $LiNbO_3$as guiding film).

IV.2.3.2. Influence of the geometrical parameter

Figures IV.15 and IV.16 illustrate, respectively, the sensitivities according to the frequency for TE_0 and TM_0 modes for different core thicknesses. We observe that, maximal sensitivities of TE modes are situated in the near infrared band of the electromagnetic spectrum (1.8 E14 Hz – 4.0E14 Hz). However, maximal sensitivities of TM modes are located in the visible band (3.0 E14 Hz – 7.0 E14 Hz). On the other hand, the figures show that, by increasing the core thickness, the sensitivity of the waveguide sensor decreases and the curves shift towards the lower frequencies. The decrease of the sensitivity can be explained, also, by the decrease of the fraction of modal power located in the cover, which is the area limited by the evanescent fields, the normal to the waveguide at z=0 and the super surface of the waveguide (x=0). In fact, when increasing the core thickness, great part of optical signal enter in the core of the waveguide in the form of propagating energy and hence, the evanescent field intensities decrease, as illustrated in Figures IV.17 and IV.18.

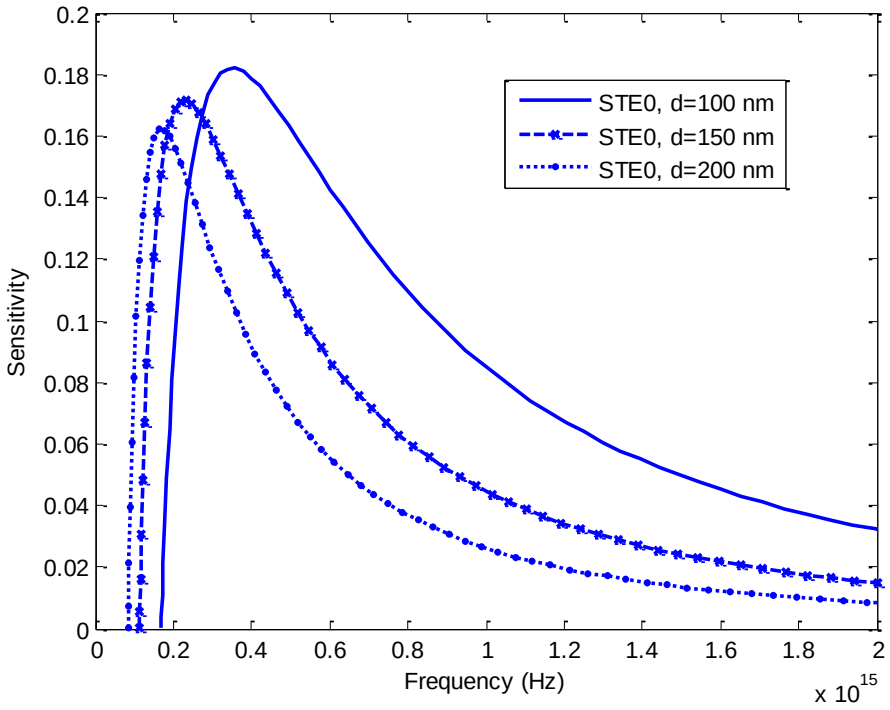

Figure IV.15: Sensitivity according to the frequency for TE_0modesfor different core thicknesses, (n_s=1.80, n_p=1.628, $LiNbO_3$as guiding film).

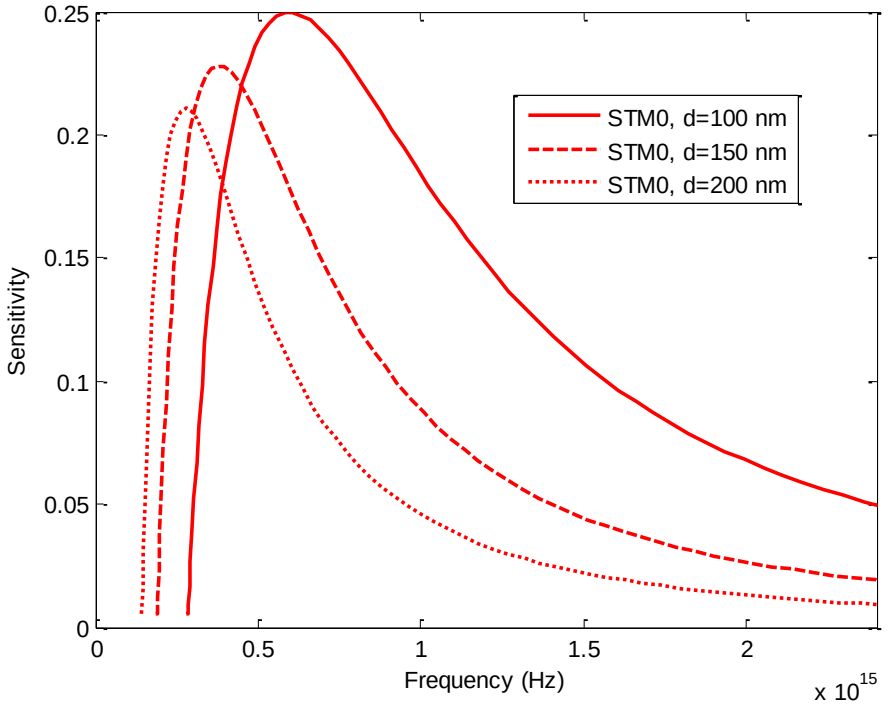

Figure IV.16: Sensitivity according to the frequency for TM_0 modes for different core thicknesses, (n_s=1.80, n_p=1.628, $LiNbO_3$as guiding film).

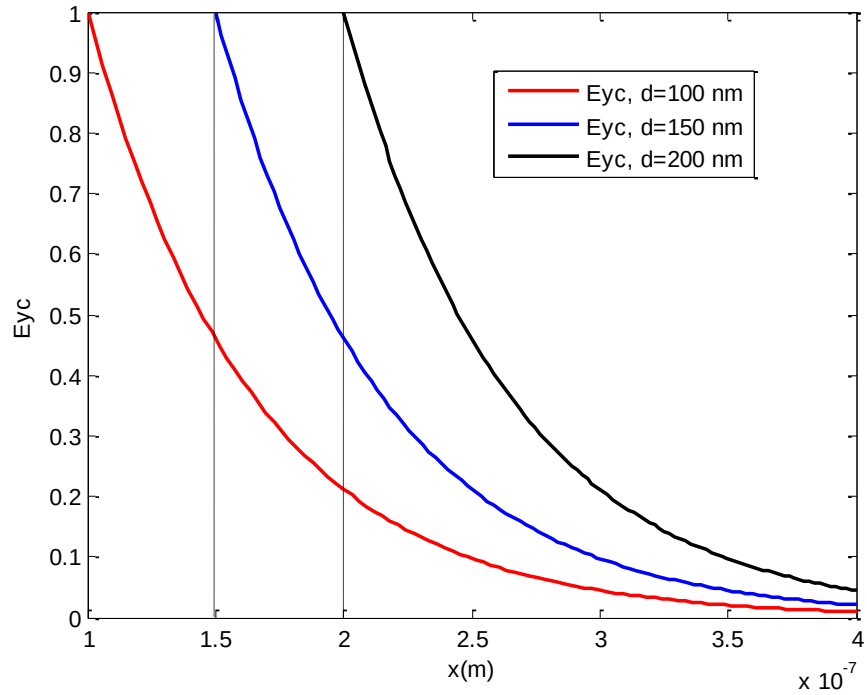

Figure IV.17: Evanescent field component E_{yc} in the cover versus x of TE_0 mode for different core thicknesses, (n_c=1.628, ns =1.80, $LiNbO_3$as guiding film).

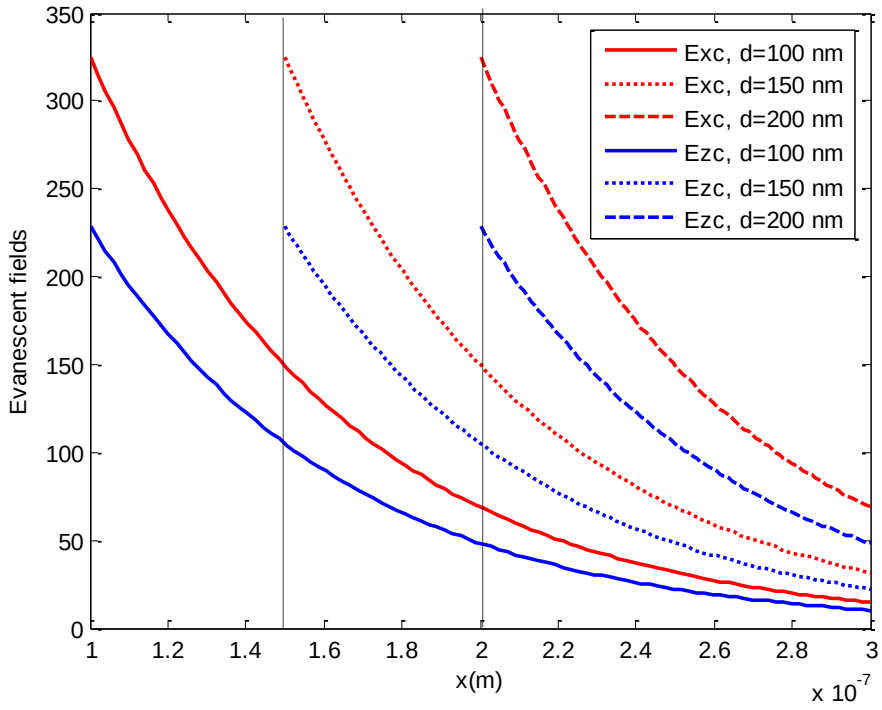

Figure IV.18: Evanescent field components in the cover versus x of TM_0 mode for different core thicknesses, (n_c=1.628, ns =1.80, $LiNbO_3$as guiding film).

IV.2.3.3. Influence of the physical parameters

Physical parameters are refractive indices of the cover, the substrate and the core of the waveguide.

A. Influence of the cover refractive index

Sensitivities according to the frequency are represented in Figures IV.19 and IV.20, for TE, TM modes, respectively, for different cover refractive index. Whereas, Figure IV.21 and IV.22, illustrate the sensitivities of fundamental modes as a function of the effective refractive index, for different cover refractive index. The graphs give us the values of maximal sensitivities and their corresponding frequencies as well as their corresponding effective refractive index. Hence, maximal sensitivities, corresponding to 1.48 and 1.70 cover refractive index are, successively, 0.11; 0.225, For TE_0 and 0.175; 0.29, for TM_0. Whereas, their corresponding frequencies are, respectively, 3.0E14 Hz; 2.25E14 Hz, For TE_0 and 6.E14 Hz; 5.45E14 Hz, for TM_0. However maximal sensitivities of both fundamental modes are located at1.85 effective refractive index. The curves show that, the sensitivity of the slab waveguide sensor improves by increasing the cover refractive index for both TE and TM modes. In addition to that, the position of the maximal sensitivities exhibit small shifts toward lower values. As the cover refractive index must be always less than substrate refractive index, we can conclude that, for both TE, TM modes, the sensitivity of the detector progresses by make the cover refractive index closer to that of the substrate. Therefore, changes of the cover refractive index, induces changes in the value of maximum sensitivity and changes in their corresponding frequencies.

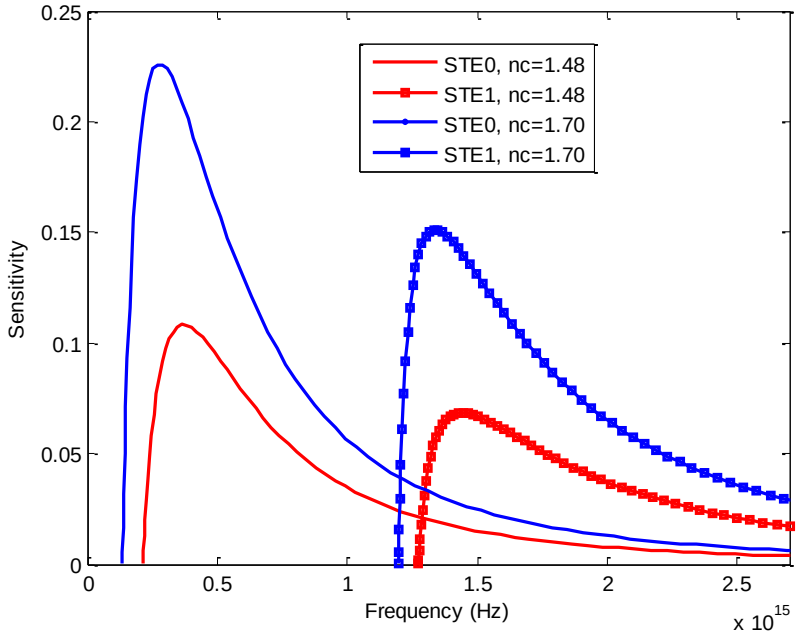

Figure IV.19: Sensitivity according to the frequency for TE modes for diverse refractive index of the cover n_c, lines curves for TE_0 modes and square markers linked lines curves for TE_1 modes, (n_s=1.80, d=100 nm, $LiNbO_3$as guiding film).

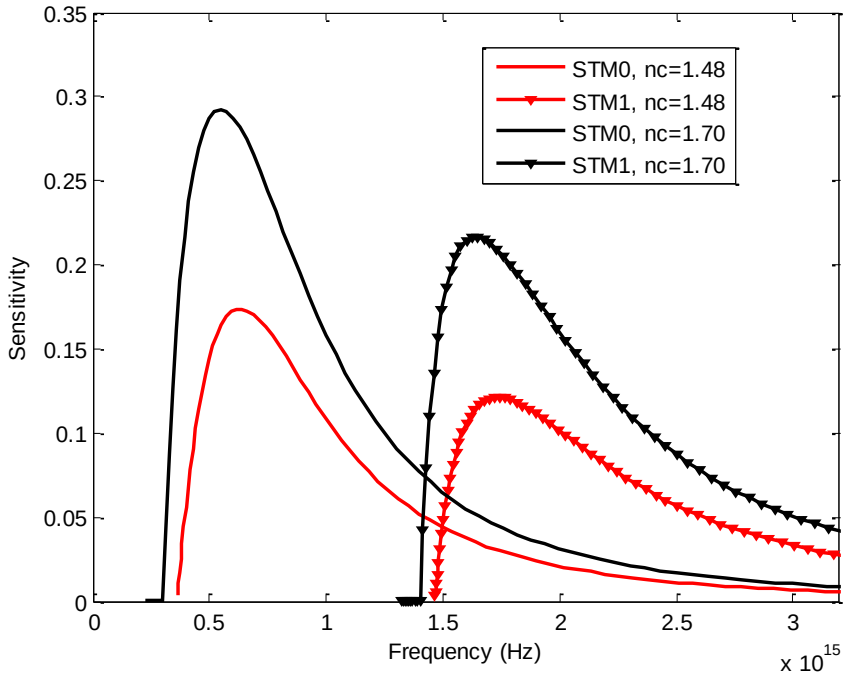

Figure IV.20: Sensitivity according to the frequency for TM modes for diverse refractive index of the cover n_c, lines curves for TM_0 modes and square markers linked lines curves for TM_1 modes, (n_s=1.80, d=100 nm, $LiNbO_3$as guiding film).

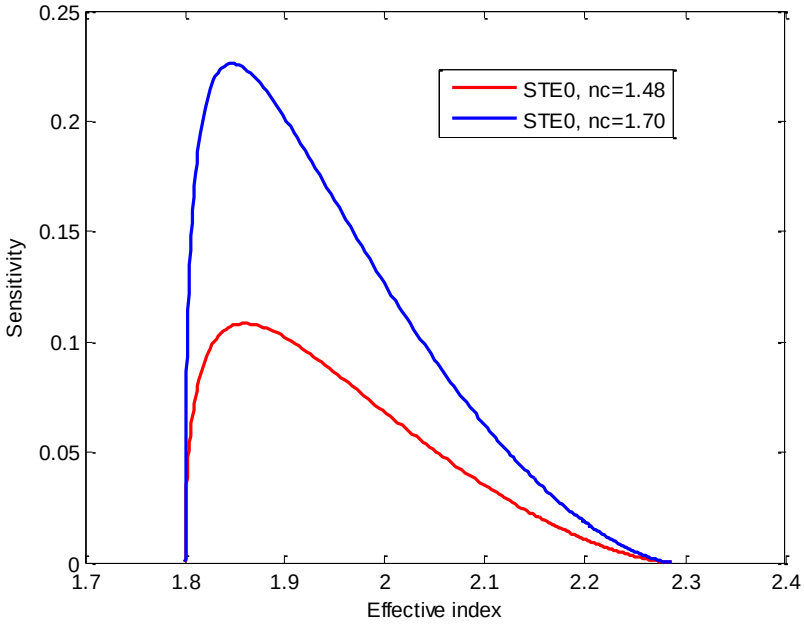

Figure IV.21: Sensitivity according to the effective index for TE_0 modes for diverse refractive index of the cover n_c, (n_s=1.80, d=100 nm, $LiNbO_3$as guiding film).

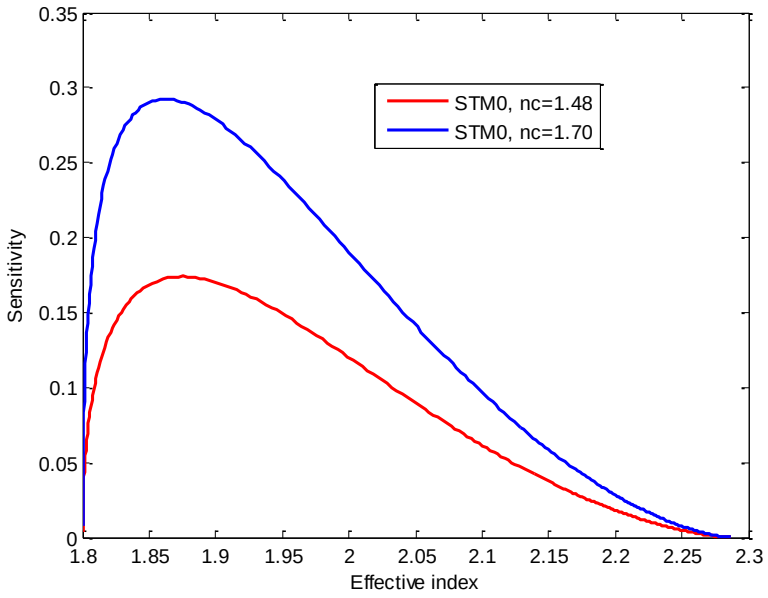

Figure IV.22: Sensitivity according to the effective index for TM_0 mode for dissimilar refractive index of the cover n_c, (n_s=1.80, d=100 nm, $LiNbO_3$as guiding film).

Figures IV.23, IV.24 represent evanescent field components of TE_0 and TM_0 modes, respectively, for different cover refractive indices. The curves show small changes of the evanescent field components, near to the cut off frequencies. These changes are caused by small changes of the effective refractive indices of both fundamental modes induced by changes of

cover refractive index, Figure IV.25. These small changes of the evanescent field components in the cover, near to the cut off frequencies, have neglected influence on the sensitivity of the slab waveguide sensor.

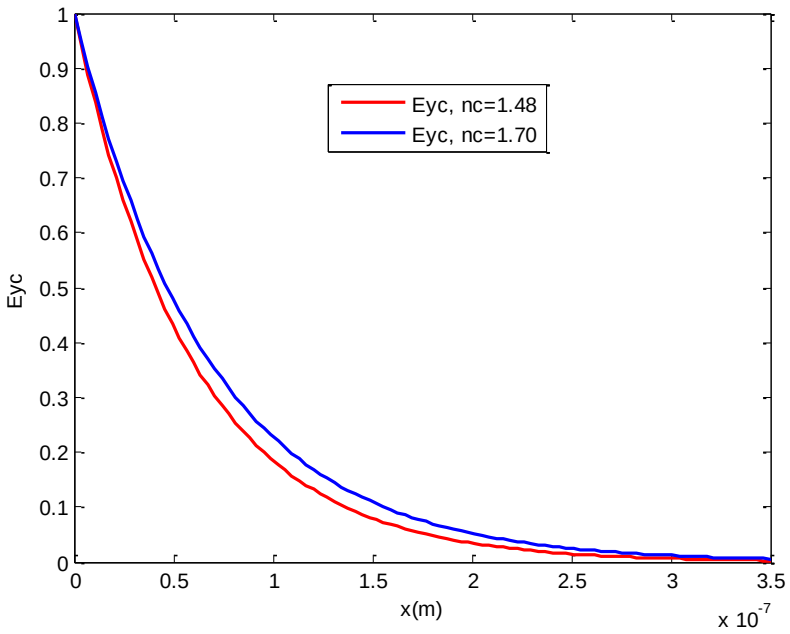

Figure IV.23: Evanescent field components E_{yc} in the cover versus x of TE_0 mode for different cover refractive indices, (n_s=1.80, d=100 nm, $LiNbO_3$as guiding film).

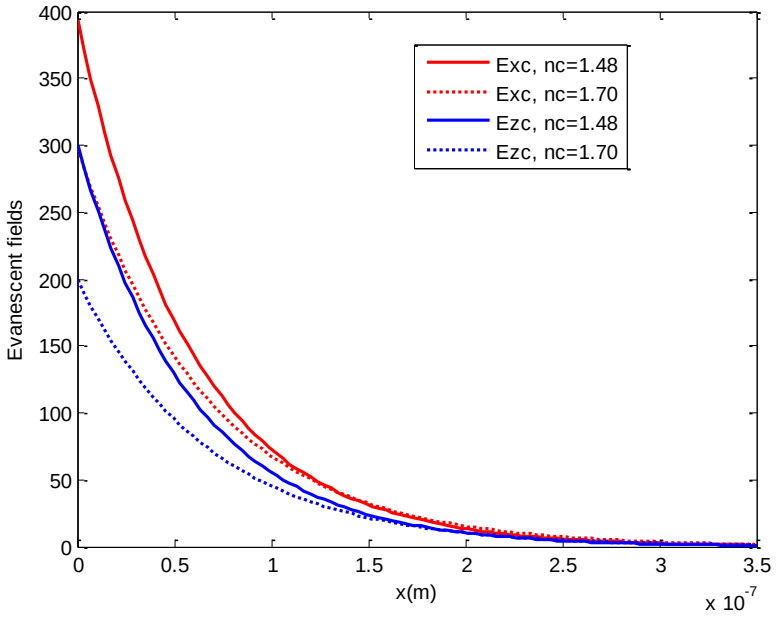

Figure IV.24: Evanescent field components (E_{xc}, E_{zc}) in the cover versus x of TM_0 mode for different cover refractive indices, (n_c=1.48, d=100 nm, $LiNbO_3$as guiding film).

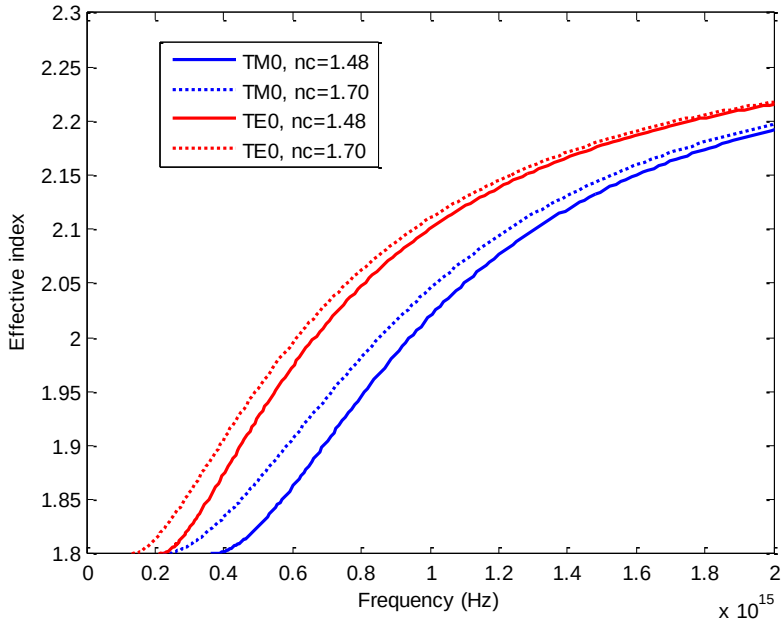

Figure IV.25: Effective index versus frequency of TE_0 and TM_0 modes in slab waveguide for different cover indices, (n_s=1.80, d=100 nm, $LiNbO_3$as guiding film).

B. Influence of the substrate refractive index

For different substrate refractive index, we illustrate in Figure IV.26 and IV.27, respectively, sensitivities according to the frequency of TE and TM modes. However, we represent, in Figure IV.28 and IV.29, sensitivities of both fundamental modes, according to the effective refractive index, for different substrate refractive index. As in the case of the cover refractive index changes, the first two graphs give us the values of maximal sensitivities and their corresponding frequencies, however, the last two graphs give us the values of maximal sensitivities and their corresponding effective refractive index. For TE_0, maximal sensitivities, corresponding to, 1.60 and 1.80 substrate refractive index, are 0.245; 0.11 and their corresponding frequencies are 2.E14 Hz; 3.E14 Hz; whereas their corresponding effective refractive indices are 1.65 and 1.85 successively. However, for TM_0, maximal sensitivities, corresponding to, 1.60 and 1.80 substrate refractive index, are 0.34; 0.175, respectively; while their corresponding frequencies are 5.E14 Hz and 6.E14 Hz; whereas their corresponding effective refractive indices are 1.7 and 1.86 successively. The curves show that, the sensitivity of the planar waveguide sensor decreases by increasing the substrate refractive index for both TE and TM modes. Further, the position of the maximal sensitivities exhibit shifts toward higher values of frequency, Figures IV.26, IV.27, and considerable shifts toward higher values of effective refractive indices, Figure IV.28, IV.29. We can conclude that, changes of substrate

refractive index, induces changes in the value of maximum sensitivity and changes in its position.

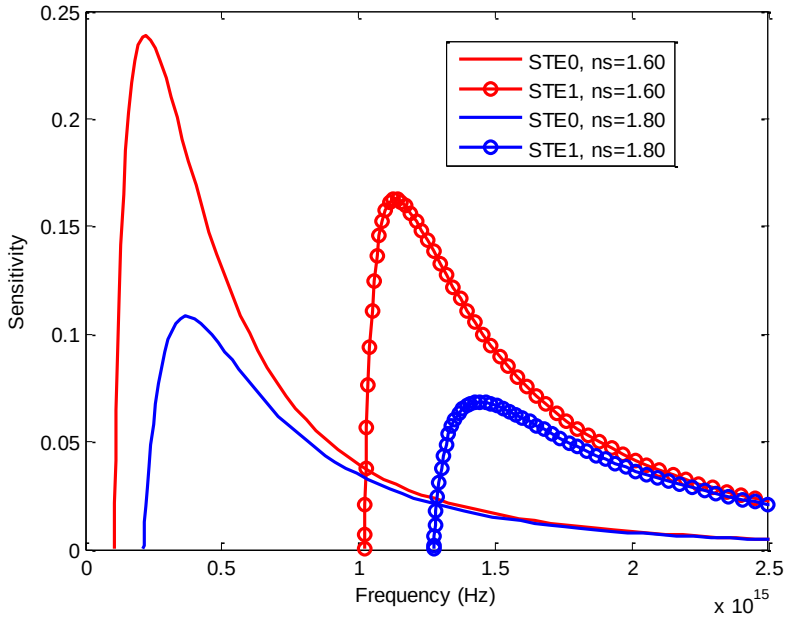

Figure IV.26: Sensitivity according to the frequency for TE modes for dissimilar refractive index of the substrate n_s, lines curves for TE_0 modes and circle markers linked lines curves for TE_1 modes, (n_c=1.48, d=100 nm, $LiNbO_3$as guiding film).

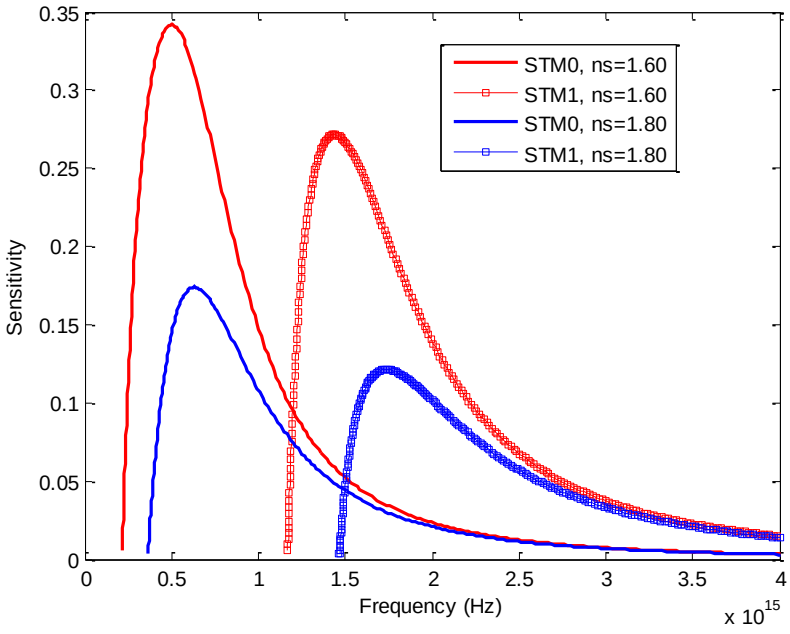

Figure IV.27: Sensitivity according to the frequency for TM modes for diverse substrate refractive index n_s, lines curves for TM_0 modes and circle markers linked lines curves for TM_1 modes, (n_c=1.48, d=100 nm, $LiNbO_3$as guiding film).

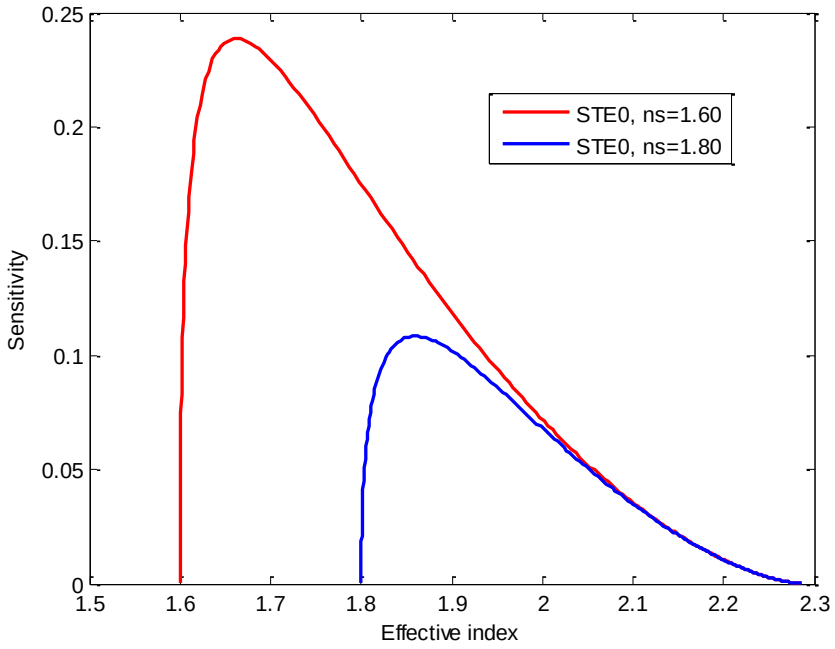

Figure IV.28: Sensitivity according to the effective index for TE_0 mode for diverse refractive index of the substrate n_s, (n_c=1.48, d=100 nm, $LiNbO_3$as guiding film).

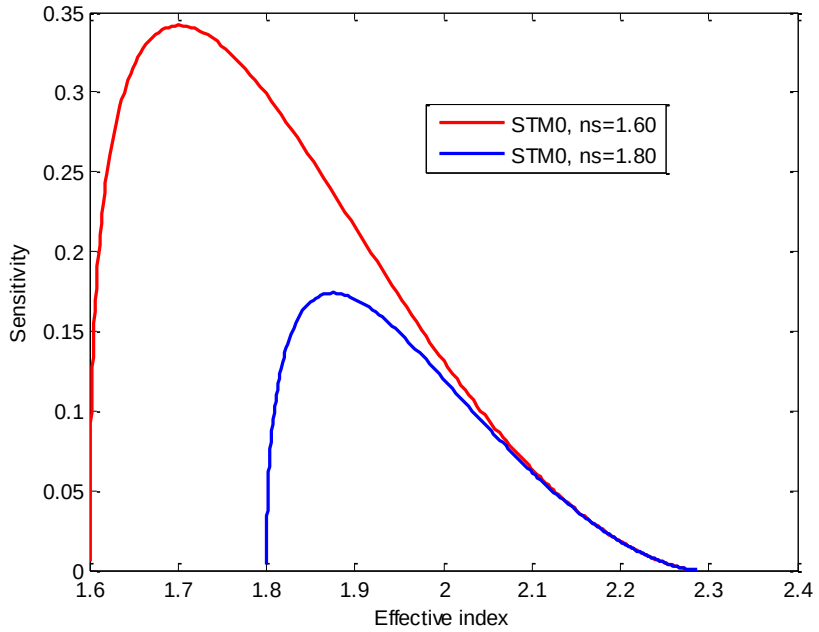

Figure IV.29: Sensitivity according to the effective index for TM_0 mode for dissimilar refractive index of the substrate n_s, (n_c=1.48, d=100 nm, $LiNbO_3$as guiding film).

Figure IV.30 and IV.31 represent evanescent field components in the cover of TE_0 and TM_0 modes, for different substrate refractive indices, respectively. The curves show small changes in the evanescent field components caused by changes of substrate refractive index; in

addition, these small changes occur near the cut off frequencies of each mode. Whereas, far from these latter, there are no changes of evanescent field components at all. The same thing for evanescent field components in the substrate, Figure IV.32 and IV.33. There are small increases of E_{ys} and small decreases of E_{xs}, E_{zs} in the substrate resulting from increasing substrate refractive index. These small changes of the evanescent field components in the cover and in the substrate, near to the cut off frequencies, are caused by small changes of the effective refractive indices resulting from substrate refractive index changes, Figure IV.34. Thus, changes of the evanescent field components have neglected influence on the sensitivity of the slab waveguide sensor, where there are important changes caused by changes of substrate refractive index, as we have seen in Figures IV.28 and IV.29.

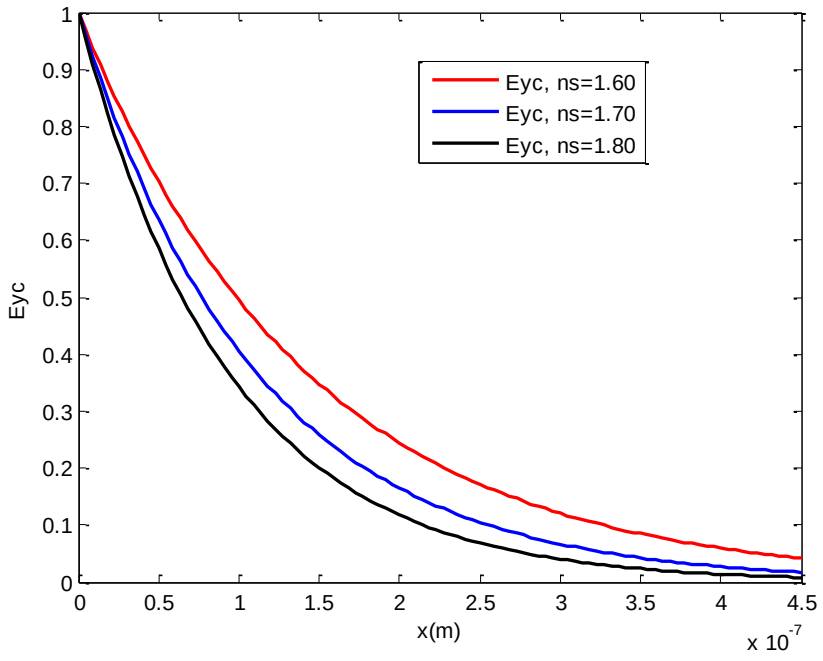

Figure IV.30: Evanescent field components E_{yc} in the cover versus x of TE_0 mode for different substrate refractive indices, (n_c=1.48, d=100 nm, $LiNbO_3$ as guiding film).

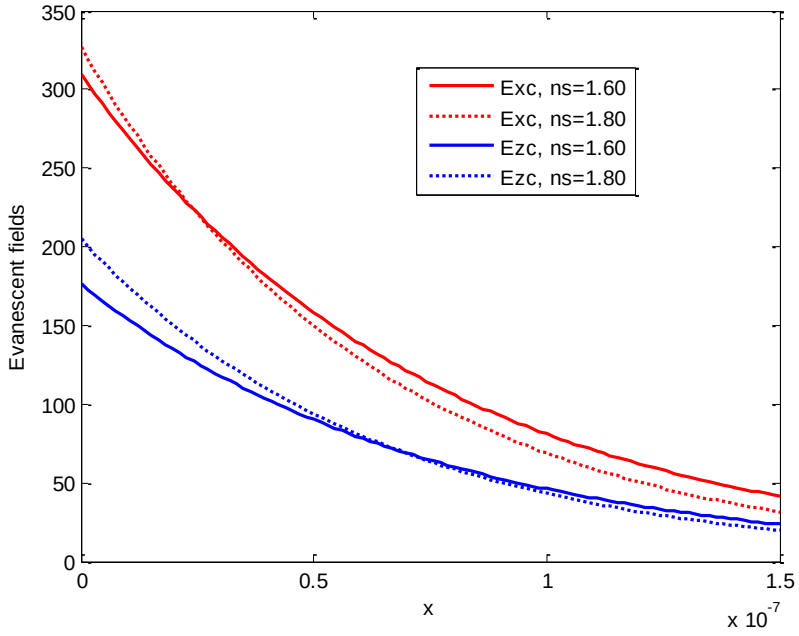

Figure IV.31: Evanescent field components (Ex, Ez) in the cover versus x of TM_0 mode for different substrate refractive indices, (n_c=1.48, d=100 nm, $LiNbO_3$as guiding film).

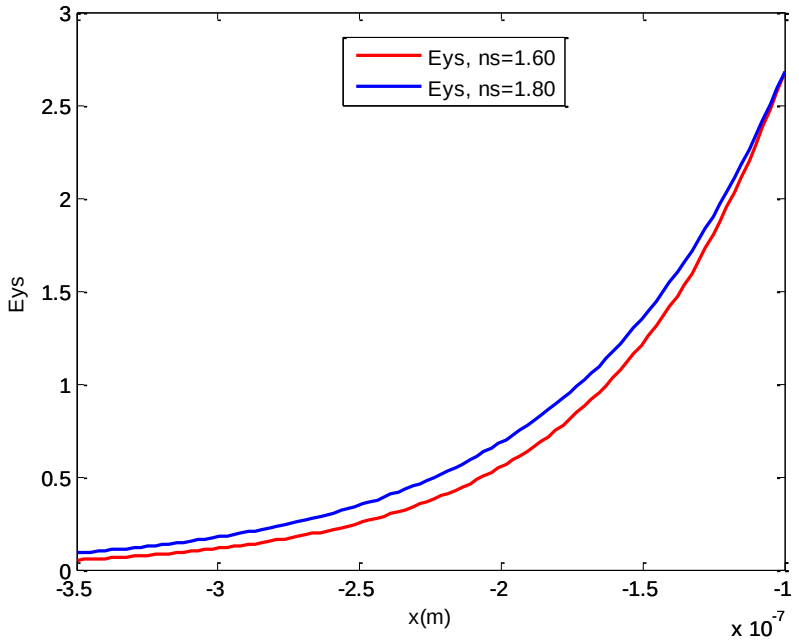

Figure IV.32: Evanescent field components E_{ys} in the substrate versus x of TE_0 mode for different substrate refractive indices, (n_c=1.48, d=100 nm, $LiNbO_3$ as guiding film).

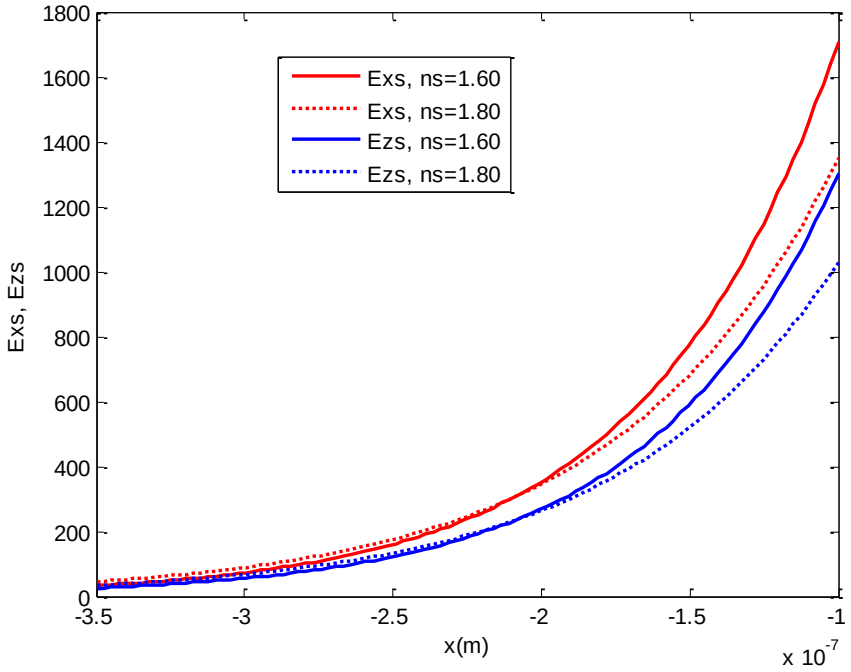

Figure IV.33: Evanescent field components (E_{xs}, E_{zs}) in the substrate versus x of TM_0 mode for different substrate refractive indices, (n_c=1.48, d=100 nm, $LiNbO_3$as guiding film).

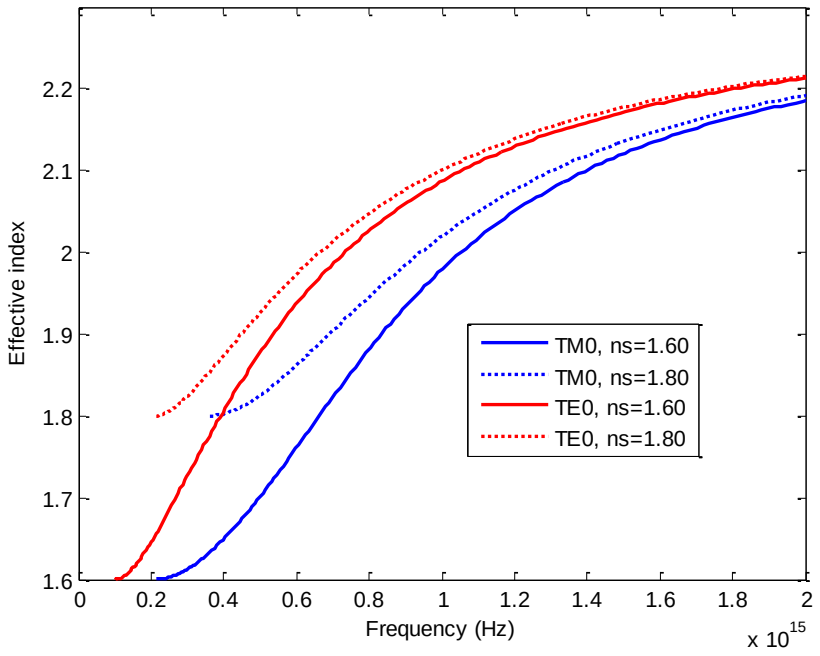

Figure IV.34: Effective index versus frequency of TE_0 and TM_0 modes in slab waveguide for different substrate indices, (n_c=1.48, d=100 nm, $LiNbO_3$as guiding film).

C. Influence of the core refractive index

Figures IV.35 and IV.36, represent sensitivities as a function of the frequency of TE, TM modes, respectively, for different core refractive index. While, Figure IV.37 and IV.38, illustrate the sensitivities of TE_0, TM_0 modes as a function of the effective refractive index, for different core refractive index. For TE_0, maximal sensitivities, corresponding to 1.80 and 2.2880 core refractive index, are 0.125; 0.24, respectively and their corresponding frequencies are 6.6E14 Hz; 2.E14 Hz; even though, their corresponding effective refractive indices are 1.62; 1.65 successively. However, for TM_0, maximal sensitivities, corresponding to, 1.80 and 2.2880 substrate refractive index are 0.15; 0.34, respectively; while their corresponding frequencies are 8.5E14 Hz; 5.0E14 Hz; and their corresponding effective refractive indices are 1.63 and 1.71 successively. The curves show that, the sensitivity of the slab waveguide sensor increases by increasing the core refractive index for both TE and TM modes. In addition to that, the position of the maximal sensitivities exhibit shifts toward lower frequencies, Figures IV.35, IV.36, and shifts toward higher values of effective refractive indices, figure.37, 38. Thus, as in the cases of cover and substrate refractive indices, changes of core refractive index, induces changes in the value of maximum sensitivity and changes in their corresponding frequency and effective refractive index.

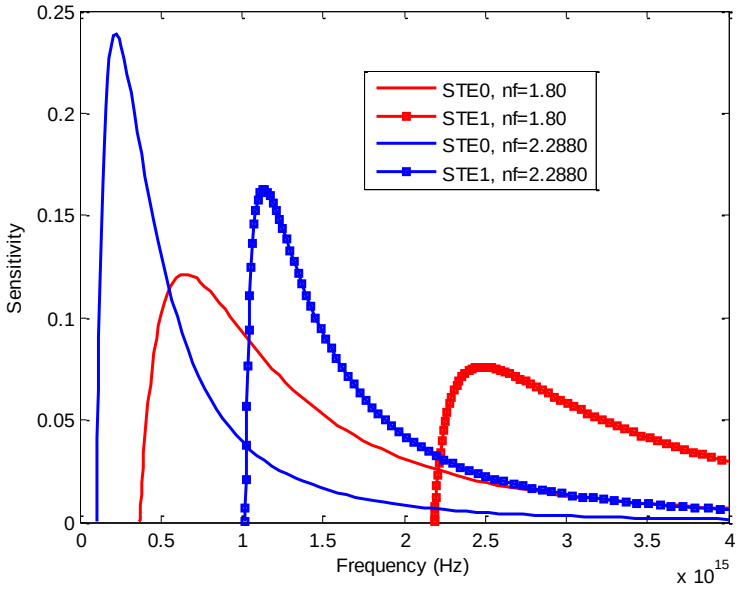

Figure IV.35: Sensitivity according to the frequency for TE modes for dissimilar refractive index of the core n_f, lines curves for TE_0 modes and square markers linked lines curves for TE_1 modes, (n_c=1.48, d=100 nm, ns=1.60).

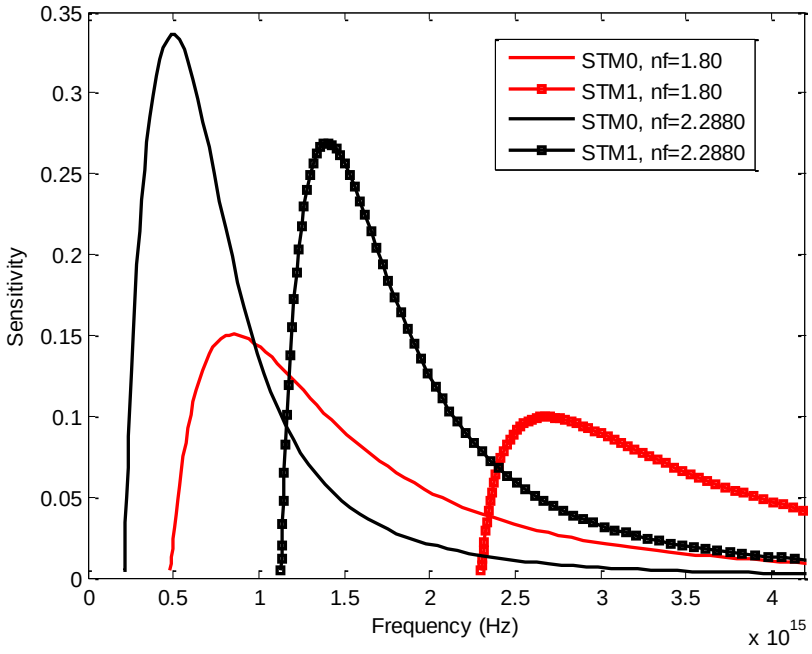

Figure IV.36: Sensitivity according to the frequency for TM modes for diverse refractive index of the core n_f, lines curves for TM_0 modes and square markers linked lines curves for TM_1 modes, (n_c=1.48, d=100 nm, ns=1.60).

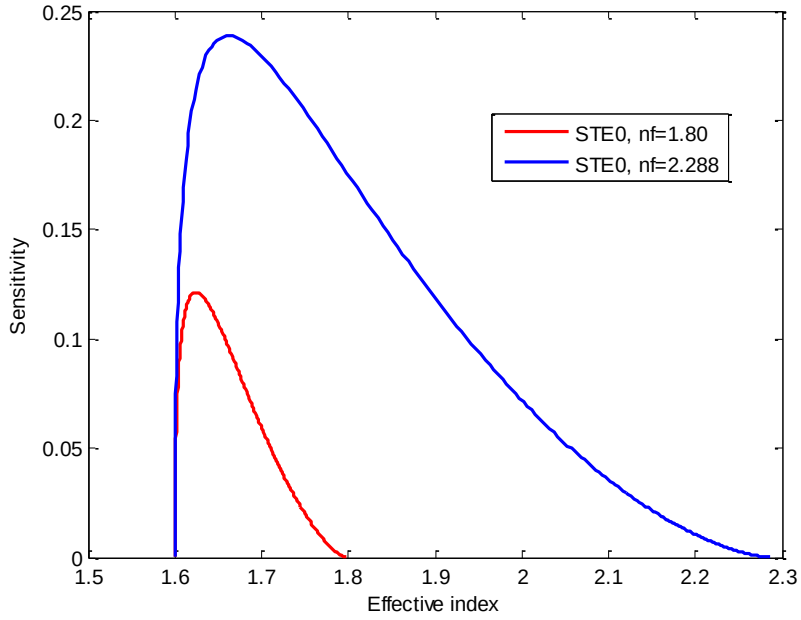

Figure IV.37: Sensitivity according to the effective index for TE_0 mode for dissimilar refractive index of the core n_f, (n_c=1.48, n_s=1.60, d=100 nm,).

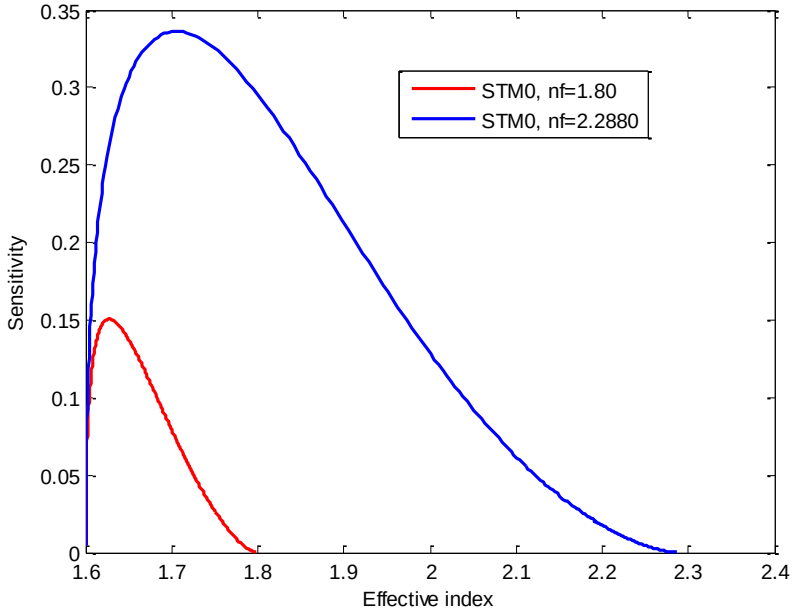

Figure IV.38: Sensitivity according to the effective index for TM_0 mode for dissimilar refractive index of the core n_f, (n_c=1.48, n_s=1.60, d=100 nm,).

Figure IV.39 and IV.40 represent evanescent field components in the cover of TE_0 and TM_0 modes, for different core refractive indices, respectively. The curves show middle changes in the evanescent field components caused by changes of core refractive index; in fact, these changes occur far from the cut off frequencies of each mode. Near to these latter, there are small changes of evanescent field components. These changes are produced by the variation of effective refractive indices of TE_0, TM_0 modes induced by changes of core refractive index, Figure IV.41. These variations of the evanescent field components, far from the cut off frequencies, have neglected influence on the sensitivity of the slab waveguide sensor, since the peaks of sensitivities are situated near the cut off frequencies.

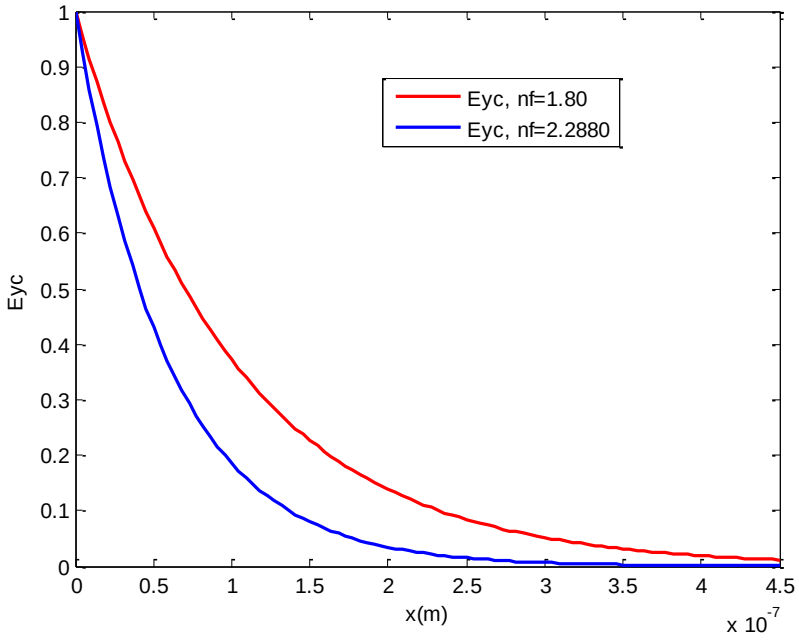

Figure IV.39: Evanescent field component E_{yc} in the cover versus x of TE_0 mode for different core refractive indices, (n_s=1.60, n_c=1.48, d=100 nm).

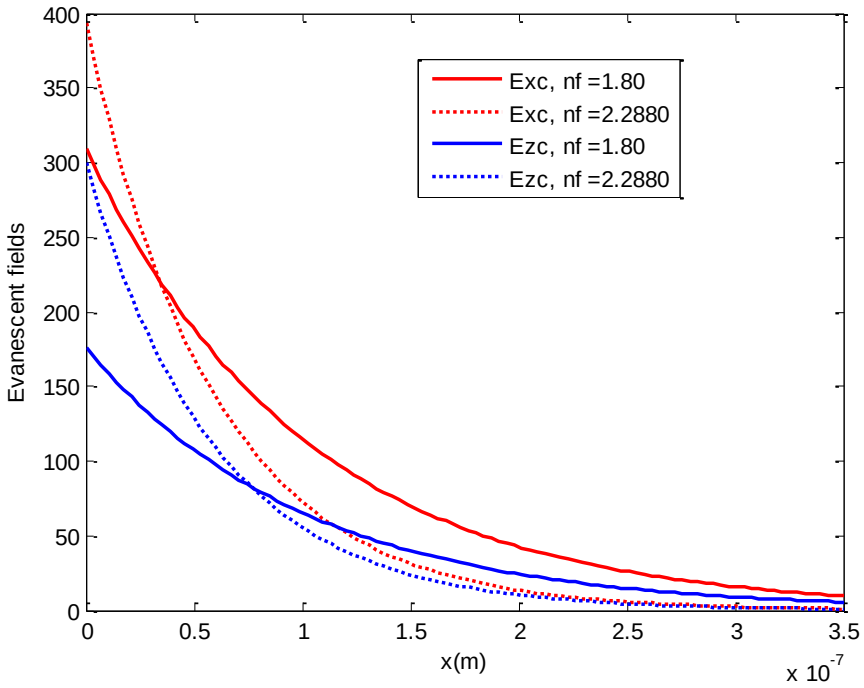

Figure IV.40: Evanescent field components (E_{xc}, E_{zc}) in the cover versus x of TM_0 mode for different core refractive indices, (n_s=1.60, n_c=1.48, d=100 nm).

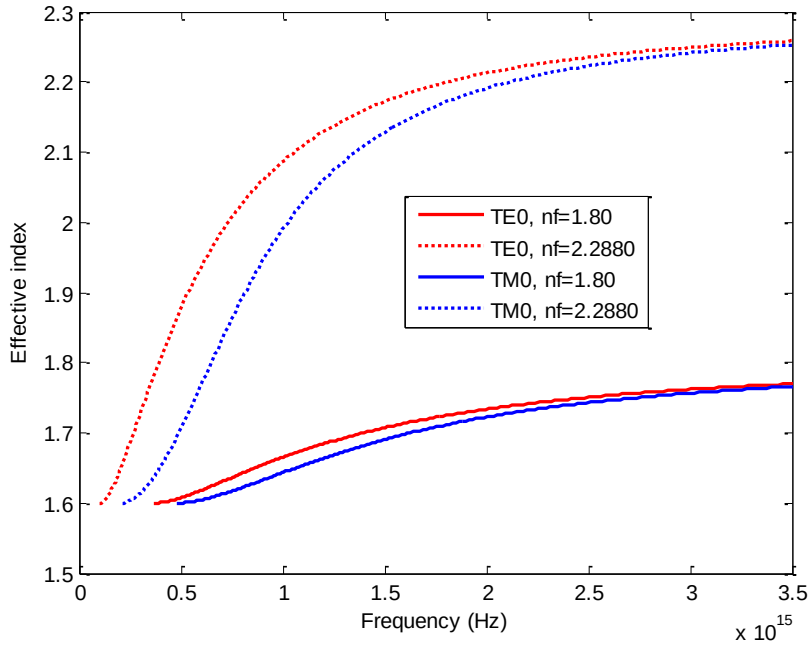

Figure IV.41: Effective index versus frequency of TE_0 and TM_0 modes in slab waveguide for different core indices, (n_c=1.48, n_s=1.60, d=100 nm).

IV.2.4. Influence of the electric field induced birefringence on the sensor sensitivity

When the electric field is applied along the optic axis of the $LiNbO_3$, its refractive indices will be changed but the crystal remainder uniaxial. The approximate model of the studied sensor is illustrated in Figure IV. 42.

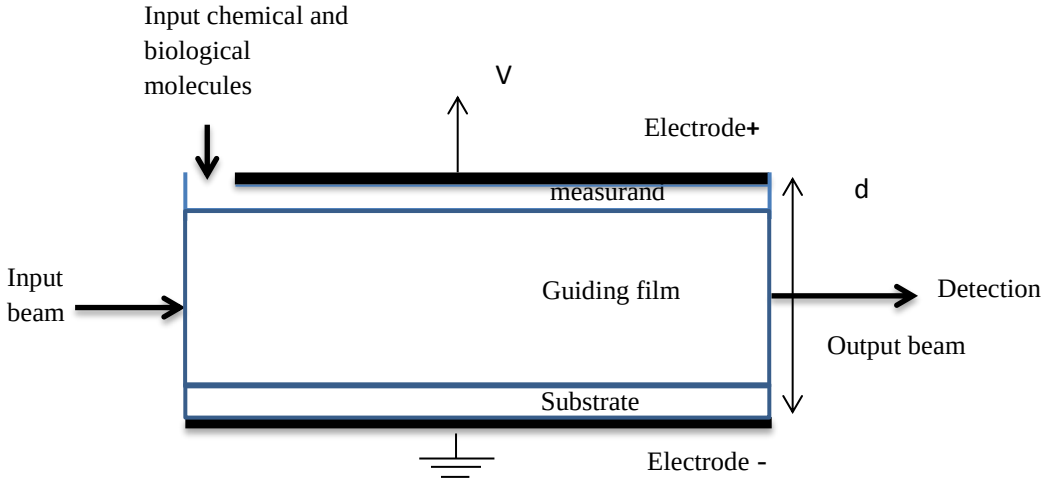

Figure IV.42: Approximate model of birefringent slab waveguide sensor

According to the direction of the applied field, we separate between two cases: If the electric field is applied along the optic axis, then, refractive indices are changed as [86]:

$$n_0(E) \approx n_0 - \tfrac{1}{2} n_0^3 r_{13} E \quad \text{(IV.15)}$$

$$n_e(E) \approx n_e - \tfrac{1}{2} n_e^3 r_{33} E \quad \text{(IV.16)}$$

Contrary, for negative applied electric field, the refractive indices are changed as:

$$n_0(E) \approx n_0 + \tfrac{1}{2} n_0^3 r_{13} E \quad \text{(IV.17)}$$

$$n_e(E) \approx n_e + \tfrac{1}{2} n_e^3 r_{33} E \quad \text{(IV.18)}$$

Where: n_0 and n_e are the ordinary and the extraordinary refractive indices of the $LiNbO_3$ without the E-field. However, $n_0(E)$and $n_e(E)$ are correspondingly the changed ordinary and extraordinary refractive indices of the $LiNbO_3$ after the application of the E field; $r_{13}$and $r_{33}$are the linear electro-optic coefficients of the medium.

The total birefringence of the uniaxial Crystal ($LiNbO_3$), as presented by [87] is given as:

$$\Delta n(E) = \left| n_{high}(E) - n_{low}(E) \right| \quad \text{(IV.19)}$$

The expressions (IV.20), (IV.21) give the total birefringence for positive and negative applied E-field, successively:

$$\Delta n(E) = \left| n_0 - n_e + \tfrac{1}{2} E (n_e^3 r_{33} - n_0^3 r_{13}) \right| \quad \text{(IV.20)}$$

$$\Delta n(E) = \left| n_0 - n_e + \tfrac{1}{2} E \left(n_0^3 r_{13} - \tfrac{1}{2} n_e^3 r_{33} \right) \right| \quad \text{(IV.21)}$$

Table IV**.1:** Electro-optic coefficients of $LiNbO_3$

n_0	n_e	$r_{13}(10^{-12}\ mV^{-1})$	$r_{33}(10^{-12}\ mV^{-1})$
2.2880	2.2030	10	32.2

According to the equations (IV.20) and (IV.21) we deduce that the total birefringence of the $LiNbO_3$ material is an increasing function of the electric field, if the latter is applied along the optic axis. In contrary, the total birefringence is a decreasing function of the electric field if the latter is applied opposite to the optic axis.

The curves of sensitivities for TE_0 or TM_0, indicate that, for positive E-field (Figure IV.43), the increase of the anisotropy induce the decrease of the sensitivity, mainly around the

maximum. Nevertheless, for negative E-field (Figure IV.44), the decrease of the anisotropy, incite the increase of the sensitivity around the maximum.

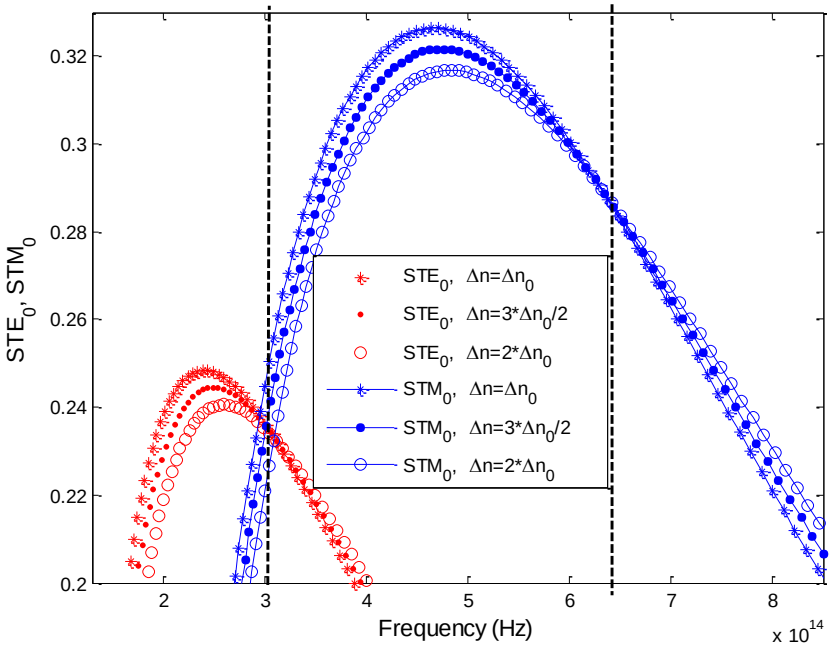

Figure IV.43: TM_0 and TE_0 modes sensitivities according to the frequency for diverse values of the anisotropy, in the case of positive E-field, blue curves for TM_0 mode and red curves for TE_0 mode.

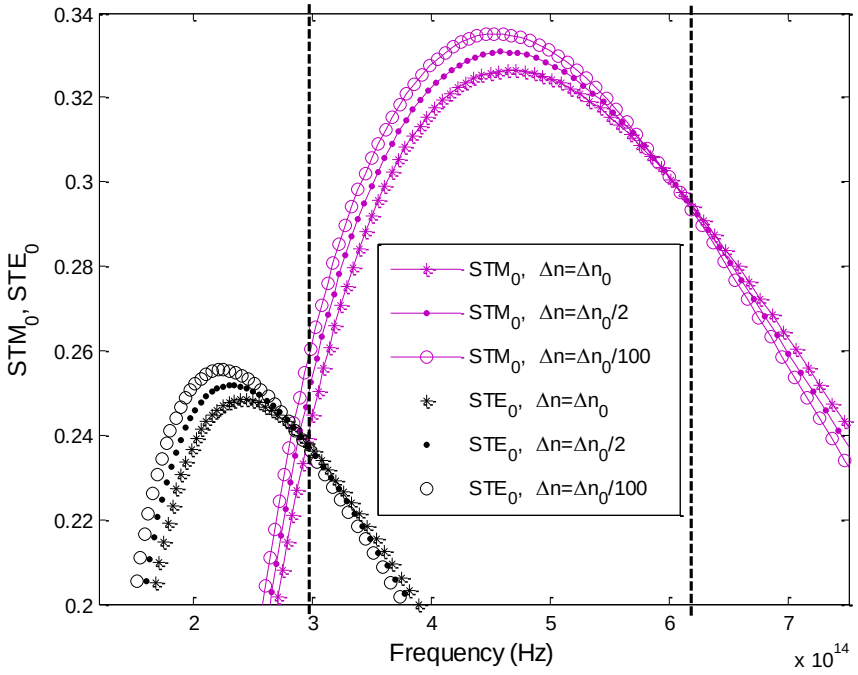

Figure IV.44: Sensitivity according to the frequency for diverse values of the anisotropy, in the case of negative E-field, magenta curves for TM_0 mode and black curves for TE_0 mode.

Figure IV.45 and IV.46 present maximum sensitivities changes of fundamental modes as a function of total birefringence Δn for positive and negative E-Field, respectively. The figures show that the sensitivity of the TM_0 mode is greater than that of TE_0 mode. Furthermore, the figures show that the sensitivities in the state of negative E-field are significantly greater than those in the situation of positive E-field.

It should be noted that all values of sensitivity found previously are comparable to those found in [88, 89, 90, 91 and 92].

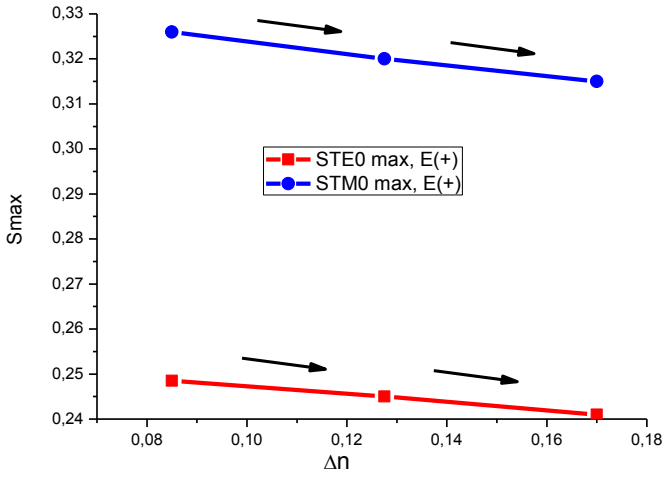

Figure IV.45: Maximum sensitivity changes according to the birefringence for positive electric field**,** red line for TE_0 mode and blue line for TM_0 mode.

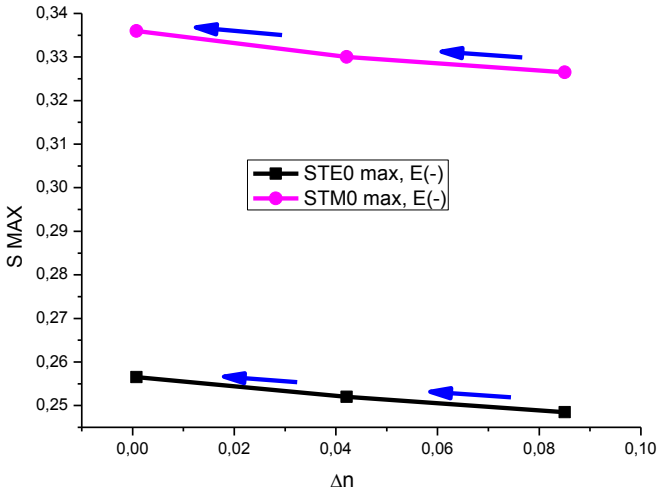

Figure IV.46: Maximum sensitivity changes according to the birefringence for negative electric field**,** black line for TE_0 mode and magenta line for TM_0 mode.

Figure IV.47 and IV.48 represent TE_0 and TM_0 effective refractive index changes according to the frequency for diverse values of increasing and decreasing birefringence, respectively. Figure.46 shows that, the increase of the birefringence induces a decrease in the effective refractive index of both TE_0 and TM_0 modes. While, Figure IV.48 shows that, the decreasing of the birefringence induces an increase in the effective refractive index of both TE_0 and TM_0 modes.

From the curves of effective refractive index (Figure IV.47, IV.48) and the curves of the sensitivities (Figure IV.43, IV.44), we can previously, conclude that the evanescent fields changes induced by the birefringence have no or neglected influence on the sensitivity changes induced by this birefringence. This conclusion is explained as follow: for the reason that, evanescent field components are functions of effective refractive index, in the other hand, for the frequencies where the sensitivity changes are maximal (vertical dashed line in Figures IV.47, IV.48), we show that the effective refractive index changes are minimal, hence, evanescent fields changes will be minimal. Thus, sensitivity changes are due to the birefringence itself.

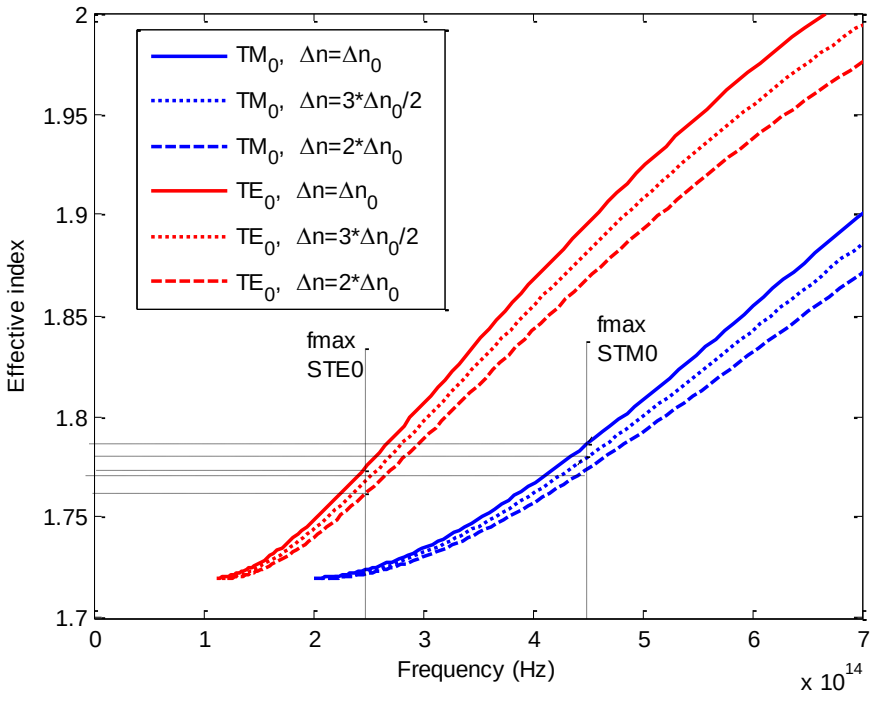

Figure IV.47: Effective refractive index according to the frequency for diverse values of increasing birefringence, blue curves for TM_0 mode and red curves for TE_0 mode.

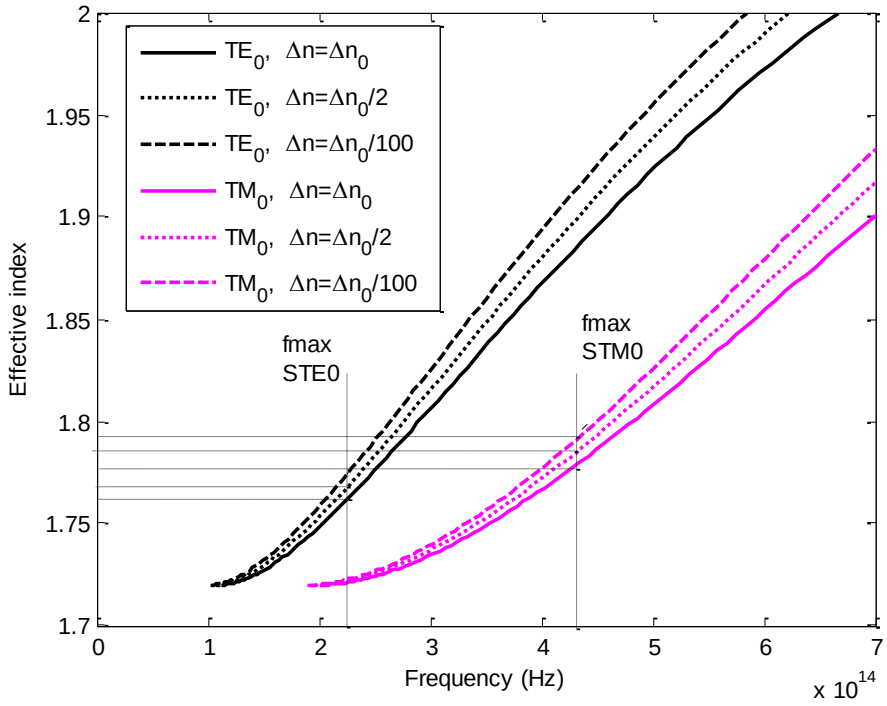

Figure IV.48: Effective refractive index according to the frequency for diverse values of decreasing birefringence, magenta curves for TM_0 mode and black curves for TE_0 mode.

IV.3. Conclusion

In this chapter, we have studied the sensitivity and the evanescent field of a slab waveguide sensor based on evanescent wave interactions constituted by $LiNbO_3$. Firstly, the sensitivity expressions are calculated using the TE and TM mode dispersion equations determined in the previous chapter. Secondly, we have investigated the influence of the source parameters, geometrical and physical parameters of the planar waveguide on the sensor sensitivity and the evanescent field, using the previous Matlab program. The results show, in all cases, that, the maximal sensitivities of TM modes and their corresponding frequencies are greater than those of TE modes. In addition to that, maximal sensitivities of both TE and TM modes are situated in different frequency bands, where those of TE modes are located in the near infra-red band and Those of TM in the visible rang. This result confirm our prediction that, birefringent waveguide based sensor can detects two different gas substances, for example, which have two different absorption lines.

Otherwise, the increase of the amplitude and the source's wavelength, induce the increase of both the maximal sensitivity and the evanescent field in the cover. Further, the increase of the core thickness induces the decrease of the sensitivity of the sensor, in the reason of the

decrease of the evanescent field. Furthermore, we have found that, the increase of the cover and the core indices induces the increase of the sensor sensitivity. On the contrary, the increase of the substrate refractive index induces the decrease of the sensor sensitivity. It is worth to note that, changes of physical parameters of the waveguide sensor have no or neglected influence on the evanescent fields in the cover.

In addition to that, we have studied the influence of E-field induced birefringence of the wave guiding film ($LiNbO_3$), on the sensitivity of the studied sensor for TE_0 and TM_0 modes. The study indicate that, for positive E-field, the increase of the anisotropy induce the decrease of the sensitivity, mainly around the maximum for both fundamental modes. Nevertheless, for negative E-field, the decrease of the anisotropy incites the increase of the sensitivity around the maximum. This property can be used to fabricate photonic sensor with adjustable sensitivity by just varying the applied electric field.

GENERAL CONCLUSION

The aim of this dissertation was divided into two parts. The first one, was the modeling of optical waveguides used for photonic sensors, in particularly, the slab waveguide and embedded-strip waveguide. The second part, was the modeling of birefringent planar waveguide sensor based on evanescent wave interactions constituted by $LiNbO_3$ as a guiding film. Such sensors can be used to detect two different substances in the same time by the same configuration, by reason of, in such birefringent waveguide we have two orthogonal modes that propagated simultaneously without interference (TE mode and TM mode). TE mode can detect one substance, and TM mode can sense the other substance.

In the first part, isotropic and uniaxial anisotropic slab waveguides were modeled with the optical ray method and the electromagnetic method, respectively. The former approach allowed us to calculate the dispersion equations of the TE and TM guided modes function of the propagation angles and the effective indices of the guided modes. Whereas, the electromagnetic approach, permitted us to calculate the wave equations, their solutions and the characteristic equations, as well as, the solutions of electromagnetic field in the three regions of the waveguide, where each region was fabricated by a uniaxial anisotropic crystal. We have developed a program in Matlab, based on the bisection method, which allowed us to calculate the propagation constants of both TE and TM polarizations, as a function of the frequency, of the wavelength and the thickness of the waveguiding film. The developed program also allowed us to see the influence of the physical and geometrical parameters as well as the source's wavelength on the guided modes. The results showed that, the increase in the thickness of the core makes increasing the propagation constants of the modes as well as reducing their cut-off frequencies, especially for of higher order modes. Further, the increase in the source's wavelength motivates the decrease of the propagation constants of modes and an increase of their cut-off thicknesses, especially for higher orders modes. Furthermore, changes of cover and substrate refractive indices have slight influence on the propagating modes. However, small changes in the core refractive index engender considerable changes in the propagation constants and cut-off frequencies of the guided modes. On the other hand, the effective index method (EIM) was explained in detail and used to calculate dispersion equations of E_{mn}^{y} and E_{mn}^{x} modes as well as their field distribution in each region of the Embedded-strip waveguide.

In the second part, we have investigated the sensitivity and the evanescent field of a slab waveguide sensor based on evanescent wave interactions constituted by $LiNbO_3$. Firstly, the sensitivity expressions are calculated using the TE and TM mode dispersion equations

determined in the first part. Secondly, we have investigated the influence of the source parameters, geometrical and physical parameters of the planar waveguide on the sensor sensitivity and the evanescent field, using the previous Matlab program. The results showed, in all cases, that, the maximal sensitivities of TM modes and their corresponding frequencies are greater than those of TE modes. In addition to that, maximal sensitivities of both TE and TM modes are situated in different frequency bands, where those of TE modes are located in the near infra-red band and Those of TM in the visible rang. This result confirm our prediction said that, birefringent waveguide based sensor can detects two different gas substances, for example, which have two different absorption lines. Otherwise, the increase of the amplitude and the source's wavelength, induce the increase of both the maximal sensitivity and the evanescent field in the cover. Further, the increase of the core thickness induces the decrease of the sensitivity of the sensor, in the reason of the decrease of the evanescent field. Furthermore, we have found that, the increase of the cover and the core indices induces the increase of the sensor sensitivity. On the contrary, the increase of the substrate refractive index induces the decrease of the sensor sensitivity. It is worth to note that, changes of physical parameters of the waveguide sensor have no or neglected influence on the evanescent fields in the cover.

In addition to that, we have studied the influence of E-field induced birefringence of the wave guiding film ($LiNbO_3$), on the sensitivity of the studied sensor for fundamental modes. The study indicate that, for positive E-field, the increase of the anisotropy induce the decrease of the sensitivity, mainly around the maximum for both fundamental modes. Nevertheless, for negative E-field, the decrease of the anisotropy incites the increase of the sensitivity around the maximum. This property can be used to fabricate photonic sensor with adjustable sensitivity by just varying the applied electric field.

As future perspectives, the obtained theoretical results of the birefringent slab waveguide based photonic sensor can be completed by an experimental step. Diversely, Modeling of 2D and 3D photonic waveguides based sensors by 3D numerical methods for homogenous and surface sensing with other optical materials is our future research domain.

REFERENCES

[1] K. T. V. Grattan and B. T. Meggitt: Optical Fiber Sensor Technology, Volume 4: Chemical and Environmental Sensing. © Springer Science Business. Media Dordrecht (1999).

[2] F. D. Leonardis & Passaro, V.M.N: Modeling and Performance of a Guided-Wave Optical Angular Velocity Sensor based on Raman Effect in SOI, *IEEE J. Lightwave Technol*., 25 (9), 2352-2366 (2007).

[3] V. M. N. Passaro, B. Troia, M. L. Notte and F. D. Leonardis: Chemical Sensors Based on Photonic Structures. Advances in Chemical Sensors, Edited by Prof. Wen Wang (2012).

[4] F. Baldini, A.N. Chester J, Homola and S. Martellucci: Optical-chemical-sensors. © Springer *(*2006).

[5] V. M. N. Passaro, C. de Tullio, B. Troia, M. La Notte, G. Giannoccaro and F. De Leonardis: Recent Advances in Integrated Photonic Sensors, *Sensors*, 12, 15558-15598 *(*2012).

[6] V. Dobrusin and S. Ruschin: Fabrication of integrated Ti: LiNbO3 waveguide polarizer, *Optical Engineering*, 47(12), (2008).

[7] M. Farhat O. Hameed and S. Obayya: Computational Photonic Sensors. © Springer International Publishing AG, part of Springer Nature (2019).

[8] S. Patrick, M. Hülsemann, B. Dietzel and A. Mai: Optical Biosensors Based on Silicon-On-Insulator Ring Resonators: *A Review. J. Molecules*, 24(3), 519 (2019).

[9] P. Bettotti, A. Pitanti, E. Rigo, F. D. Leonardis, V. M. N. Passaro and L. Pavesi: Modeling of Slot Waveguide Sensors Based on Polymeric Materials. *Sensors*, 11, 7327-7340 (2011).

[10] C. A. Barrios: Optical Slot-Waveguide Based Biochemical Sensors. *Sensors*, 9, 4751-4765 (2009).

[11] Luff, B.J.; Harris, R.D.; Wilkinson, J.S.; Wilson, R.; Schiffrin, D.J. Integrated-optical directional coupler biosensor. *Opt. Lett*, 21, 618–620 (1996).

[12] Heideman, R.G.; Kooyman, R.P.H.; Greve, J: Performance of a highly sensitive optical waveguide Mach-Zehnder interferometer immunosensor. *Sens. Actuat. B,* 10, 209–217 (1993).

[13] A. Ymeti, J. Greve, P.V. Lambeck, T.Wink, H. van, Beumer, R. R.Wijn, R. G. Heideman, V. Subramanian, and J. S. Kanger: Fast, ultrasensitive virus detection using a young interferometer sensor, *Nano Lett*. 7(2), 394–397 (2007).

[14] Armani, A.M.; Kulkarni, E.P.; Fraser, S.E.; Flagan, R.C.; Vahala, K.J. Label-free, single molecule detection with optical microcavities. *Science*, 317, 783–786 (2007).

[15] C. Ranacher, A. Tortschanoff, C. Consani, M. Moridi, T. Grille and B. Jakoby: Photonic Gas Sensor Using a Silicon Strip Waveguide, *J. Proceedings*, 1, 547 (2017).

[16] J. Milvich, D. Kohler, W. Freude and C. Koos: Surface sensing with integrated optical waveguides: A design guideline. *Optics express*, 26 (16), (2018).

[17] M. A. Butt, S. A. Degtyarev, S. N. Khonina & N. L. Kazanskiy: An evanescent field absorption gas sensor at mid- IR 3.39 μm wavelength. *Journal of Modern Optics*, 1892-1897 (2017).

[18] V. R. Almeida, Q. Xu, C. A. Barrios, and M. Lipson: Guiding and confining light in void nanostructure. *Optics letters*. 29 (11), (2004).

[19] Passaro V, La Notte M: Optimizing SOI slot waveguide fabrication tolerances and strip slot coupling for very efficient optical sensing. *Sensors* 12 (3), 2436-2455 (2012).

[20] Wang Z, Zhu N, Tang Y, Wosinski L, Dai D, He S. Ultra-compact low-loss coupler between strip and slot waveguides. *Optics Letters*, 34 (10), 1498-1500 (2009).

[21] Passaro, V.M.N.; Dell'Olio, F.; Ciminelli, C.; Armenise, M.N: Efficient chemical sensing by coupled slot SOI waveguides. *Sensors*, 9, 1012–1032 (2009).

[22] Q. Liu et al., "Highly sensitive Mach–Zehnder interferometer biosensor based on silicon nitride slot waveguide," *Sens. Actuators B Chem.*, 188, 681 –688 (2013).

[23] Barrios, C.A.; Gylfason, K.B.; Sánchez, B.; Griol, A.; Sohlström, H.; Holgado, M.; Casquel, R. Slot-waveguide biochemical sensor. *Opt. Lett*., 32, 3080-3082 (2007).

[24] P. H. FU, T. Y. CHiang, N. C. Cheng, Y. F Ma and D.W. Huang: Microring resonator composed of vertical slot waveguides with minimum polarization mode dispersion over a wide spectral range. *Applied Optics*, 55 (13), 2016.

[25] G. Yuan, L. Gao, Y. Chen, X. Liu, J. Wang, Z. Wang: Improvement of optical sensing performances of a double-slot-waveguide-based ring resonator sensor on silicon-on-insulator platform. *Optik* 125, 850– 854 (2014).

[26] S. Patrick: Chapter 10: Silicon-on-Insulator Slot Waveguides: Theory and Applications in Electro-Optics and Optical Sensing. From the Edited Volume: Emerging Waveguide Technology. Edited by Kok Yeow You. Licensee Intech Open (2018).

[27] Dell'Olio, F.; Passaro, V.M.N: Optical sensing by optimized silicon slot waveguides. *Opt. Express*, 15, 4977–4993 (2007).

[28] E. Jordana, J.M. Fedeli, P. Lyan, J.P. Colonna, P. Gautier, N. Daldosso, L. Pavesi, Y. Lebour,P. Pellegrino, B. Garrido, J. Blasco, Deep-UV lithography fabrication of slot waveguides and sandwiched waveguides for nonlinear applications. In 4th IEEE International Conference on Group IV Photonics, 1–3 (2007).

[29] J. G.W. Pérez, A. H. ElHouati, A. S. Postigo, J. Leuermann, D. X. Xu, P. Cheben, A. O. Moñux, R. Halir and I. M. Fernández: Subwavelength structures for silicon photonics biosensing. *Optics and Laser Technology* 109, 437–448 (2019).

[30] Giampaolo Pitruzzello and Thomas F. Krauss: Photonic crystal resonances for sensing and imaging. *Journal of Optics*. 20 (7), (2018).

[31] J. Joannopoulos, S. Johnson, J. Winn, and R. Meade: Photonic Crystals: Molding the Flow of Light. By Princeton University Press, (2008).

[32] Y. Liu1, H. W. M. Salemink: Photonic crystal-based all-optical on-chip sensor. *Optics Express* 20 (18), 19912-19920 (2012).

[33] C. Y. Chao, L. J. Guo: Design and optimization of microring resonators in biochemical sensing applications, *Journal of Lightwave Technology* 24, 1395–1402 (2006).

[34] B. Troia, A. Paolicelli, F. D. Leonardis and V. M. N. Passaro: Chapter11: Photonic Crystals for Optical Sensing: A Review. From, Advances in Photonic Crystals. Edited by Vittorio M. N. Passaro, (2013).

[35] Krauss, T.F: Slow light in photonic crystal waveguides. *J. Phys. D*, *40*, 2666–2670 (2007).

[36] Krauss, T.F: Why do we need slow light? *Nat. Phot.*, *2*, 448–450 (2008).

[37] Mark G. Scullion, Thomas F. Krauss and Andrea Di Falco: Slotted Photonic Crystal Sensors. *Sensors*, *13*, 3675-3710 (2013).

[38] A. Di Falco, L. O'Faolain, and T. F. Krauss: Dispersion control and slow light in slotted photonic crystal waveguides, *Appl. Phys. Lett.*, 92, 83501 (2008).

[39] J. Wu, C. Peng, Y. P.Li, and Z.Y. Wang: Light Localization in Slot Photonic Crystal Waveguide, *Chin. Phys. Lett.*, 26 (1), 14209 (2009).

[40] U. P. Dharanipathy, M. Minkov, M. Tonin, V. Savona, and R. Houdré: High-Q silicon photonic crystal cavity for enhanced optical nonlinearities, *Appl. Phys. Lett.*, 105, 101101 (2014).

[41] H. Takagi, Y. Ota, N. Kumagai, S. Ishida, S. Iwamoto, and Y. Arakawa: High Q H1 photonic crystal nanocavities with efficient vertical emission. *Opt. Express*, 20 (27), 28292–28300 (2012).

[42] Jágerská, J.; Zhang, H.; Diao, Z.; Le Thomas, N. & Houdré, R. (2010): Refractive index sensing with an air-slot photonic crystal nanocavity. *Optics Letters*, 35(15), 2523-2525 (2010).

[43] José Luís Santos Faramarz Farahi: Handbook of Optical Sensors. CRC Press. (2015).

[44] M Gabalis, D Urbonas and R Petruskevicius: A perforated microring resonator for optical sensing applications. *J. Opt*. 16, 105003, (2014).

[45] V. M. N. Passaro, F. Dell'Olio, B. Casamassima and F. De Leonardis: Guided-Wave Optical Biosensors. *Sensors*, 7, 508-536 (2007).

[46] Andreas Hänsel and Martijn: Opportunities for photonic integrated circuits in optical gas sensors. *J. Phys. Photonics* 2, 012002 (2020).

[47] Vo-Dinh, T.; Cullum, B. M. "Fluorescence Spectroscopy for Biomedical Diagnostics, in chapter 5". Biomedical Photonics Handbook. Editor: Tuan Vo-Dinh. CRC Press (2003).

[48] L. Liu, X. Zhou, J. S. Wilkinson, P. Hua, B. Song & H. Shi: Integrated optical waveguide based fluorescent immunosensor for fast and sensitive detection of microcystin-LR in lakes: Optimization and Analysis. *Scientific Reports* 7, 3655, (2017).

[49] S. Kumar, P. Kumar, A. Das and C. S .Pathak: Chapter, Surface-Enhanced Raman Scattering: Introduction and Applications. Recent Advances in Nanophotonics-Fundamentals and Applications. intechopen. 92614, (2019).

[50] Weber WH, Merlin R.: Raman Scattering in Materials Science. Berlin, Heidelberg: *Springer*, (2000).

[51] Smith E, Dent G: Introduction, basic theory and principles. In: Smith E, Dent G, Editors. Modern Raman Spectrosopy - A Practical Approach. 5, (2005).

[52] Moskovits M: Surface-enhanced spectroscopy. *Reviews of Modern Physics*. 57, 783-826 (1985).

[53] De Leonardis, F.; Passaro, V.M.N.: Modeling of Raman amplification in Silicon-on-Insulator optical microcavities. *New J. Phys*, 9, 1–24 (2007).

[54] Liu, A.; Rong, H.; Jones, R.; Cohen, O.; Hak, D.; Paniccia, M: Optical amplification and lasing by stimulated Raman scattering in silicon waveguides. *J. Lightwave Technol*. 24, 1440–1455 (2006).

[55] M. Makela, P. Gordon, D. Tu, C. Soliman, G. L. Cote, K. Maitland, and P. T. Li: Benzene Derivatives Analysis Using Aluminum Nitride Waveguide Raman Sensors. *American Chemical Society*, (2020).

[56] E. Luan, H. Shoman, D. M. Ratner, K. C. Cheung and L. Chrostowski: Silicon Photonic Biosensors Using Label-Free Detection. *Sensors*, 18, 3519 (2018).

[57] Cesar S. Huertas, Olalla Calvo-Lozano, Arnan Mitchell and Laura M. Lechuga: Advanced Evanescent-Wave Optical Biosensors for the Detection of Nucleic Acids: An Analytic Perspective, *Frontiers in Chemistry*, 7, 724 (2019).

[58] K. E. Zinoviev, A. B. Gonzalez-Guerrero, C. Dominguez, and L. M. Lechuga: Integrated bimodal waveguide interferometric biosensor for label-free analysis. *J. Lightwave. Technol*. 29(13), 1926–1930 (2011).

[59]Daphne Duval and Laura M. Lechuga, chapter8: Optical Waveguide Biosensors, from, PHOTONICS Scientific Foundations, Technology and Applications, Biomedical Photonics, Spectroscopy, and Microscopy, Volume IV, Edited by DAVID L. ANDREWS; by John Wiley & Sons, Inc. Copyright © (2015).

[60] K. Schmitt, B. Schirmer, C. Hoffmann, A. Brandenburg, and P. Meyrueis: Interferometric biosensor based on planar optical waveguide sensor chips for label-free detection of surface bound bioreactions, *Biosens. Bioelectron*. 22(11), 2591–2597 (2007).

[61] J. H. Sim, Y. H. Kwak, C. H. Choi, S.-H. Paek, S. S. Park, and S. Seo: A birefringent waveguide biosensor platform for label-free live cell detection of Listeria monocytogenes, *Sens. Actuators B. Chem*. 173, 752–759 (2012).

[62] Zourob M., Lakhtakia A: Optical Guided-wave Chemical and Biosensors I., Vol. 7, 2010. Springer Series on Chemical Sensors and Biosensors. Methods and Applications. Series Editor: G. Urban (2010).

[63] S. V. Pham, M. Dijkstra, A. J. F. Hollink, L. J. Kauppinen, R. M. de Ridder, M. Pollnau, P. V. Lambeck, and H. J.W. M. Hoekstra: On-chip bulk-index concentration and direct, label-free protein sensing utilizing an optical grated-waveguide cavity, *Sens. Actuators B. Chem.* 174, 602–608 (2012).

[64] Sonia Grego, Jonathan R. McDaniel, Brian R. Stoner: Wavelength interrogation of grating-based optical biosensors in the input coupler configuration. *Sensors and Actuators B* 131, 347–355 (2008).

[65] J. Adrian, S. Pasche, J.-M. Diserens, F. Sanchez-Baeza, H. Gao, M. P. Marco, and G. Voirin: Waveguide interrogated optical immunosensor (WIOS) for detection of sulfonamide antibiotics in milk, *Biosens. Bioelectron*.24 (11), 3340–3346 (2009).

[66] Yiming. M, Bowei. D, Chengkuo. L: Progress of infrared guided-wave nanophotonic sensors and devices, *Journal of Nano Convergence*, 7, 12 (2020).

[67] G. Ycas et al., "High-coherence mid-infrared dual-comb spectroscopy spanning 2.6 to 5.2 μm," *Nat. Photonics* 12, 202–208 (2018).

[68] Z. M., Lakhtakia. A: Optical Guided-wave Chemical and Biosensors II., Vol. 8, 2010. Springer Series on Chemical Sensors and Biosensors. Methods and Applications. Series Editor: G. Urban.

[69] S. Patrick, C. Villringer, S. Pulwer, F. Heinrich, J. Bauer, B. Dietzel, C. Mai, A. Mai, M. Casalboni, and S. Schrader: Hybrid Waveguide Ring Resonator for Biochemical Sensing. *IEEE Sensors Journal* ; 17(15), 4781- 4790 (2017).

[70] M.-C. Estevez, M. Alvarez and L. M. Lechuga: Integrated optical devices for lab-on-a-chip biosensing applications. *Laser Photonics Rev.*, 1–25 (2011).

[71] J. T. Robinson, L. Chen, and M. Lipson: On-chip gas detection in silicon optical microcavities. *Optics Express*. 16(6), 4296-4301 (2008).

[72] G. Lifante: Integrated Photonics: Fundamentals. John Wiley & Sons Ltd, England (2003).

[73] B. e. a. Saleh, m. c. Teich: Fundamentals of photonics, wiley series in pure and applied optics. Editor: B. e. a. Saleh, published by john wiley & sons, Inc., Hoboken, new jersey (2007).

[74] S. K. Selvaraja and P. Sethi: Chapter 6: Review on Optical Waveguides. From: Emerging Waveguide Technology. Intech Open (2018).

[75] Robert G. Hunsperger: Integrated Optics Theory and Technology, Springer Science Business Media, NY 10013, USA March 2009.

[76] Refractive index database: https://refractiveindex.info.

[77] K. S. Chiang: Dual effective-index method for the analysis of rectangular dielectric waveguides. *Applied optics*. 25(13), (1986).

[78] J. Linares, V. Moreno and M.C. Nistal: Designing of Monomode Step-Index Channel Guides with Quasi-Exact Modal Solutions by the Effective Index Method, *Journal of Modern Optics*, 47, 599–604 (2000).

[79] K. OKAMOTO: Fundamentals of Optical Waveguides. Elsevier Academic Press publications. USA (2006).

[80] Ermini M. L., Mariani S., Scarano S., Minunni M: Bioanalytical approaches for the detection of single nucleotide polymorphisms by Surface Plasmon Resonance biosensors. *Biosens. Bioelectron*. 61, 28–37(2014).

[81] Levy, M., Osgood, R. M., Jr., Liu, R., Cross, L. E., Cargill III, G. S., Kumar, A., and Bakhru, H: Fabrication of single-crystal lithium niobate films by crystal ion slicing. *Appl. Phys. Lett*. 73(16), 2293-2295 (1998).

[82] Rabieia, P. and Gunter, P.: Optical and electro-optical properties of submicrometer lithium niobate slab waveguides prepared by crystal ion slicing and wafer bonding. *Appl. Phys. Lett.* 85 (20), 4603-4605 (2004).

[83] Parriaux, O., Dierauer, P: Normalized expressions for the optical sensitivity of evanescent wave sensors. *Opt. Lett*. 19(20), 1665–1665 (1994).

[84] Jalaleddine, A. M.: Guided waves propagating in isotropic and uniaxial anisotropic slab waveguide. Dissertation, Ohio University U.S.A (1982).

[85] Veldhuis, G. J., Parriaux, O., Hoekstra, H. J. W. M., and Lambeck, P. V.: Sensitivity enhancement in evanescent optical waveguide sensors. *J. Lightwave. Technol*. 18(5), 677–682 (2000).

[86] Saleh E. A., Teich, M. C.: Electro-optics. In: Saleh E. A., Teich, M. C. (Eds.): Fundamentals of Photonics. John Wiley & Sons, Inc., U.S.A (1991).

[87] Timtere, P., Usman, A., Ododo, J. C.: The phenomenon of nonlinear optical birefringence in uniaxial crystals. *Lat. Am. J. Phys. Educ.* 5(2), 432-437 (2011).

[88] H. M. Khalil, M. M. Shabat, S. A. TAYA and M. M. Abadla: Nonlinear optical waveguide structure for sensor application: tm case, *Int. J. Mod. Phys. B,* 21(30), 5075-5089 (2007).

[89] P. Karasinski: Optical uniform/gradient waveguide sensor structure – characterization, *Opto-electron. Rev*, 19(1), 01–09 (2011).
[90] P. Karasinski: Planar Optical Waveguide Sensor Structures with Grating Couplers, *Acta Phys. Pol. A*, Vol. 116 (2009).

[91] D. Kumar, V. Singh: Theoretical modeling of a nonlinear asymmetric metal-clad planar waveguide based sensors, *Optik*, 122, 1872– 1875 (2011).

[92] S.A. Tayaa, M. M. Shabata, H.M. Khalil: Enhancement of sensitivity in optical waveguide sensors using left-handed materials, *Optik*, 120, 504–508 (2009).

Doctoral thesis: Conception and modeling of photonic components. Application: photonic waveguide sensors.

By: Abdelbaki CHEROUANA **Supervisor: Prof. BOUCHAMA Idris**

الخلاصة -العمل الرئيسي لهذه الأطروحة هو نمذجة المستشعر الفوتوني المستند إلى الدليل الموجي المستوي مزدوج الانكسار، الذي يتكون من مادة $LiNbO_3$ كقلب للدليل الموجي. وذلك بدراسة تأثير عوامل المصدر الضوئي، والعوامل الهندسية والفيزيائية للدليل الموجي، وكذلك دراسة تأثير الانكسار المزدوج الناتج عن المجال الكهربائي، على حساسية المستشعر والمجال الزائل. أظهرت دراستنا أن استخدام مادة ثنائية الانكسار، مثل $LiNbO_3$، باعتبارها قلب الدليل الموجي للمستشعر الضوئي، يمكن أن يسمح لنا باكتشاف مادتين مختلفتين في نفس الوقت بنفس الإعدادات، بسبب وجود في الدليل الموجي مزدوج الانكسار، نوعين من الأنماط المتعامدة التي تنتشر في وقت واحد دون تداخل (نمط TE ونمط TM). بالإضافة إلى ذلك، توجد الحساسيات القصوى للأوضاع TE وTM في نطاقات تردد مختلفة، حيث توجد تلك الخاصة بأوضاع TE في النطاق القريب من الأشعة تحت الحمراء وتلك الخاصة بأوضاع TM في النطاق المرئي. علاوة على ذلك، فإن استخدام الانكسار الناجم عن المجال الكهربائي يمكن أن يجعل حساسية المستشعر الضوئي قابلة للتعديل عن طريق تغيير المجال الكهربائي المطبق فقط.

الكلمات المفتاحية: الأدلة الموجية الضوئية، الموجة الزائلة، الانكسار المستحث بالمجال الكهربائي، المستشعر القائم على الدليل الموجي المستوي، حساسية المستشعر الضوئي، التباين أحادي المحور.

Abstract - The main work of this thesis is the modeling of birefringent planar waveguide based photonic sensor fabricated by $LiNbO_3$ as waveguiding film, and studying the influence of source parameters, geometrical and physical parameters, as well as electric field induced birefringence on the sensitivity and evanescent field of the sensor. Our study showed that, the use of a birefringent material, like $LiNbO_3$, as a core of the waveguide can permit us the detection of two different substances in the same time by the same configuration, by reason of, in such birefringent waveguide we have two orthogonal modes that propagated simultaneously without interference (TE mode and TM mode). In addition to that, maximal sensitivities of both TE and TM modes are situated in different frequency bands, where those of TE modes are located in the near infra-red band and Those of TM in the visible rang. Furthermore, the use of electric field induced birefringence can make sensitivity of the photonic sensor adjustable by just varying the applied electric field.

Keywords: Photonic waveguides**,** Evanescent wave, electric filed induced birefringence, Slab waveguide based sensor, Optical sensor sensitivity, Uniaxial anisotropy.

Résumé - Le travail principal de cette thèse est la modélisation d'un capteur photonique basé sur un guide d'ondes planaire biréfringent fabriqué par $LiNbO_3$ en tant que cœur du guide d'onde, en étudiant l'influence des paramètres de la source, des paramètres géométriques et physiques du guide d'onde, ainsi que de la biréfringence induite par le champ électrique sur la sensibilité et champ évanescent du capteur. Notre étude a montré que l'utilisation d'un matériau biréfringent ($LiNbO_3$), comme cœur du guide d'ondes, peut nous permettre la détection de deux substances différentes en même temps par la même configuration, en raison que, dans un tel guide d'ondes biréfringent, nous avons deux modes orthogonaux qui se propagent simultanément sans interférence (mode TE et mode TM). De plus, les sensibilités maximales des modes TE et TM se situent dans des bandes de fréquences différentes, celles des modes TE se situant dans le proche infrarouge et celles du TM dans le visible. De plus, l'utilisation de la biréfringence induite par un champ électrique peut rendre la sensibilité du capteur photonique réglable en faisant simplement varier le champ électrique appliqué.

Mots-clés : Guides d'ondes photoniques, Onde évanescente, Biréfringence induite par champ électrique, Capteur à base d'un guide d'ondes planaire, Sensibilité du capteur optique, Anisotropie uniaxiale.